Comparison of Fission Product Release Predictions using PARFUME and BISON with Results from the AGR-3/4 Irradiation Experiment

September 2022

William F. Skerjanc and Wen Jiang

INL Idaho National Laboratory

Comparison of Fission Product Release Predictions using PARFUME and BISON with Results from the AGR-3/4 Irradiation Experiment

William F. Skerjanc and Wen Jiang

September 2022

**Idaho National Laboratory
Advanced Reactor Technologies
Idaho Falls, Idaho 83415**

http://www.art.inl.gov

Page intentionally left blank

INL ART Program

Comparison of Fission Product Release Predictions using PARFUME and BISON with Results from the

INL/RPT-22-69003

September 2022

Technical Reviewer:

_____   9/14/2022
Adriaan Riet   Date

Approved by:

_____   9/13/2022
Paul A. Demkowicz   Date
AGR Fuels Technical Director

_____   9/14/2022
Gerhard Strydom   Date
ART GCR National Technical Director

_____   9/13/2022
Michelle T. Sharp   Date
INL Quality Assurance

ABSTRACT

The PARFUME (PARticle FUel ModEl) fuel performance modeling code and the BISON nuclear fuel performance application built on the Multiphysics Object-Oriented Simulation Environment finite element library were used to predict the fission product release from tristructural isotropic (TRISO)-coated fuel particles and compacts during the third and fourth irradiation experiment of the Advanced Gas Reactor (AGR-3/4) Fuel Development and Qualification Program.

The fuel performance modeling codes PARFUME and BISON modeled the AGR-3/4 irradiation experiment using the fuel compact time-averaged volume averaged daily temperatures for a total irradiation duration of 369.1 effective full power days to predict the release fraction of the fission product silver (Ag-110m) from a representative TRISO-coated fuel particle from AGR-3/4 compacts. Post-irradiation examination measurements provided data on the release of these fission products in the compacts outside of the silicon carbide (SiC) layer. The PARFUME and BISON results were then compared to the silver release measured from compact gamma scanning. The results showed good agreement between PARFUME and BISON but both codes under-predicted the silver release fraction for all the compacts.

In addition, BISON was used to model and predict the fission product concentration radial profile outside of the compacts in capsules' inner and outer rings. These rings were either comprised of matrix or structural graphite. To obtain the concentration profiles of silver, cesium, and strontium, a sorption isotherm model was developed in BISON to capture the effects of fission product transport across the gaps between the concentric rings. The general shape of the concentration radial profiles as calculated by BISON were similar in the inner ring but varied in the outer ring depending on the fission product of interest or capsule temperature. Using this methodology and model, BISON can now aid in developing new fission product diffusion coefficients for matrix or structural graphite materials.

Page intentionally left blank

CONTENTS

FIGURES

TABLES

ACRONYMS

AGR	Advanced Gas Reactor
ATR	Advanced Test Reactor
BAF	Bacon Anisotropy Factor
CEGA	Combustion Engineering/General Atomics
DTF	designed-to-fail
EFPD	effective full power days
FB	fuel body
FIMA	fissions per initial heavy metal atom
FP	fission product
HTGR	high-temperature gas-cooled reactor
IAEA	International Atomic Energy Agency
INL	Idaho National Laboratory
IPyC	inner pyrolytic carbon
IR	inner radius or ring
LEU	low-enriched uranium
MOOSE	Multiphysics Object-Oriented Simulation Environment
NEFT	northeast flux trap
OPyC	outer pyrolytic carbon
OR	outer radius or ring
PALM	power axial locator mechanism
PARFUME	PARticle FUel ModEl
PIE	post-irradiation examination
PyC	pyrolytic carbon
SiC	silicon carbide
TAVA	time-average/volume-average
TMAP4	Tritium Migration Analysis Program Version 4
TRISO	tristructural isotropic
UCO	uranium oxycarbide

Page intentionally left blank

Comparison of Fission Product Release Predictions using PARFUME and BISON with Results from the AGR-3/4 Irradiation Experiment

1. INTRODUCTION

Several fuel and material irradiation experiments have been planned for Idaho National Laboratory's (INL's) Advanced Reactor Technologies (ART) Advanced Gas Reactor (AGR) Fuel Development and Qualification Program. These experiments support the development and qualification of tristructural isotropic (TRISO)-coated particle fuel for use in high-temperature gas-cooled reactors (HTGRs). The goals of these experiments are to provide irradiation performance data to support fuel process development, qualify fuel for normal operating conditions, support the development and validation of fuel performance and fission product transport models and codes, and provide irradiated fuel and materials for post-irradiation examination (PIE) and safety testing [1]. AGR-3/4 combined the third and fourth in this series of planned experiments to test TRISO-coated, low-enriched uranium oxycarbide (UCO) fuel.

This report documents comparisons between PIE measurements and the fission product release predicted by the fuel performance modeling code PARticle FUel ModEl (PARFUME) [2] and the finite element-based code BISON [3] for silver (Ag), cesium (Cs), and strontium (Sr) from TRISO-coated fuel particles and compacts from the AGR-3/4 irradiation experiment in the Advanced Test Reactor (ATR) at INL. The calculations include modeling AGR-3/4 compacts irradiated from December 2011 to April 2014 in the ATR over a total of 10 ATR cycles, including seven normal cycles, one low-power cycle, one unplanned outage cycle, and one power axial locator mechanism (PALM) cycle for a total of 369.1 effective full power days (EFPD). Because no burnup was accumulated during the low-power cycle and the AGR-3/4 test train was moved to the ATR canal during the unplanned outage and PALM cycles, the modeling only covers the seven normal power cycles. Previous comparisons were performed using PARFUME and PIE data from AGR-1 [4] and AGR-2 [5] irradiation experiments.

Details associated with completing these calculations along with the PIE measurement data are provided in the remainder of this document. The AGR-3/4 irradiation experiment is described briefly in Section 2, PARFUME and BISON modeling input parameters are described in Section 3, compact modeling results are compared to gamma scanning PIE data for silver in Section 4, the fission product radial concentration across capsule rings are presented in Section 5, conclusions are summarized in Section 6, and the references are listed in Section 7.

1.1 AGR Program

The Department of Energy AGR Fuel Development and Qualification program was established to qualify TRISO-coated fuel for use in HTGRs. The primary goal of the program is to provide a baseline fuel qualification data set in support of the licensing and operation of an HTGR [1].

Seven fuel and material irradiation experiments were planned for the Department of Energy AGR program. The overall objectives of these experiments are to [1]:

- Develop fuel fabrication capabilities

- Perform fuels and materials irradiation

- Perform safety testing and PIE

- Improve fuel performance modeling

- Evaluate fission product transport and source term determination.

1

1.2   PARFUME

PARFUME is an integrated mechanistic computer code that evaluates the thermal, mechanical, and physicochemical behavior of coated fuel particles and the probability for fuel failure given the particle-to-particle statistical variations in physical dimensions and material properties that arise during the fuel fabrication process [2]. PARFUME describes both the mechanical and physicochemical behavior of the fuel particle under irradiation and postulated accident conditions, while capturing the statistical nature of the fuel, and determines the failure probability of a population of fuel particles, accounting for all viable mechanisms that can lead to particle failure. In addition, PARFUME calculates fission product (FP) transport and determines the diffusion of FPs through the particle coating layers and their subsequent release through the fuel matrix to the coolant boundary. The general solution procedure used by PARFUME consists of the basic processes depicted in the flow chart of Figure 1.

Coated particle fuel exhibits statistical variations in physical dimensions and material properties from particle to particle due to the nature of the fabrication process. Particle behavior is also inherently multidimensional, further complicating model development. The failure probability of a batch of fuel particles depends on statistical variations in the fuel design parameters as well as variation in the characteristic strengths of the coating layers in a batch. The calculation of fuel particle failures implemented in PARFUME samples the fuel design parameters from a Gaussian statistical distribution, and the layer strengths are sampled from a Weibull statistical distribution [6] [7]. PARFUME allows for statistical variations in the kernel diameter, the four-layer thicknesses, the pyrocarbon densities, the degree of anisotropy of the pyrocarbon layers (as measured by the Bacon anisotropy factor [BAF]), the creep coefficient for the pyrocarbon, Poisson's ratio in creep for the pyrocarbon, bond strength between the inner pyrolytic carbon (IPyC) and silicon carbide (SiC) layers, and particle asphericity (as measured by the aspect ratio).
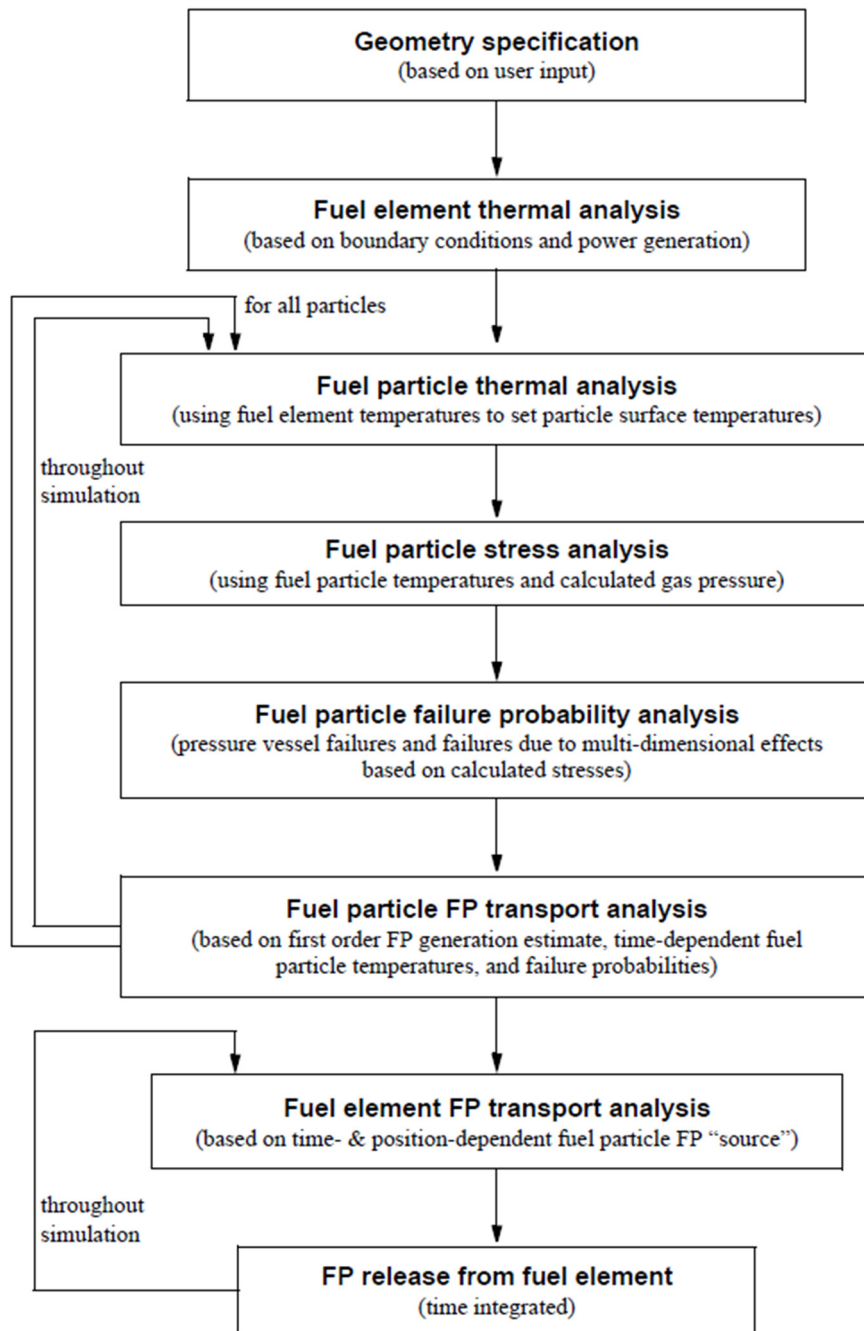
Figure 1. PARFUME calculation flow chart.

1.3 BISON

BISON [3] is a nuclear fuel performance application built using the Multiphysics Object-Oriented Simulation Environment (MOOSE) finite element library [8] developed at INL that is capable of modeling multiple fuel forms in a wide variety of dimensions and geometries. BISON/MOOSE solves coupled nonlinear partial differential equations, including heat conduction, mechanics, FP species transport, etc., in a fully implicit manner. More detailed descriptions of the BISON fuel performance code as it relates to TRISO fuel modeling can be found in "BISON TRISO Modeling Advancements and Validation to AGR-1 Data" [9], "Numerical Evaluation of AGR-2 Fission Product Release" [10], and "TRISO particle fuel performance and failure analysis with BISON" [11]. The Monte Carlo methodology used in BISON to calculate the failure probability of a batch of fuel particles is summarized in Figure 2 [11]. Recently, a more efficient statistical failure analysis, similar to the "fast" integration methodology in PARFUME, has been added to BISON [12].
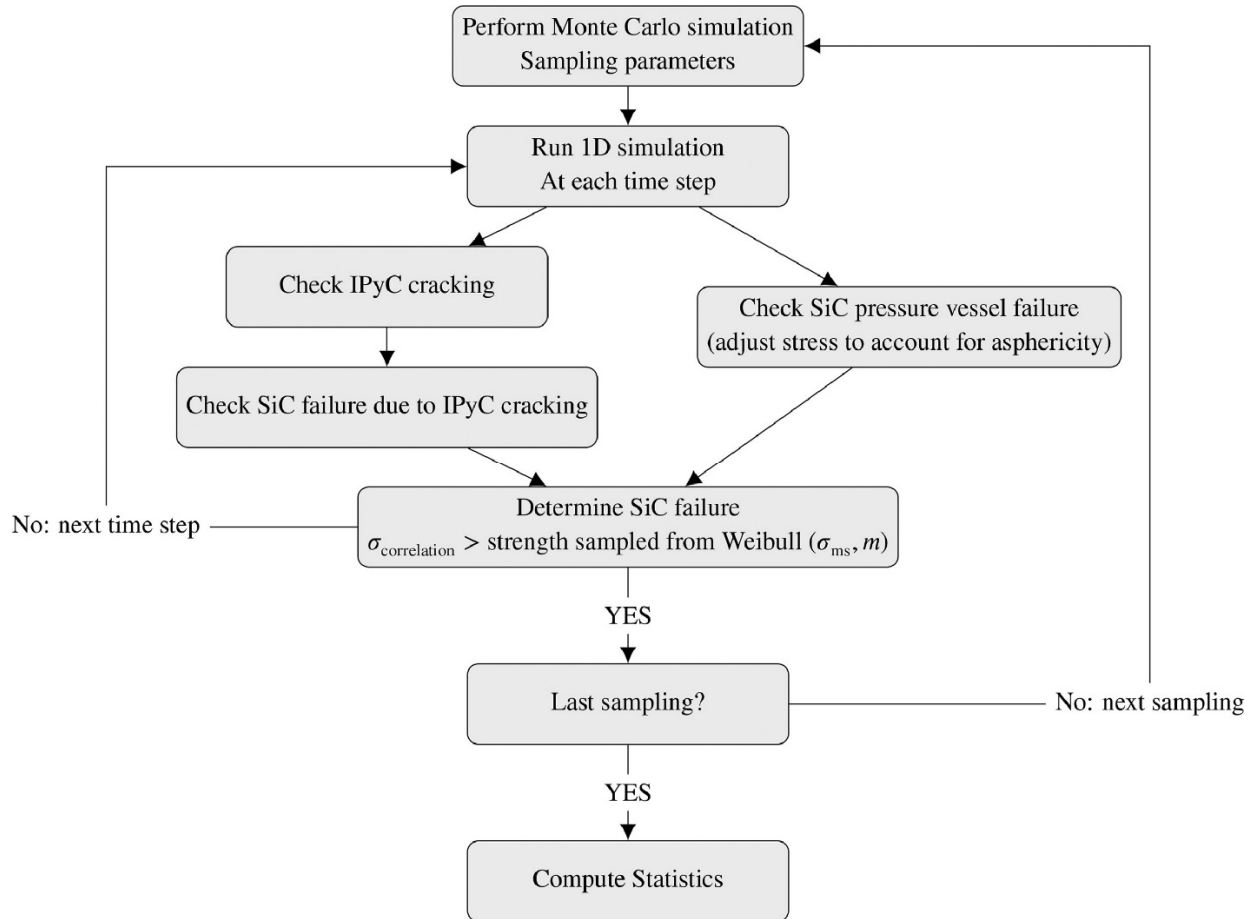
Figure 2. Monte Carlo methodology for calculating failure probability in BISON.

BISON has the capability to incorporate different irradiation conditions and run either very small analyses with a single processor or very large analyses on multiple processors on a supercomputer. For TRISO fuel, BISON supports spherically symmetric models, axisymmetric models, and full 3D models. Thermomechanical models for each material layer include elastic, irradiation creep, irradiation-induced dimension change, thermal expansion, and thermal conductivity.

FP generation, diffusion, and release can also be modeled for TRISO particles with UO_2, UCO or uranium nitride kernels. In addition, BISON has the ability to perform statistical failure analyses of large samples of fuel particles. This capability enables the evaluation of failure due to multidimensional failure phenomena by analyzing thousands of particles. This enables realistic calculations of the FP release from the many particles in a TRISO-fueled reactor.

2. AGR-3/4 IRRADIATION EXPERIMENT

As defined in the technical program plan for the INL ART/AGR fuel program [1], the objectives of the AGR-3/4 experiment are as follows:

1. Irradiate fuel containing UCO designed-to-fail (DTF) fuel particles that will provide a known source of FPs for subsequent transport through compact matrix and structural graphite materials.

2. Assess the effects of sweep gas impurities (such as CO, H_2O, and H_2) typically found in the primary coolant circuit of HTGRs, on fuel performance and subsequent FP transport.

3. Provide irradiated fuel and material samples for PIE and safety testing.

4. Support the refinement of fuel performance and FP transport models with online, PIE, and safety test data.

2.1 Fuel Characteristics

Fuel for AGR-3/4 contained conventional driver fuel similar to the baseline fuel used in the AGR-1 experiment [13] and DTF fuel particles whose kernels were identical to the driver fuel kernels and whose coatings were DTF under irradiation, leaving FPs to migrate through the surrounding materials [14] [15]:

- Driver fuel consisted of TRISO-coated particles that were slightly less than 1 mm in diameter. Each particle had a central reference kernel that contains fuel material, a porous carbon buffer layer, an IPyC layer, a SiC barrier coating, and an outer pyrolytic carbon (OPyC) layer as depicted in Figure 3. Each layer's function is described in Table 1. Kernels for AGR-3/4 consisted of UCO fuel.

- DTF fuel consisted of reference kernels with a 20-μm thick pyrolytic carbon (PyC) seal coating. This coating was DTF early in the irradiation and provide a known source of FPs.
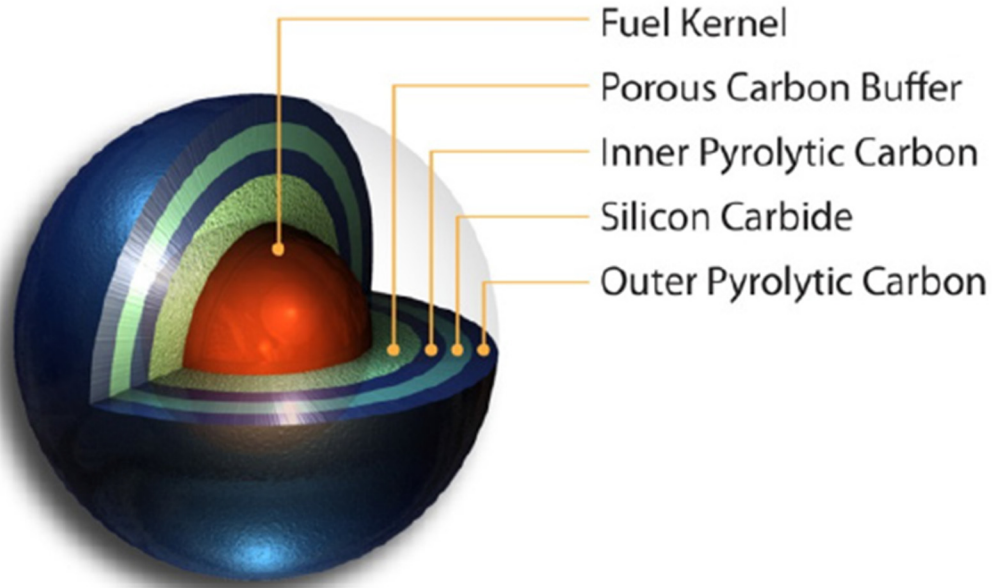
Figure 3. Typical TRISO-coated fuel particle geometry.

Table 1. Primary functions of particle fuel components.

Component	Primary Function
Kernel	Contains fissile fuel.
Buffer	Provides void space for FP gases and accommodates differential changes in dimensions between coating layers and kernel.
IPyC	Structural layer and fission gas barrier that protects the kernel during SiC deposition and the SiC layer from most FPs during irradiation.
SiC	Primary structural layer and primary FP barrier.
OPyC	Structural layer that also permits embedding the particles in graphitic matrix material.

Kernels for AGR-3/4 consisted of low-enriched uranium UCO fuel. The kernels were fabricated by BWX Technologies [16] in accordance with the AGR-3/4 DTF Fuel and Capsule Component Material Specifications [15]. The UCO kernels were coated and characterized by Oak Ridge National Laboratory [17] [18]. Coating was performed in accordance with the AGR-3/4 fuel product specification [14] [15].

After coating, AGR-3/4 fuel was formed into cylindrical compacts. The compact matrix material was composed of graphite flake and a thermosetting resin. Prior to compacting, the fuel particles were overcoated with thick layers of the compact matrix material. This overcoat was intended to prevent particle-to-particle contact and help achieve the desired packing fraction of the fuel particles. Each AGR-3/4 compact contained driver fuel particles and 20 DTF particles (about 1% of the particles) that were placed along its axis (Figure 4). AGR-3/4 compacts were nominally 12.51 mm in length and 12.31 mm in diameter. A complete description of the fuel compacts, FP monitoring system, physics analysis, and thermal analysis were presented in the final as-run report [19].
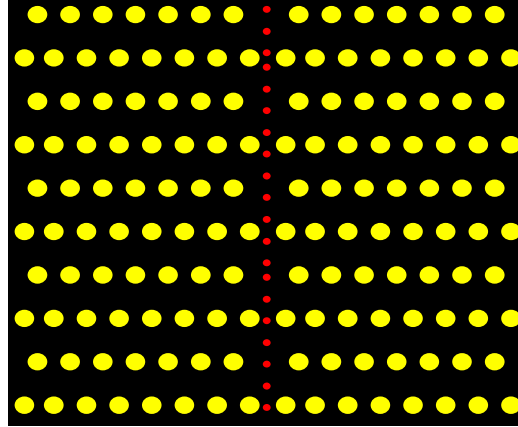
Figure 4. Schematic of an AGR-3/4 compact with DTF fuel particles along the axis.

2.2 AGR-3/4 Description

To achieve the test objectives outlined above, in accordance with requirements from the technical program plan [1] and the irradiation test specification [20], AGR-3/4 was irradiated in the northeast flux trap (NEFT) position of the ATR at INL. A cross-sectional view of the ATR core, which indicates the NEFT location, is displayed in Figure 5.
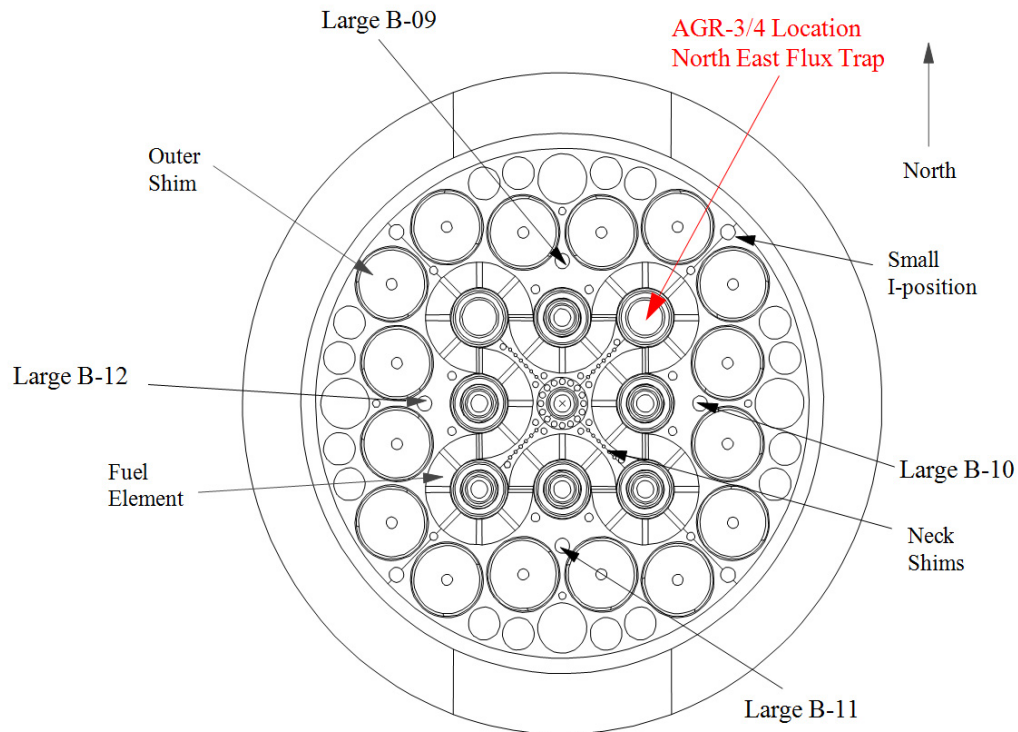
Figure 5. ATR core cross section displaying the NEFT position.

The AGR-3/4 test train was a multi-capsule, instrumented experiment designed for irradiation in the 133.4-mm diameter NEFT position of ATR. The best geometry for obtaining FP transport data was determined to be a capsule with a single stack of fuel compacts that contained a known fraction of DTF particles surrounded by three concentric annular rings of test material: an annulus of fuel-compact matrix material; an annulus of fuel-element graphite; and an annulus of graphite operating at a lower temperature to act as a sink for FPs. This configuration best reduced axial thermal gradients and, hence, axial diffusion. The test reactor's axial flux distribution and space considerations within the test train imposed a practical limit of 12 independently controlled and monitored capsules per test train. An axial view of the test train is illustrated in Figure 6. Figure 7 illustrates the radial view of a capsule.
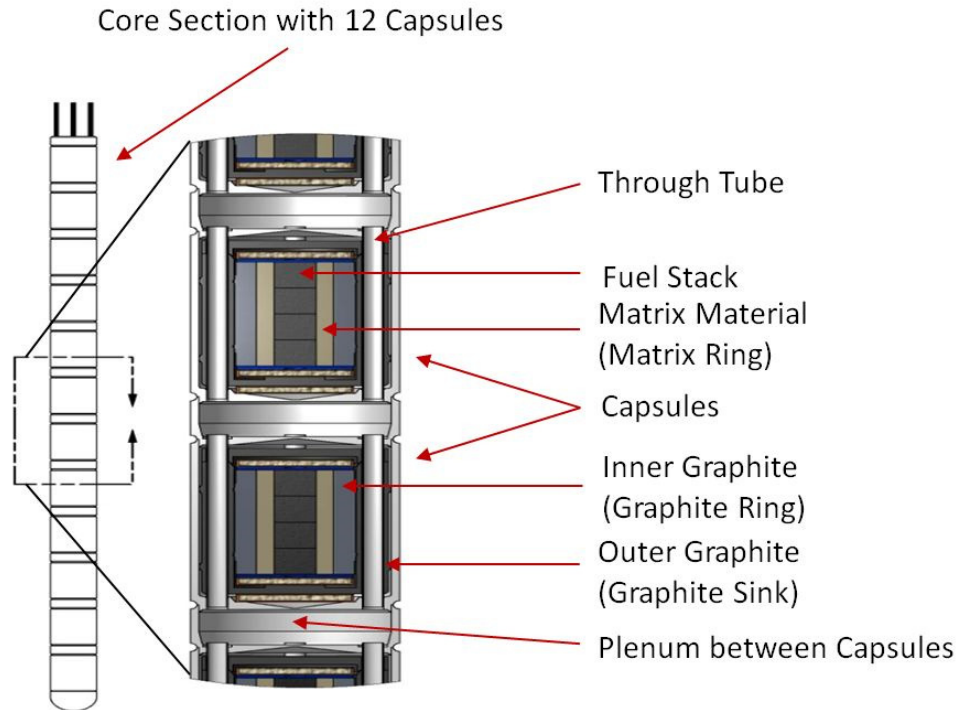
Figure 6. Axial schematic of the AGR-3/4 capsules.
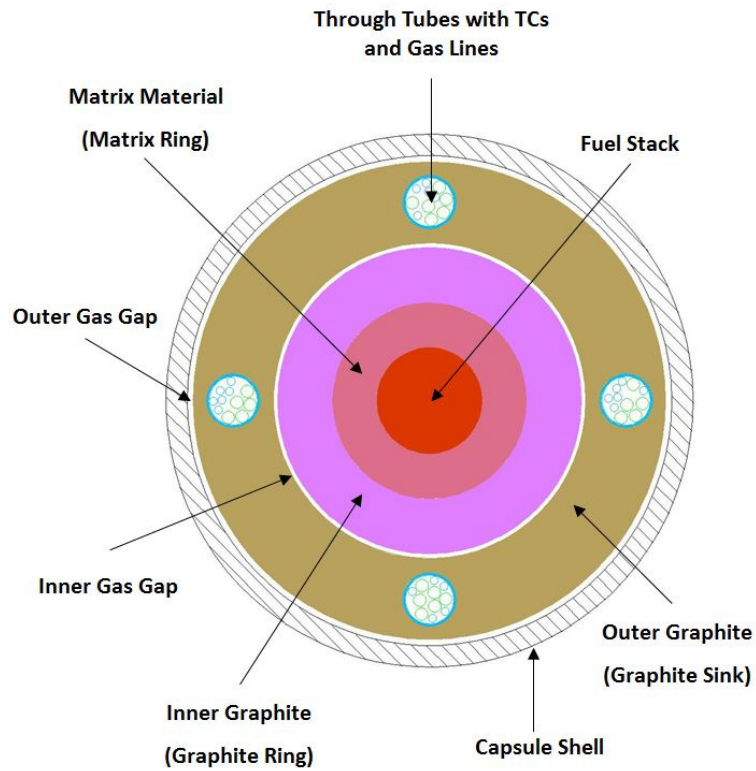
Figure 7. Radial schematic of the AGR-3/4 capsule.

Independent gas lines routed a mixture of helium and neon gases through each of the twelve capsules to provide temperature control and to sweep released FP gases to the FP monitoring system [19]. Figure 8 shows a schematic diagram of the FP monitoring system.
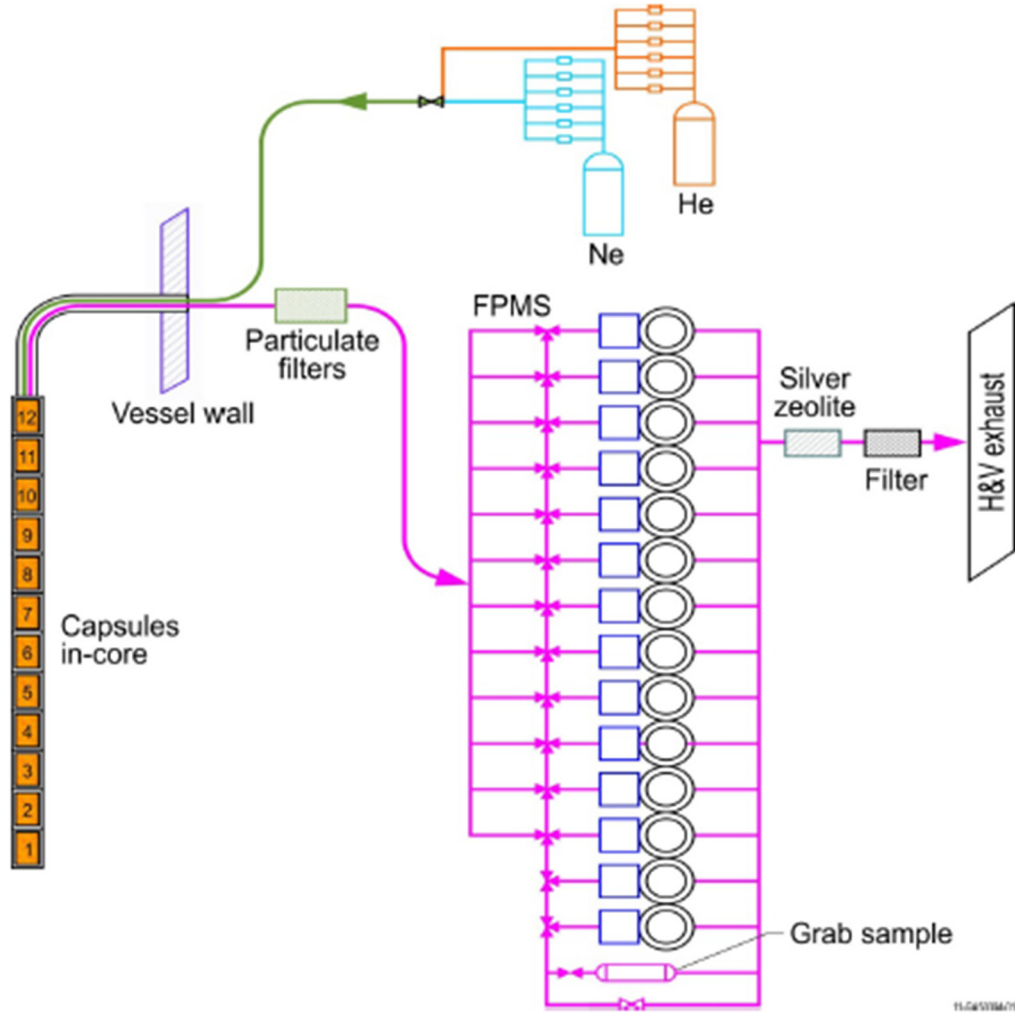
Figure 8. Simplified flow path for the AGR-3/4 sweep gas.

2.3 AGR-3/4 Irradiation

AGR-3/4 combined the third and fourth irradiation in the AGR program. Irradiation began in December 2011 and concluded in April 2014 in the ATR for a total irradiation duration of 369.1 EFPD. Final burnup values on a per compact basis ranged from 5.35 to 15.24% FIMA, while fast fluence values ranged from 1.50 to 5.31×10^{25} n/m^2 ($E_n > 0.18$ MeV). TAVA fuel temperatures on a capsule basis at the end of irradiation ranged from 854°C in Capsule 12 to 1345°C in Capsule 7. The capsule-specific fluence, burnup, and TAVA temperatures used for this study are shown in Table 2 [19].

Table 2. Capsule average thermal conditions and end-of-irradiation fluence and burnup.

Capsule	Average Fluence ($\times 10^{25}$ n/m^2) [$E_n > 0.18$ MeV]	Average Burnup (% FIMA)	TAVA (°C)
12	1.50	5.35	854
11	2.87	9.06	1226
10	3.94	11.81	1191
9	4.66	13.67	1008
8	5.08	14.52	1190
7	5.27	14.96	1345
6	5.31	15.24	1051
5	5.19	14.88	1015
4	4.85	14.21	1008
3	4.22	12.58	1177
2	3.21	10.07	1057
1	1.76	6.14	927

2.4   Post-Irradiation Examination

After irradiation, the AGR-3/4 test train was transferred to the Materials and Fuels Complex Hot Fuel and Examination Facility at INL, and PIE activities were divided into two phases [21]. The objectives of the AGR-3/4 PIE campaign are to [21]:

- Determine the distribution of fission products in matrix and graphite rings at the end of irradiation

- Determine the distribution of FPs in matrix and graphite rings at elevated temperatures following heating in pure helium and/or oxidizing atmospheres

- Determine the fractional inventory of FPs remaining in fuel kernels and the compact matrix at the end of irradiation

- Determine the fractional inventory of condensable and gaseous FP release from fuel kernels and compact matrix at elevated temperatures during heating in pure helium and/or oxidizing atmospheres.

Comparisons between PIE measurements and model predictions focused on silver, cesium, and strontium. Comparisons involving other FPs were not performed, either because of a lack of modeling input data for transport through TRISO-coated fuel particles and compacts for other species (e.g., europium), or because release was not observed in PIE (e.g., krypton). Specific irradiated compacts were selected for examination based on a detailed set of criteria, including the need to examine a range of irradiation temperatures and burnups.

Information on FP release was obtained through several different measurements. The primary means of assessing FP release was through a direct analysis of the released inventory, which included the inventory released from the compacts and measured on the irradiation capsule components. Silver represents a special case, in which the level of release from the fuel compacts can be sufficiently high (i.e., more than several percent) that the fraction retained in the compacts can be estimated by directly measuring the remaining inventory in the fuel and comparing it to the predicted inventory from physics calculations. In all cases, the measured inventory was first decay-corrected to the end of the AGR-3/4 irradiation and then compared with the predicted inventory from as-run neutronics calculations of the AGR-3/4 experiment to calculate corresponding release or retention fractions.

Gamma scanning of 32 irradiated AGR-3/4 compacts was used to determine their inventory of Ag-110m. These compacts were from Capsules 1, 3, 4, 5, 7, 8, 10, and 12. The other capsules (2, 6, 9, and 11) remained intact for heat up tests. In addition, destructive physical sampling of the capsule rings was completed by machining and milling the material on the circumference of the rings and performing gamma scans to measure the amount of FPs present.

3.   FUEL MODELING

PARFUME and BISON were used to model the AGR-3/4 experiment to determine the probability of fuel particle failure and release of the FPs silver (Ag), cesium (Cs), and strontium (Sr) from both the driver fuel and DTF fuel particles. The analysis considered conventional fuel particle failure (e.g., typical pressure vessel failure) and multidimensional failure mechanisms (e.g., IPyC cracking, pressure vessel failure associated with particle asphericity, and IPyC/SiC debonding). The two fuel performance codes did not consider any as-fabricated exposed kernels and the release fractions were calculated assuming no driver fuel particle failures at time equal to zero. Both PARFUME and BISON assume that the DTF particles are failed at the beginning of the irradiation. Key aspects of the modeling of the AGR-3/4 irradiation are described in the following subsections.

3.1   Irradiation Conditions

PARFUME and BISON are designed to evaluate fuel performance based on user inputs for neutron fluence and burnup, with a corresponding set of thermal conditions. For this analysis, compact-specific fluence and burnup results from neutronics analysis [22] and fuel temperature histories from thermal analysis [23] were performed to support the AGR-3/4 experiment campaign were used in the models. The AGR-3/4 irradiation consisted of 48 compacts [19] and the as-run PARFUME predictions were performed on a compact-level basis using the daily TAVA temperatures. The fluence, burnup, and final TAVA temperatures for all compacts are provided in Table 3 [19].

PARFUME has considerable flexibility relative to the application of thermal conditions affecting fuel particles. A user may define the thermal conditions for the outer surfaces of the fuel-bearing materials (e.g., the outer surface of a pebble in the case of a pebble bed reactor or the coolant channel surface of a unit cell containing fuel compacts in the case of a prismatic reactor) or the user may define fuel-bearing material temperatures directly. Options for the outer surfaces of fuel-bearing materials include defining either a time-dependent set of temperatures or a time-dependent set of heat transfer coefficients, with a corresponding time-dependent set of sink temperatures. Fuel-bearing material temperatures can be defined directly as time-dependent values that are applicable to the entire material or the user may divide the material into regions and supply time-dependent temperatures for each region. The direct specification of fuel-bearing material temperatures was applied here at the outer surface of the OPyC layer using the predicted irradiation temperatures [23].

PARFUME assumes all particles in a compact experience similar irradiation and thermal histories over the course of irradiation. Practically, PARFUME models one particle using the average burnup and fast neutron fluence and the volume-averaged temperature of the whole compact. In this scheme, PARFUME statistically treats a collection of particles within a range of geometrical dimensions and physical properties, but all the particles experience the same irradiation and thermal histories.

The AGR-3/4 experiment was irradiated for 369.1 EFPD and is modeled for each compact with end-of-irradiation values of burnup and fast neutron fluence summarized in Table 3. Burnup and fast neutron fluence are assumed to evolve linearly during irradiation. This assumption is validated by the nearly linear increase of the compact burnup and fast neutron fluence values reached at the end of each AGR-3/4 cycle, as reported in the AGR-3/4 as-run report [19].

Table 3. AGR-3/4 compacts end-of-irradiation TAVA temperatures and accumulated fluence and burnup.

Capsule	Compact	Fluence ($\times 10^{25}$ n/m^2)	Burnup (% FIMA)	TAVA (°C)	Capsule	Compact	Fluence ($\times 10^{25}$ n/m^2)	Burnup (% FIMA)	TAVA (°C)
	4	1.19	4.85	832		4	5.31	15.26	1032
	3	1.41	5.17	864		3	5.32	15.27	1081
	2	1.60	5.52	872		2	5.32	15.23	1078
12	1	1.80	5.87	849	6	1	5.30	15.21	1013
	4	2.61	8.42	1200		4	5.23	14.98	989
	3	2.80	8.89	1246		3	5.22	14.92	1050
	2	2.96	9.30	1252		2	5.18	14.86	1047
11	1	3.11	9.64	1205	5	1	5.14	14.74	973
	4	3.75	11.43	1168		4	4.92	14.41	996
	3	3.89	11.75	1210		3	4.89	14.29	1035
	2	4.01	11.96	1213		2	4.83	14.16	1029
10	1	4.12	12.08	1172	4	1	4.74	13.98	970
	4	4.53	13.40	983		4	4.38	12.93	1168
	3	4.63	13.63	1033		3	4.28	12.73	1205
	2	4.70	13.78	1035		2	4.17	12.49	1196
9	1	4.76	13.87	980	3	1	4.04	12.16	1138
	4	5.02	14.43	1169		4	3.44	10.65	1060
	3	5.07	14.54	1213		3	3.30	10.29	1081
	2	5.11	14.58	1213		2	3.14	9.90	1068
8	1	5.13	14.51	1165	2	1	2.95	9.43	1018
	4	5.24	14.90	1319		4	2.10	6.85	929
	3	5.27	15.00	1376		3	1.87	6.37	959
	2	5.29	15.02	1375		2	1.66	5.91	941
7	1	5.28	14.92	1311	1	1	1.42	5.43	880

Note: Compacts from Capsules 12, 10, 8, 7, 5, 4, 3, and 1 were selected for compact gamma scanning.

The thermal history evolves daily. For each compact, the daily temperatures of all the calculation nodes in a compact are averaged, and PARFUME and BISON use the resulting volume-averaged compact daily temperatures to set the thermal history of the modeled driver TRISO and DTF fuel particles. The daily temperatures are set as boundary conditions at the outer edge of the OPyC. From the OPyC boundary temperature, the codes calculate the temperature profile between the OPyC and the kernel center, considering that the temperature profile is affected throughout irradiation by the width of the gap forming between the buffer and the IPyC layer.

Daily temperatures were used in modeling because the TAVA temperatures displayed in Table 3 were determined to not be a suitable metric to correlate FP release to temperature, as they do not adequately reflect the thermal state of the compacts throughout irradiation. The compacts experienced a range of daily volume-average temperatures that could span several hundred degrees around their TAVA temperatures, resulting in a broad range of diffusivities, some of which far exceed the diffusivity values calculated at the TAVA temperatures. The diffusivities are modeled with an Arrhenius equation and exponentially decrease with inverse temperature. Consequently, diffusivity is highly sensitive to temperature, and averaging higher and lower temperatures with similar weights to compute FP release with the resulting TAVA temperature leads to an under-estimation of the diffusivity, and hence an under-estimation of the release.

As an illustration, Figure 9 shows the thermal histories of Compact 10-2 and 8-2. Both compacts have a TAVA temperature of 1213°C, but Compact 8-2 experienced the highest temperatures over the last ~90 days of irradiation. Compact 8-2 is therefore expected to yield a higher fractional release of FPs. In this example, the silver release fraction calculated with the TAVA temperature is 25% for both compacts. Using their respective daily temperatures, release fractions of 34% for Compact 10-2 and 56% for Compact 8-2 are obtained, in accordance with the Arrhenius diffusivities. When comparing to the PIE measurements, using the daily temperatures to calculate release fractions is a much better metric to account for the effect of temperature on FP release.
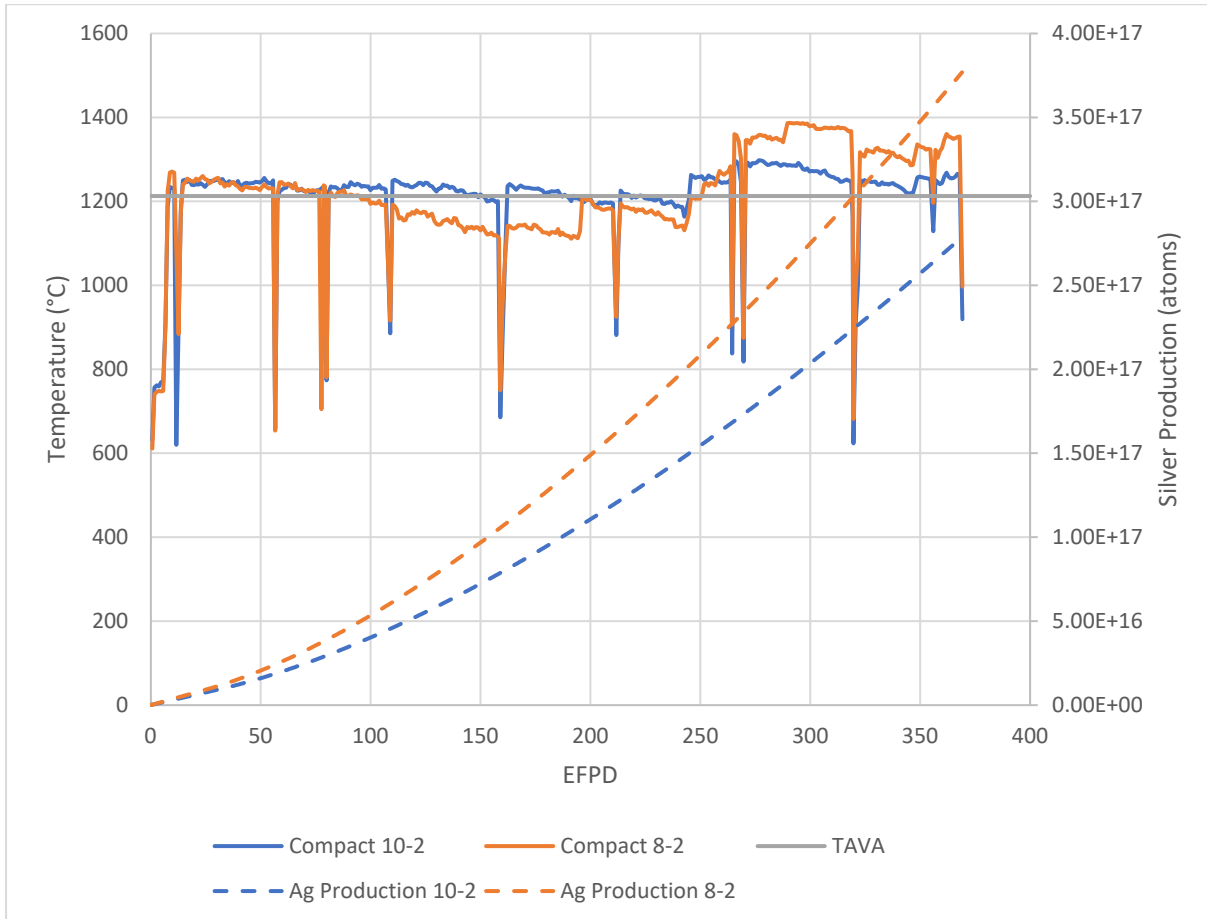
Figure 9. Evolution of daily temperatures and silver production throughout irradiation for Compact 10-2 and Compact 8-2.

3.2 Input Parameters

The PARFUME input parameters needed to model the AGR-3/4 irradiation experiment are provided in Table 4. They originate from:

- The AGR-3/4 Irradiation Test Final As-Run Report [19] for the fuel characteristics, particle geometry, compact characteristics, and material non-mechanical properties.

- A Combustion Engineering/General Atomics (CEGA) Corporation report for the material mechanical properties [24].

Table 4. Parameters used in PARFUME to model the AGR-3/4 irradiation test.

Category	Parameter	Value
Fuel characteristics	U^{235} enrichment (wt%)	19.717
	Oxygen/uranium (atomic ratio)	1.43
	Carbon/uranium (atomic ratio)	0.361
Particle geometry	Kernel diameter (μm)	357.3 ± 10.5
	Buffer thickness (μm)	109.7 ± 7.7
	IPyC thickness (μm)	40.4 ± 2.3
	SiC thickness (μm)	33.5 ± 1.1
	OPyC thickness (μm)	41.3 ± 2.1
	Particle asphericity @ SiC (aspect ratio)	1.056
Compact characteristics	Diameter (mm)	12.31
	Number of driver particles per compact	1872
	Number of DTF particles per compact	20
	Compact matrix density (g/cm^3)	1.603
	Uranium contamination fraction	3.5×10^{-5}
Material properties	IPyC Weibull modulus	9.5
	SiC Weibull modulus	6
	OPyC Weibull modulus	9.5
	IPyC / SiC bond strength (MPa)	100
	PyC Poisson's ratio in creep	0.5
	PyC creep coefficient amplifier	2
	Kernel density (g/cm^3)	11.098
	Buffer density (g/cm^3)	1.10
	IPyC density (g/cm^3)	1.904 ± 0.014
	OPyC density (g/cm^3)	1.900 ± 0.012
	IPyC (post compact anneal) BAF	1.027 ± 0.002
	OPyC (post compact anneal) BAF	1.021 ± 0.002
DTF property	Pyrocarbon thickness (μm)	20.0 ± 0.9
	pyrocarbon density (g/cm^3)	1.988 ± 0.009
	Anisotropy	1.243 ± 0.019

In addition, diffusion coefficients used for FP transport are derived from the International Atomic Energy Agency (IAEA) Technical Document 978 [25] and are discussed further below.

Statistical variations are considered relative to the fuel attributes listed in Table 5 where the standard deviation is provided. This includes particle geometry, PyC densities, and PyC BAF.

The material mechanical properties used in PARFUME are obtained from a report compiled by the CEGA Corporation [24]. Table 4 displays parameters used in PARFUME. Material properties directly incorporated into the PARFUME source code have been previously discussed in detail [2] [26] [27].

3.3 Fission Product Transport

FP transport in PARFUME is based on coding extracted from the Tritium Migration Analysis Program Version 4 (TMAP4) [28]. Originally developed to assist in the evaluation of tritium losses from fusion reactor systems, TMAP4 incorporates a one-dimensional diffusion capability that determines the thermal response of structures and solves equations for solute atom movement through surfaces and in bulk materials.

The coding extracted from TMAP4 was modified for use within PARFUME to calculate FP transport from the kernel through the successive coating layers of a TRISO-coated fuel particle, from individual TRISO-coated particles to the surrounding matrix, and from the surrounding matrix to the outside of the fuel sphere or compact, which constitutes the release of the FPs.

FP transport in PARFUME is a three-step process that includes a fuel element (e.g., cylindrical fuel compact comprised of many TRISO particles embedded in a graphitic matrix) thermal analysis, thermal and FP transport analysis for fuel particles, and a fuel element FP transport analysis ultimately leading to FP release. Thermal analyses are performed to incorporate the temperature dependence of diffusion. Diffusion is first calculated for individual fuel particles. Results from each particle then serve as time- and position-dependent FP sources for the subsequent fuel element transport analysis.

FP transport was calculated for FP silver (Ag), cesium (Cs), and strontium (Sr). Diffusion coefficients used in PARFUME for each of these species in the successive coating layers and matrix are derived from IAEA [25] and displayed in Table 5. The corresponding diffusivities can be calculated using these diffusion coefficients in the following Arrhenius-type equation:

$$D = D_{0,1}e^{-\frac{Q_{0,1}}{RT}} + D_{0,2}e^{-\frac{Q_{0,1}}{RT}}$$

where:

$D_{0,i}$ = pre-exponential factor (m²/s)

$Q_{0,i}$ = activation energy (kJ/mol)

R = gas constant (8.3142×10^{-3} kJ/mol/K)

T = temperature (K)

The diffusion coefficients in Table 5 have been derived from the evaluation of numerous irradiation and heating experiments. They are defined as "effective" diffusion coefficients, "effective" meaning that all possible transport mechanisms are summarized in a single transport process. The use of these effective diffusion coefficients is to be considered with care. These coefficients were determined for UO_2 fuel and associated particle coatings of older German fabrication, whose properties (such as microstructure) are different than those of the UCO fuel and coatings of the AGR-3/4 experiment. Similar measurements for UCO fuel kernels (which can vary in stoichiometry) do not exist. Furthermore, in many cases, the coefficients employed here are partly based on data from post-irradiation heating tests, which do not consider possible irradiation effects (such as radiation-induced segregation) and are conducted at higher temperatures than usual irradiation experiments. Consequently, IAEA diffusivities are not necessarily well adapted to model the FP transport of the AGR-3/4 UCO fuel irradiation experiment.

Table 5. Diffusion coefficients used in PARFUME.

Specie	$D_{0,i}$ (m²/s) $Q_{0,i}$ (kJ/mol)	Kernel[a]	Buffer	IPyC/OPyC	SiC	Matrix Graphite[b]
Ag	$D_{0,1}$	6.70E-09	1.00E-08	5.30E-09	3.60E-09	1.6
	$Q_{0,1}$	165	0	154	215	258
	$D_{0,2}$	--	--	--	--	--
	$Q_{0,2}$					
Cs	$D_{0,1}$	5.60E-08	1.00E-08	6.30E-08	5.50E-14	3.60E-04
	$Q_{0,1}$	209	0	222	125	189
	$D_{0,2}$	5.20E-04	--	--	1.60E-02	--
	$Q_{0,2}$	362			514	
Sr	$D_{0,1}$	2.20E-03	1.00E-08	2.30E-06	1.20E-09	1.00E-02
	$Q_{0,1}$	488	--	197	205	303
	$D_{0,2}$	--	--	--	1.80E+06	--
	$Q_{0,2}$				791	

a. Diffusivities used for UCO kernels were obtained from UO_2 data.
b. Diffusivity in the matrix was set to 10^{-6} m²/s in cases where the release at the particle level was needed for comparison to experimental data.

The diffusivities of silver, cesium, and strontium as a function of temperature in the successive layers of a particle and compact are provided in the figures below. From these figures, the following conclusions can be drawn:

- Silver (Figure 10): SiC is the main retentive barrier, but the kernel and PyC are also slightly retentive. Considering the dimensions of the TRISO particle, the diffusion time through the kernel is not negligible compared to the diffusion time through the SiC layer. However, at the AGR-3/4 temperatures, these diffusion times are small compared to the irradiation length, and silver is not predicted to be well retained over the course of irradiation.

- Cesium (Figure 11): as with silver, the SiC layer is the main retentive barrier, but to a much larger extent than the kernel. The Cs diffusivity in SiC is about two orders of magnitude lower than for Ag in SiC. The kernel is also more retentive to cesium than it is to silver, which is an important factor in the case of particles with failed SiC layers. Because of its lower diffusivities, cesium is better retained than silver in both the kernel and SiC layer.

- Strontium (Figure 12): unlike cesium and silver, strontium is primarily retained by the kernel itself. The combination of a larger thickness and a lower diffusivity compared to the SiC layer makes the kernel the first barrier to Sr release. Therefore, strontium release is less affected by the failure of the SiC layer than Cs, for example, and because of its low kernel diffusivity, strontium is well retained by the TRISO fuel at the AGR-3/4 temperatures.
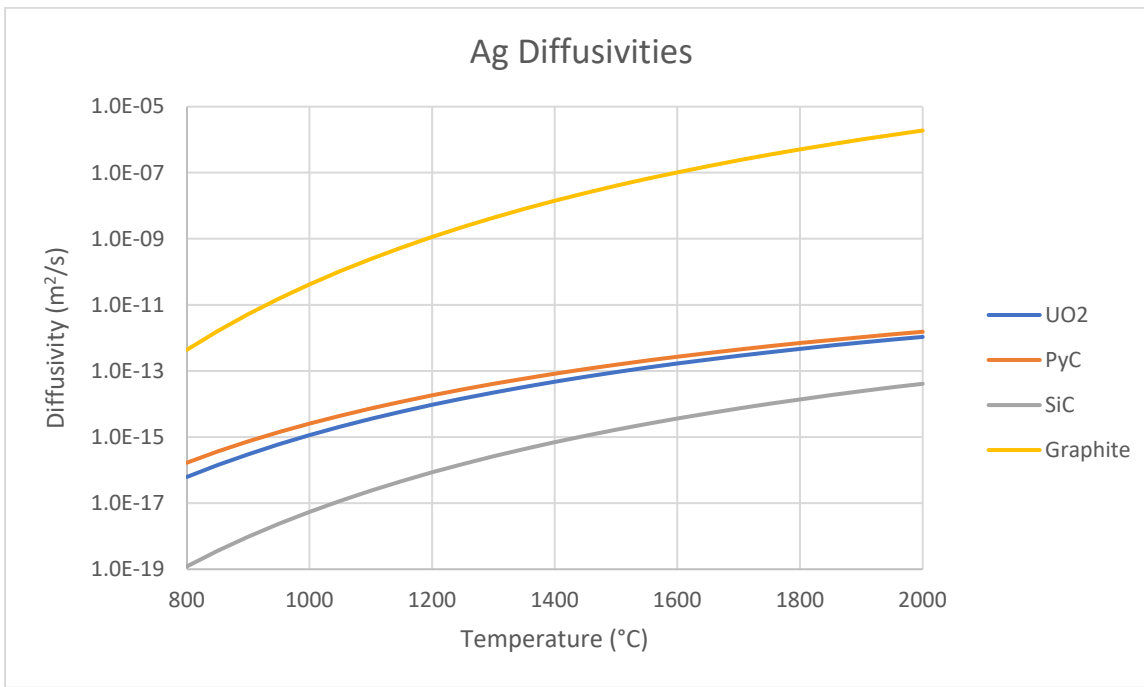
Figure 10. Silver diffusivities.
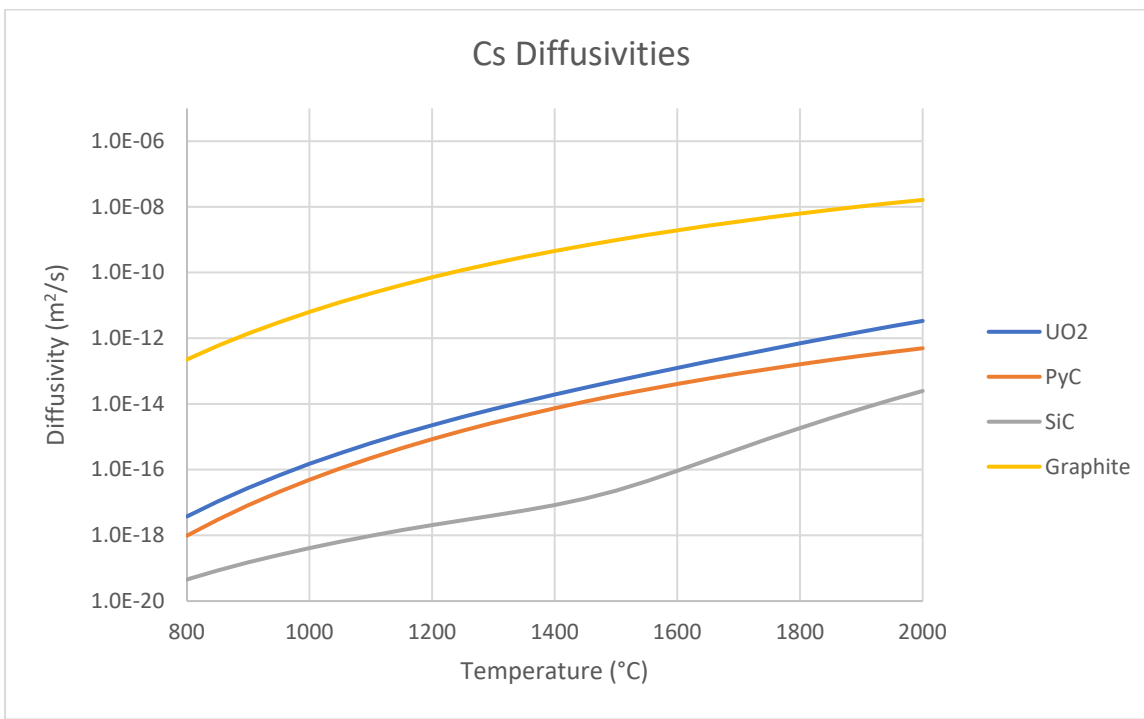
Figure 11. Cesium diffusivities.
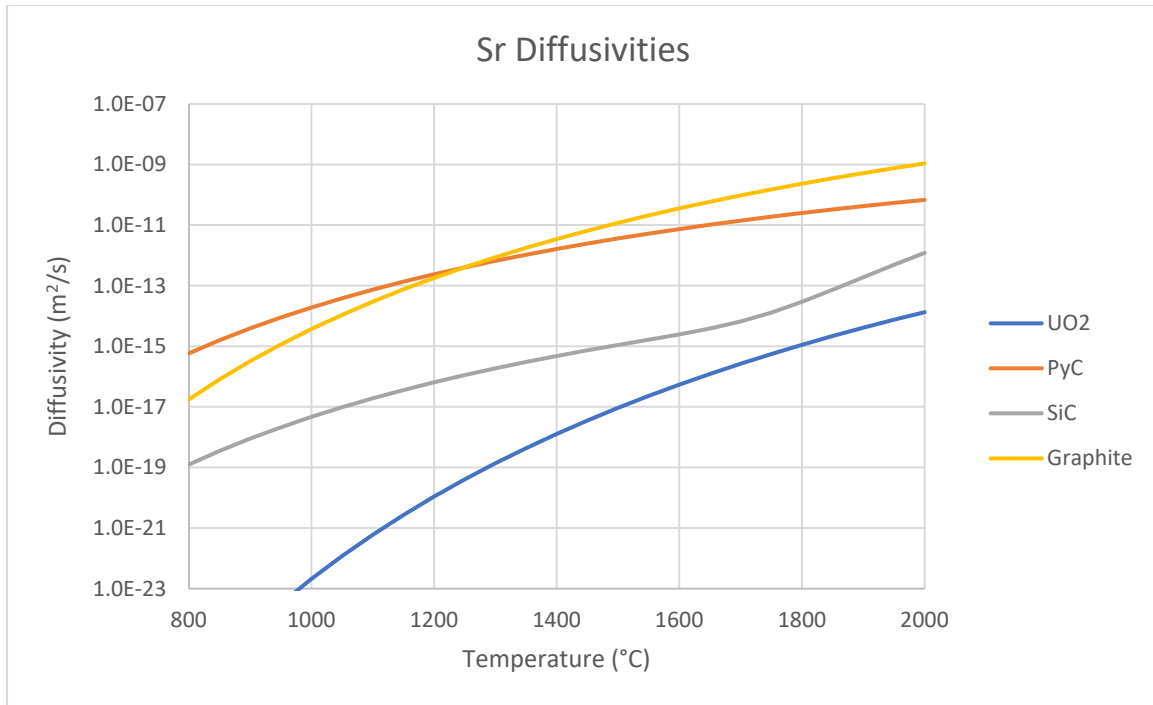
Figure 12. Strontium diffusivities.

The release of FPs is calculated at the compact level after the FPs were transported through the TRISO particle and surrounding compact. FPs are considered released once they reach the compact edge. The fractional release of FPs is then calculated by normalizing the calculated release from the compact to the calculated kernel source or inventory.

To assess the release at the particle level, (i.e., the FPs that are released from the TRISO particle into the compact matrix), PARFUME can be modified to force diffusion through the matrix. This is done by adjusting the diffusivity of the matrix graphite to a value of 10^{-6} m^2/s. With this adjustment, the release PARFUME calculates at the edge of the compact corresponds to the release from the TRISO particles.

In PARFUME, the calculation of FP transport through a collection of particles is weighted by the probability of the failure of these particles. The statistical variations in the modeling parameters of Table 4 are used in the thermomechanical stress analysis to determine any layer failure, at which point the diffusivity of that layer is set to 10^{-6} m^2/s, corresponding to a loss of retentive capability. This relies on the strong assumption that a failed layer does not retain diffusing species at all, even partially, and it is implemented as such for lack of a better understanding of the diffusing mechanisms in failed layers. The resulting release from the collection of particles includes release from the driver fuel particles as well as release from the DTF particles.

To more accurately reproduce the number of particles with retentive and non-retentive coating layers, driver fuel particles and DTF particles were modeled separately. PARFUME has the capability to separately model driver fuel particles and DTF particles by decoupling the two particle types. PARFUME is run twice, once modeling the driver fuel particles with the IAEA diffusivities and once again with DTF particles, where it is assumed that the DTF particles fail early in irradiation and the kernel and PyC layer diffusivities are set to 10^{-6} m^2/s. This results in separate release fractions from driver fuel particles and DTF particles, which can then be combined accordingly in each compact to compare to the measured release data. A similar approach was performed using BISON.

4.   COMPACT GAMMA SCANNING

Gamma scanning was performed on the 32 irradiated compacts listed in Table 3 to determine their inventories of Ag-110m. The irradiation characteristics of the selected compacts cover a wide range of TAVA temperatures; however, high and low burnup values (and corresponding fluence values) are only represented in the selected compacts, as illustrated in Figure 13. The irradiation characteristics of all the compacts listed in Table 3 are illustrated in Appendix A.
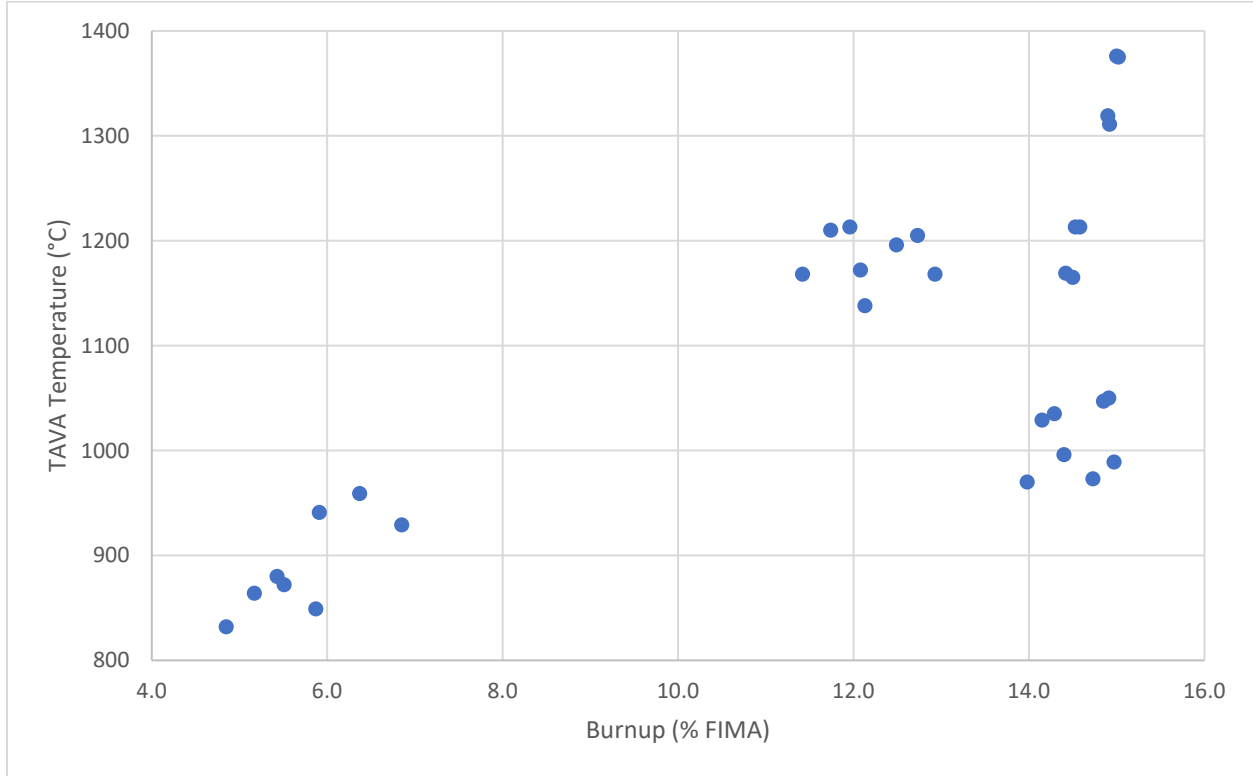
Figure 13. Compact TAVA temperatures versus burnup selected for gamma scanning.

4.1   Measured Silver Release Versus Predicted

The measured retention fraction was obtained by dividing the inventory measured in the compact from gamma scanning [29] by the total inventory of silver produced during irradiation, as calculated by as-run coupled neutronics and depletion models [22]. The measured release fraction is equal to one minus the measured retention fraction. Since the retention/release fractions rely on both measured and calculated values, they are subject to uncertainties from both measured and calculated biases. This can lead to a considerable bias on the values being reported. For example, the measured Ag-110m inventory in Capsules 1 and 12 (low TAVA temperature capsules) have rather large uncertainties [30]. In the case of Capsule 12, this can be as much as 80%. These low temperature capsules should be used with caution to quantify any conclusions regarding silver release due to their large uncertainties. In addition, the ratio of measured to calculated values reported in PIE literature is not referred to as the retained values but for this analysis, it assumes that the calculated values are correct, and therefore the release fractions can be estimated. This again does not take into consideration the uncertainties associated with the measured values, which can be appreciable.

The PIE measurements and PARFUME predictions for the 32 selected compacts are summarized in Table 6 and illustrated in Figure 14. Compacts in Figure 14 are numbered in the order presented in Table 6, with Compact 12-4 as the first entry and Compact 1-1 as the last data point. Appendix B displays break-down plots for each capsule. Figure 15 and Figure 16 show the difference between the calculated and measured silver release fractions from compact gamma scanning for the eight capsules as a function of TAVA temperature and burnup.

Table 6. Ag measured and calculated release fraction.

No.	Compact	Fluence (× 10^{25} n/m^2)	Burnup (% FIMA)	TAVA (°C)	PIE Release Fraction	PARFUME Calculated Release Fraction		
						Driver	DTF	Combined
1	12-4	1.19	4.85	832	7.72E-01	7.84E-05	8.31E-01	8.86E-03
2	12-3	1.41	5.17	864	7.88E-01	6.99E-05	9.13E-01	9.72E-03
3	12-2	1.60	5.52	872	5.62E-01	6.97E-05	9.26E-01	9.85E-03
4	12-1	1.80	5.87	849	3.37E-01	7.89E-05	8.84E-01	9.43E-03
5	10-4	3.75	11.43	1168	9.50E-01	2.07E-01	9.97E-01	2.15E-01
6	10-3	3.89	11.75	1210	9.15E-01	3.32E-01	9.97E-01	3.39E-01
7	10-2	4.01	11.96	1213	8.04E-01	3.42E-01	9.97E-01	3.49E-01
8	10-1	4.12	12.08	1172	8.45E-01	2.17E-01	9.97E-01	2.25E-01
9	8-4	5.02	14.43	1169	8.40E-01	3.93E-01	9.98E-01	4.00E-01
10	8-3	5.07	14.54	1213	8.37E-01	5.55E-01	9.98E-01	5.60E-01
11	8-2	5.11	14.58	1213	8.57E-01	5.56E-01	9.98E-01	5.61E-01
12	8-1	5.13	14.51	1165	8.22E-01	3.82E-01	9.98E-01	3.88E-01
13	7-4	5.24	14.90	1319	8.50E-01	7.81E-01	1.00E+00	7.83E-01
14	7-3	5.27	15.00	1376	8.79E-01	8.78E-01	1.00E+00	8.79E-01
15	7-2	5.29	15.02	1375	8.89E-01	8.77E-01	1.00E+00	8.78E-01
16	7-1	5.28	14.92	1311	8.74E-01	7.64E-01	1.00E+00	7.67E-01
17	5-4	5.23	14.98	989	2.97E-01	1.79E-03	9.95E-01	1.23E-02
18	5-3	5.22	14.92	1050	2.28E-01	2.51E-02	9.97E-01	3.54E-02
19	5-2	5.18	14.86	1047	1.94E-01	2.28E-02	9.97E-01	3.31E-02
20	5-1	5.14	14.74	973	3.17E-01	7.23E-04	9.95E-01	1.12E-02
21	4-4	4.92	14.41	996	2.91E-01	2.75E-03	9.96E-01	1.32E-02
22	4-3	4.89	14.29	1035	3.29E-01	1.56E-02	9.97E-01	2.60E-02
23	4-2	4.83	14.16	1029	2.87E-01	1.27E-02	9.97E-01	2.31E-02
24	4-1	4.74	13.98	970	3.41E-01	6.60E-04	9.95E-01	1.12E-02
25	3-4	4.38	12.93	1168	9.51E-01	1.76E-01	9.98E-01	1.84E-01
26	3-3	4.28	12.73	1205	9.08E-01	2.76E-01	9.99E-01	2.83E-01
27	3-2	4.17	12.49	1196	9.29E-01	2.52E-01	9.99E-01	2.60E-01
28	3-1	4.04	12.16	1138	9.36E-01	1.17E-01	1.00E+00	1.27E-01

No.	Compact	Fluence ($\times 10^{25}$ n/m^2)	Burnup (% FIMA)	TAVA (°C)	PIE Release Fraction	PARFUME Calculated Release Fraction		
						Driver	DTF	Combined
29	1-4	2.10	6.85	929	1.90E-01	6.52E-05	9.95E-01	1.06E-02
30	1-3	1.87	6.37	959	1.78E-01	2.82E-04	9.97E-01	1.08E-02
31	1-2	1.66	5.91	941	4.41E-01	1.04E-04	9.96E-01	1.06E-02
32	1-1	1.42	5.43	880	2.39E-01	7.20E-05	9.85E-01	1.05E-02
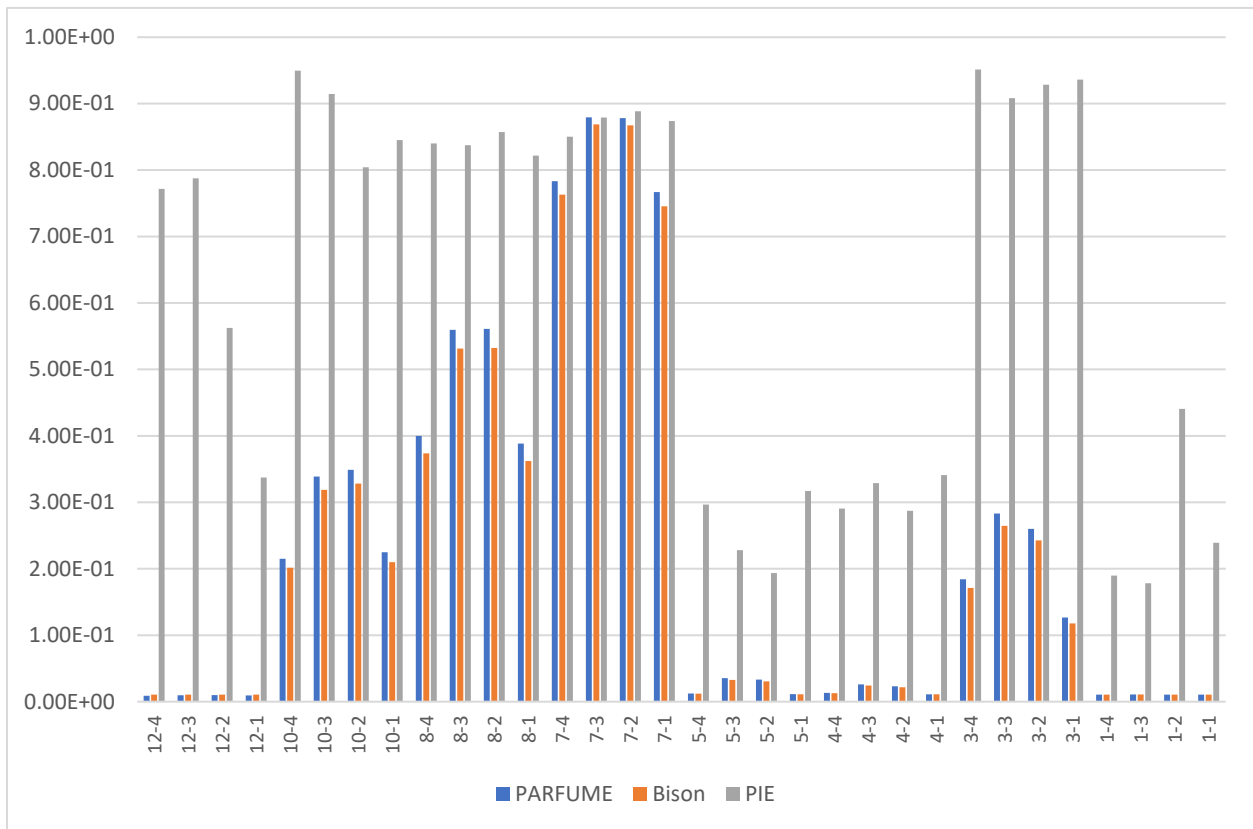
Figure 14. Predicted versus measure silver release fraction from compact gamma scanning.
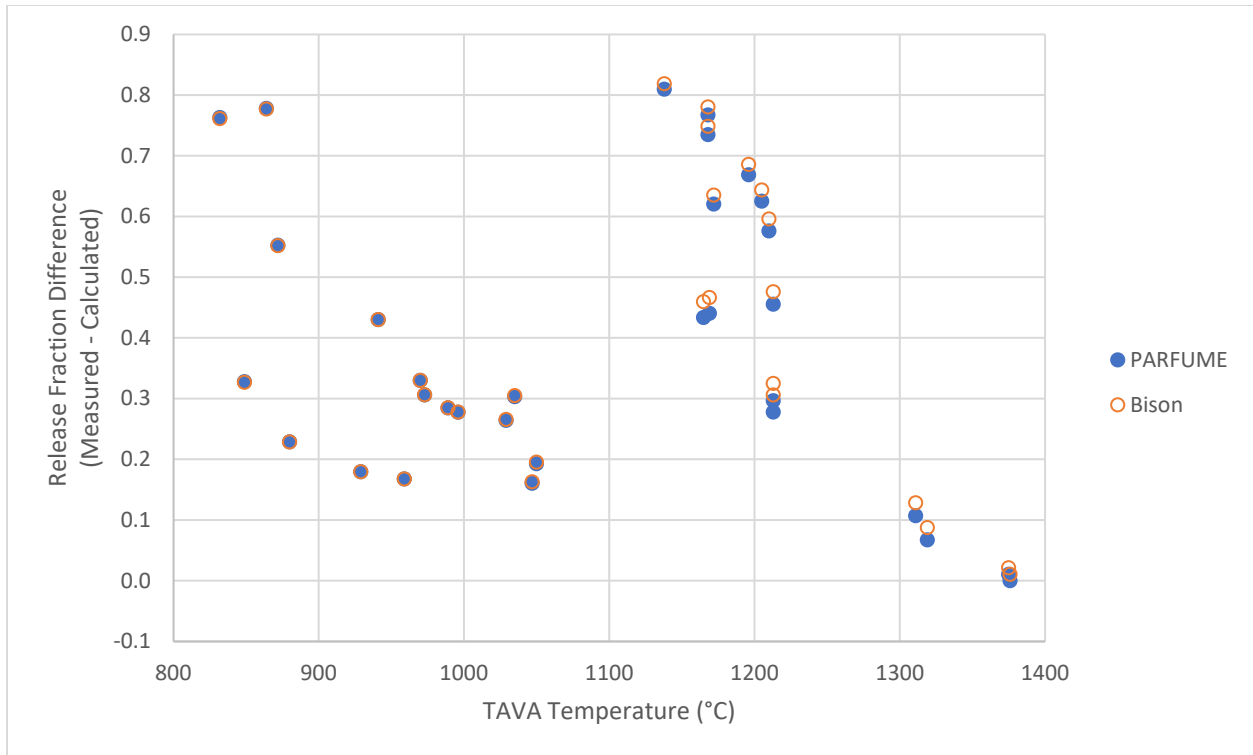
Figure 15. Difference between calculated and measured release fraction versus TAVA temperature.
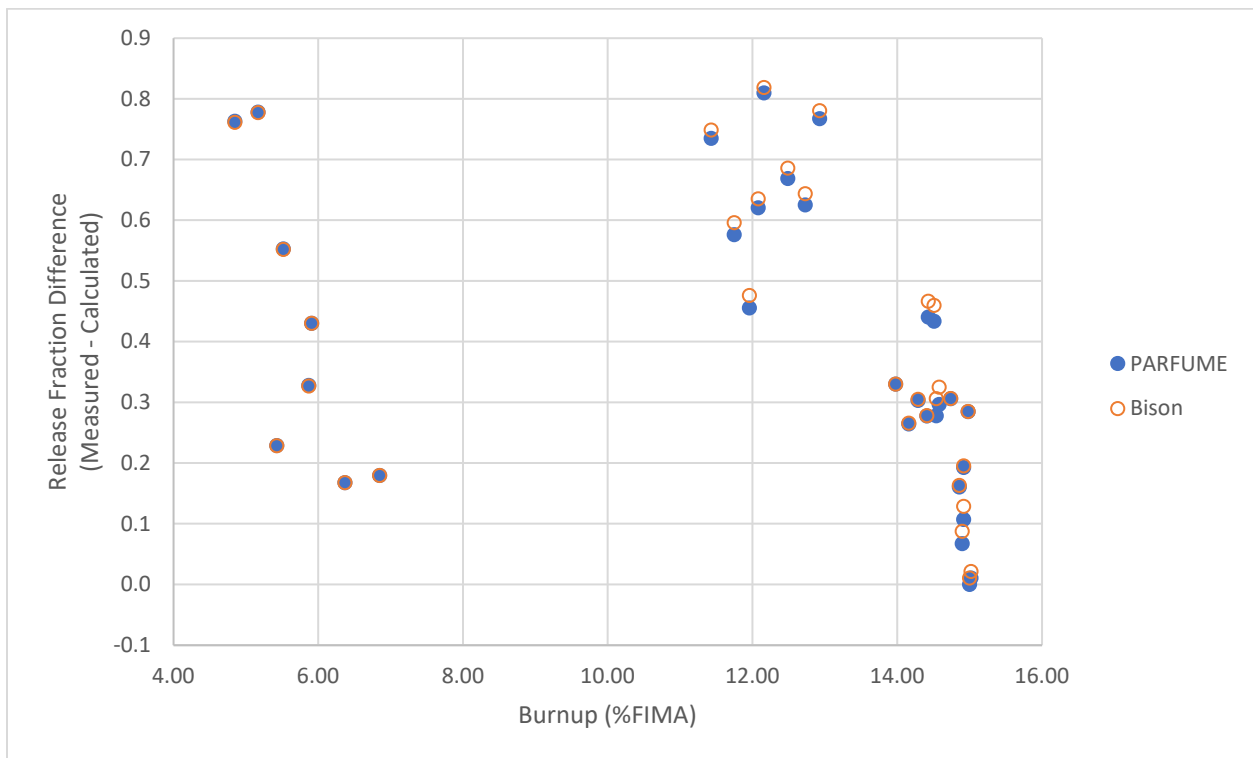
Figure 16. Difference between calculated and measured release fraction versus burnup.

Based on the results presented in the figures above, the following observations can be made:

- The silver release fractions calculated by PARFUME and BISON were in good agreement

- Both codes under-predict PIE silver release fractions in UCO compacts

- PARFUME and BISON under-predict silver release in UCO compacts regardless of burnup levels and no correlation can be made

- The under-prediction of UCO fuel is consistent with previous predictions from AGR-1 PIE [4] and AGR-2 PIE [5].

4.2   Discussion and Analysis of Silver Release

PARFUME consistently underpredicts the silver release fraction when compared to the measured data inferred from compact gamma scanning. This can be partly attributed to the temperature spatial distribution exhibited through the compact as well as the spatial distribution of the silver source. These phenomena are further discussed below.

4.2.1   Release Fraction Versus Temperature

As previously discussed, TAVA temperatures are not a suitable metric to correlate silver release to temperature because they do not adequately reflect the thermal state of the compacts throughout irradiation. Daily temperatures were therefore used to calculate the predicted silver release. In addition to their distribution around the compact TAVA temperature, the daily temperatures also widely vary spatially throughout a compact. As illustrated in Figure 17, daily temperatures can range significantly from the cold side to the hot side of a compact [23], which can lead to a significant range in silver release from one particle to another.
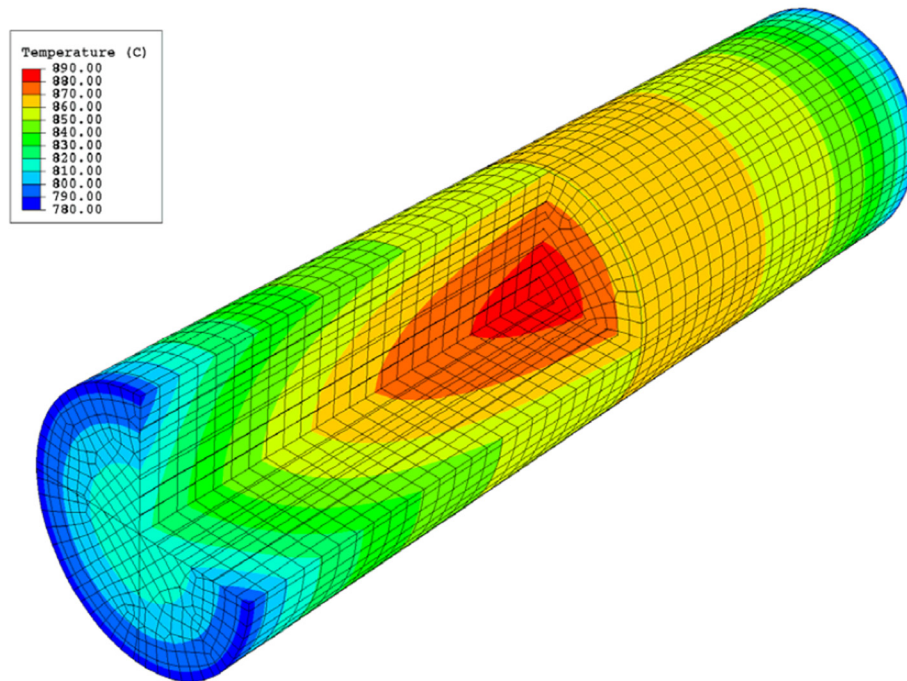
Figure 17. Cut-away view of a typical temperature (°C) contour plot of a capsule.

The temperature spatial distributions in the AGR-3/4 compacts were obtained from as-run thermal analysis [23]. Because of the large number of thermal nodes (roughly one node per particle), PARFUME could not be used to calculate the silver release of every single node. The predictions for silver release are based on the behavior of an average particle within each compact, whereas PIE measurements reflect the behavior of individual particles experiencing a broader set of daily temperatures because of their spatial locations all over the compact.

The discrepancy observed between the calculated values and PIE when comparing the average fractional release (or retained fraction) can be largely attributed to the wide distribution of temperatures experienced by compact during irradiation. PARFUME and BISON use the volume-average daily temperatures to compute the average fractional release for each compact but the release fraction of a particle bearing the volume-average daily temperatures is not equivalent to the average of the release fractions of all individuals particles in the compact because the diffusivity does not vary linearly with temperature. Therefore, using the volume-average daily temperatures underestimates the release by neglecting the relatively larger release of hotter particles. This causes a discrepancy between the calculated values and PIE when comparing fractional release from compact gamma scanning.

As-run calculations report uncertainties on the calculated temperatures up to 100°C [19]. Although no temperature bias was reported, Figure 18 shows the impact of a temperature change on the silver release calculated by PARFUME. Compacts in Figure 18 are numbered in the order presented in Table 6. For each of the 32 gamma scanned compacts, the temperature was adjusted in 50°C increments in PARFUME calculations to attempt to match the PIE release. For instance, the daily temperatures of Compact 5-3 were increased by 100°C so the resulting calculated release fraction would more closely match the measured release fraction of the compact, the increase was 50°C for Compact 7-1, and so forth. Figure 18 displays the PIE data and PARFUME predictions with the release predictions obtained after the temperature changes. Only two compacts did not require a temperature adjustment in the PARFUME prediction, Compacts 7-3 and 7-2. Figure 18 shows that the PARFUME predictions are sensitive to the individual compact temperatures and adjusting the as-run daily TAVA temperatures can improve the calculated release fraction results when compared to PIE data. Since the calculated release fractions by PARFUME and BISON were in agreement, only one fuel performance modeling code (PARFUME) was used to complete this sensitivity study.
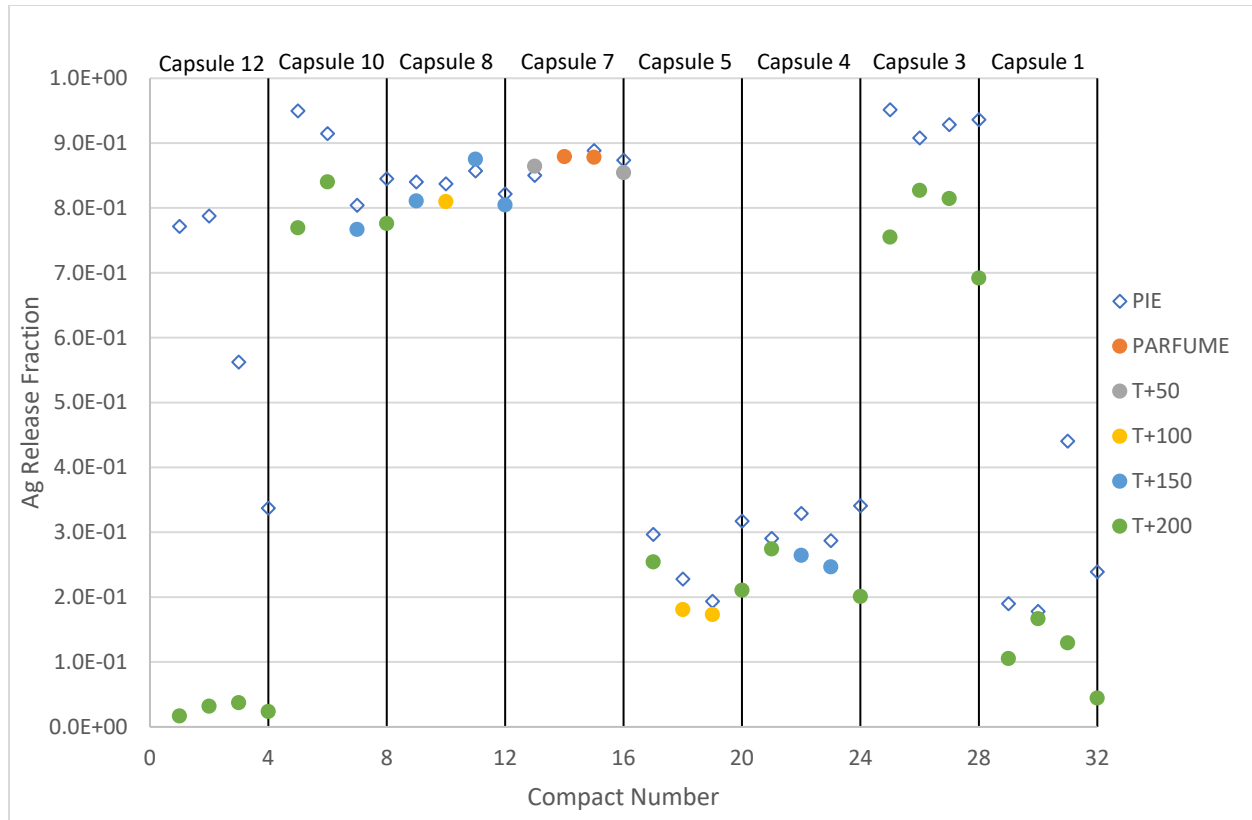
Figure 18. Effect of temperature adjustments on calculated silver release (numbering following the order in Table 6).

Table 7 gives a summary of the impact of temperature change on silver release. For each temperature adjustment, Table 7 shows the range of initial PARFUME release fractions for the compacts affected by that temperature adjustment (Compacts 7-4 and 7-1 for a temperature adjustment of 50°C, for instance) and the range of release fractions calculated by PARFUME after the temperature adjustment. As an example, the impact of the release fraction due to an increase in temperature on selected compacts is presented in Figure 19.

Table 7. Effect of temperature adjustment on calculated silver release.

Temperature Adjustment	Initial Release Fraction Range	Adjusted Release Fraction Range
+50°C	$7.7×10^{-1} – 7.8×10^{-1}$	$8.6×10^{-1} – 8.6×10^{-1}$
+100°C	$3.3×10^{-2} – 5.6×10^{-1}$	$1.7×10^{-1} – 8.1×10^{-1}$
+150°C	$2.3×10^{-2} – 5.6×10^{-1}$	$2.5×10^{-1} – 8.7×10^{-1}$
+200°C	$8.9×10^{-3} – 3.4×10^{-1}$	$1.7×10^{-2} – 8.4×10^{-1}$
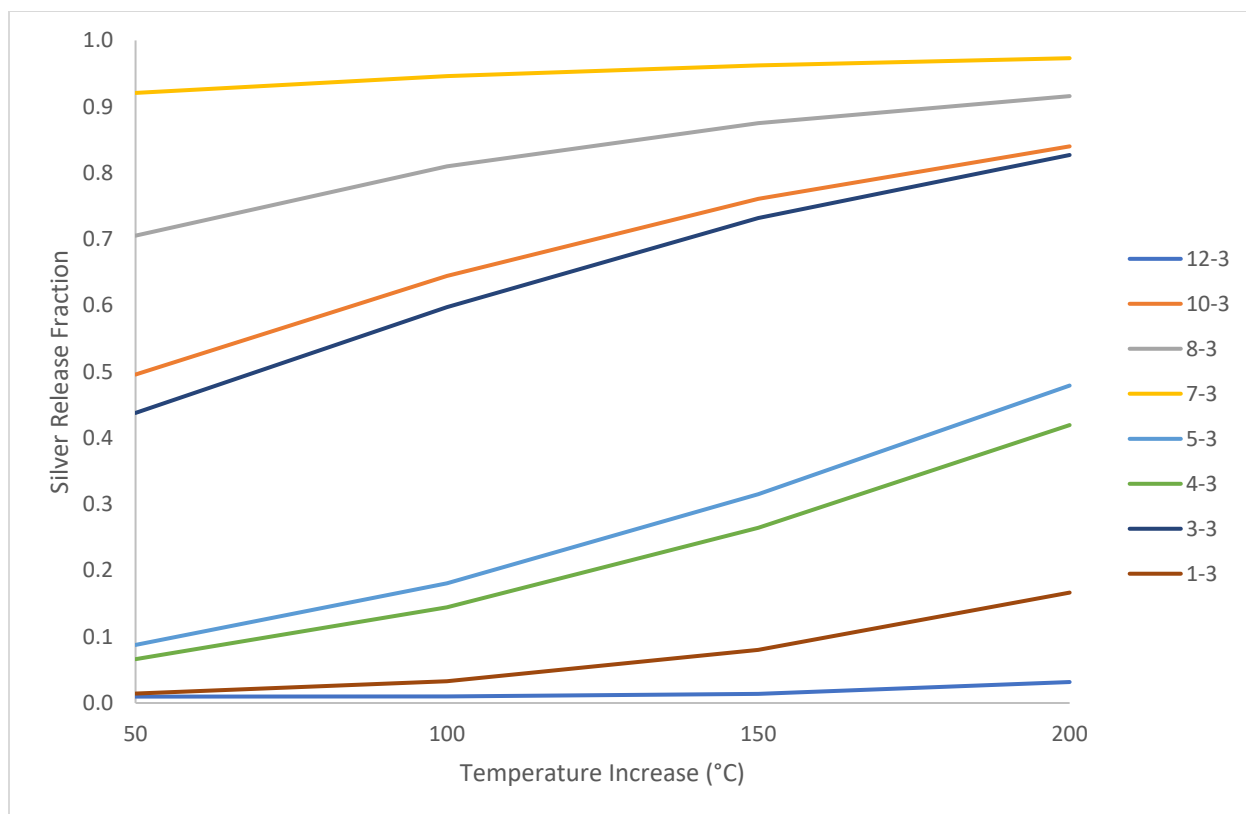
Figure 19. Effect of incremental temperature increases has on silver release fraction for selected compacts.

In addition, Table 8 shows the repartition of the temperature adjustments by capsule. It shows the higher adjustments were needed for capsules that were at a lower TAVA temperature (Capsules 12, 10, 3, and 1). Conversely, capsules at higher TAVA temperatures did not need large temperature adjustments to match the PIE release fraction. Previous comparisons to PIE data also show that PARFUME underpredicts the silver release fraction in UCO fuel and in some cases, large temperature adjustments are needed to match PIE [4] [5].

Table 8. Temperature adjustment by capsule.

| Capsule | No Change | Temperature Adjustment | | | | Total |
		+50°C	+100°C	+150°C	+200°C	
12	-	-	-	-	4	*4*
10	-	-	-	1	3	*4*
8	-	-	1	3	-	*4*
7	2	2	-	-	-	*4*
5	-	-	2	-	2	*4*
4	-	-	-	2	2	*4*
3	-	-	-	-	4	*4*
1	-	-	-	-	4	*4*
Total	*2*	*2*	*3*	*6*	*19*	*32*

4.2.2   Release Versus Source

The release of silver is primarily driven by temperature and there is some uncertainty in predicting silver release because of the temperature spatial distribution across the compacts. The silver source is also spatially distributed across the compact, but both the PARFUME calculations and release fractions calculated from the PIE measurements consider a uniform source averaged over the compact volume to normalize the amount of released silver. In reality, the silver source is directly linked to the distribution of neutron flux and fission density within a compact. The neutron flux was not uniform throughout the capsules, as there are both axial and azimuthal variations. Consequently, a gradient in fission density rate existed throughout the capsules and within each individual compact, as demonstrated in the AGR-1 experimental results versus PARFUME [4]. The results show that a variation in the relative amounts of U-235 and Pu-239 in the compacts, and therefore the subsequent Ag-109 production and activation to Ag-110m were not uniform throughout the compacts, leading to a distribution of the Ag-110m source across compacts.

It is too computationally time-consuming to predict the FP source of each individual fuel particle per compact; therefore, both PARFUME and as-run neutronics calculations used average sources. In PARFUME, the source is at the particle level, and it is obtained by calculating the source of an average particle bearing the average burnup of the compact. The silver fission yield used in this calculation is a burnup-dependent correlation obtained from a coupled calculation between MCNP [31] and ORIGEN2 [32] that takes into account the production of Ag-109 from uranium and plutonium fission and the subsequent activation to Ag-110m. The as-run neutronics calculation of the source is done directly at the compact level. The two sources are related by the number of particles in the compact. Previous calculations for the AGR-1 experiment [4] showed that the relative magnitude of the source has no impact when calculating the release fractions because of the very definition of the release fraction that normalizes the release to the source term.

The first consequence of using average sources is that these calculated average sources are not equal to the real silver produced during irradiation. Silver production is higher from fission in Pu-239 than from U-235. Early in the irradiation, nearly all fissions are from U-235. As the irradiation progresses, U-238 is transmuted to Pu-239, and fissions in Pu-239 become more frequent. Because the effective FP yield of silver is not independent of burnup, the silver source exhibits a nonlinear build-up with time. This non-linearity implies the source obtained at the average compact burnup (calculated sources) is not equal to the average source obtained from all the sources of the individual particles, each at their own burnup (real source). Appendix D of the AGR-1 experiment versus PARFUME report [4] offers a detailed theoretical explanation as to why the two calculated sources do not represent the real source, and therefore only allow estimates of the real fractional release of the irradiated compacts. Furthermore, even though PIE and PARFUME use a similar source to normalize their respective measured or calculated release, results cannot provide comparable silver release fractions independently of the temperature issue. This is again due to the non-linearity of the silver generation rate with burnup.

PARFUME calculates the fractional release of silver independently of its isotopes. This is because the effective FP yield used for silver does not discriminate its isotopes but was calculated to reflect the overall production of silver with burnup. In the case of PIE, the release of isotope Ag-110m is measured, and its production by activation of isotope Ag-109 is shifted in time. The release fraction of Ag-110m is the same as the release fraction of Ag-109 if it is assumed that both isotopes are similarly distributed across the compacts, and that both isotopes behave similarly regarding diffusion through the TRISO particles and matrix. The second assumption seems reasonable, but it cannot be confirmed by any currently available experimental data or backed-up by any theoretical diffusion model. It also cannot be modeled by PARFUME since the code does not differentiate between isotopes. That assumption also entails that the variation in time of the Ag-110m/Ag-109 ratio has no impact on their respective release fractions; both released fractions are equal because of the similar diffusion behavior of the two isotopes, and because the relative magnitude of the source does not modify the subsequent release fraction.

The first assumption, on the other hand, is dubious at best since the neutron flux is not spatially uniform across a given compact, resulting in nonuniform distributions of Ag-109 and Ag-110m across that compact, as explained previously. Because Ag-110m is produced by the activation of Ag-109, the effect of a nonuniform neutron flux on the Ag-110m distribution is amplified. Since particles are not individually modeled by as-run neutronics or by PARFUME, these nonuniformities of the Ag-109 and Ag-110m distributions are not captured by calculation. Therefore, their impact on the measured and calculated release fractions of silver cannot be properly assessed.

5.   FISSION PRODUCT DIFFUSION THROUGH CAPSULE RINGS

5.1   Model Description and Implementation

Each AGR-3/4 compact contains driver fuel particles and 20 DTF particles placed along its axis. The fuel compacts are surrounded by three concentric annular rings of test material consisting of fuel-compact matrix material and fuel-element graphite. Figure 20 shows a BISON 3-D model, with the 20 DTF particles placed in the center line and randomly distributed driver particles hosted in the fuel compact. The four regions of the BISON model are the fuel compact, matrix, graphite, and sink. They are separated blocks without sharing nodes between their interfaces. The height is 12.5 mm with a compact radius of 6.15 mm and ring wall thicknesses of 6.05, 6.30, and 13.14 mm, respectively. All fuel particles are randomly generated from a Monte Carlo simulation. At every time step, the FP and heat released from each particle is transferred to the compact as a point source. Those point sources are used in the compact model to drive the FP and thermal diffusion.
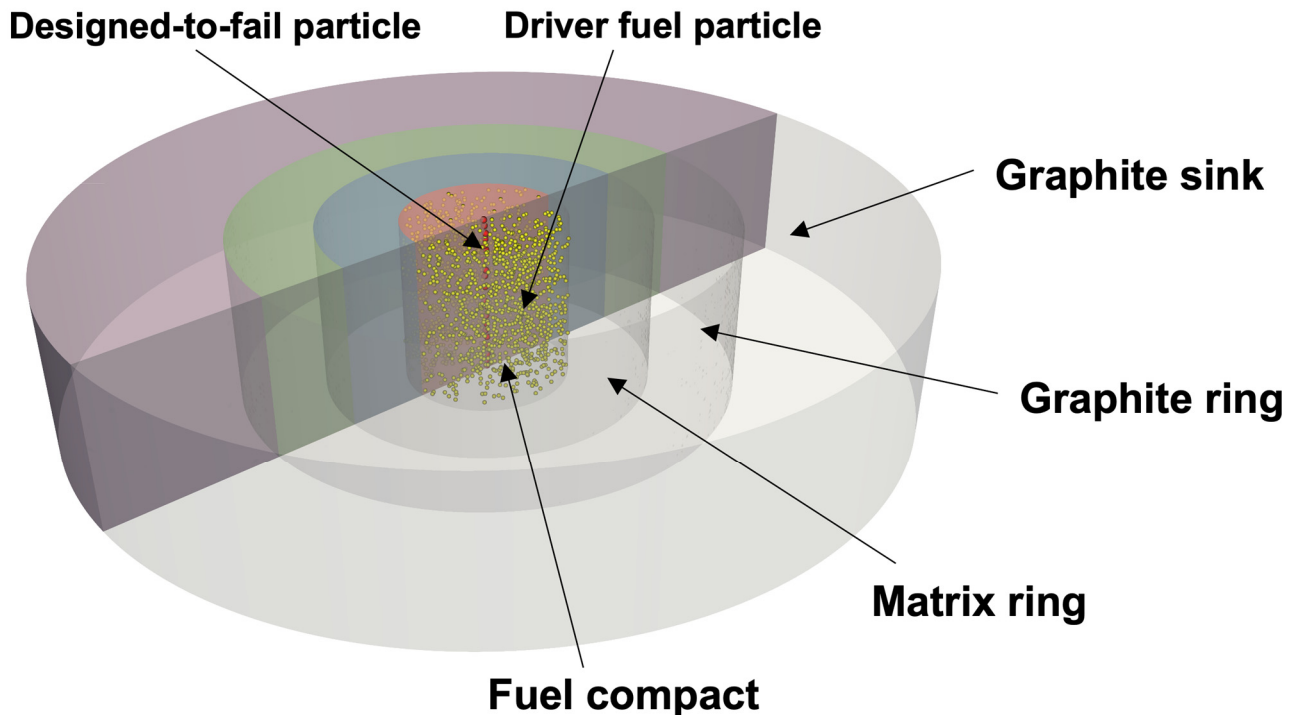
Figure 20. AGR-3/4 BISON representation. The four regions of the BISON model are fuel compact, matrix ring, graphite ring and graphite sink.

BISON solves the following heat and diffusion coupled equations:

$$\rho c_P \frac{\partial T}{\partial t} = \nabla \cdot (k\nabla T) + E_f \dot{F}$$

$$\frac{\partial C}{\partial t} + \nabla \cdot (D\nabla C) + \lambda C - S = 0$$

where T is temperature, ρ and c_p are density and specific heat, k is the thermal conductivity, E_f is the energy released per fission, $\dot{F}$ is the volumetric fission rate, C is concentration, and λ and S is the radioactive decay constant and source rate of a given species, respectively.

The diffusion coefficient, $D\left(\frac{m^2}{s}\right)$, is defined in Arrhenius form as:

$$D = D_0 \exp(-\frac{Q}{RT})$$

where R is the universal gas constant. Values of D_0 and Q for silver, cesium, and strontium for matrix and graphite are summarized in *Table 9*. The resulting diffusion coefficients as a function of temperature for the selected FPs are illustrated in *Figure 21* for both matrix and graphite materials.

Table 9. Diffusion coefficient for matrix and graphite.

	Silver		Cesium		Strontium	
Species	D_0 (m²/s)	Q (J/mol)	D_0 (m²/s)	Q (J/mol)	D_0 (m²/s)	Q (J/mol)
Matrix	1.6	258000	3.60×10^{-4}	189000	1.00×10^{-2}	303000
Graphite	1.38×10^{-2}	226000	1.70×10^{-6}	149000	1.70×10^{-2}	268000
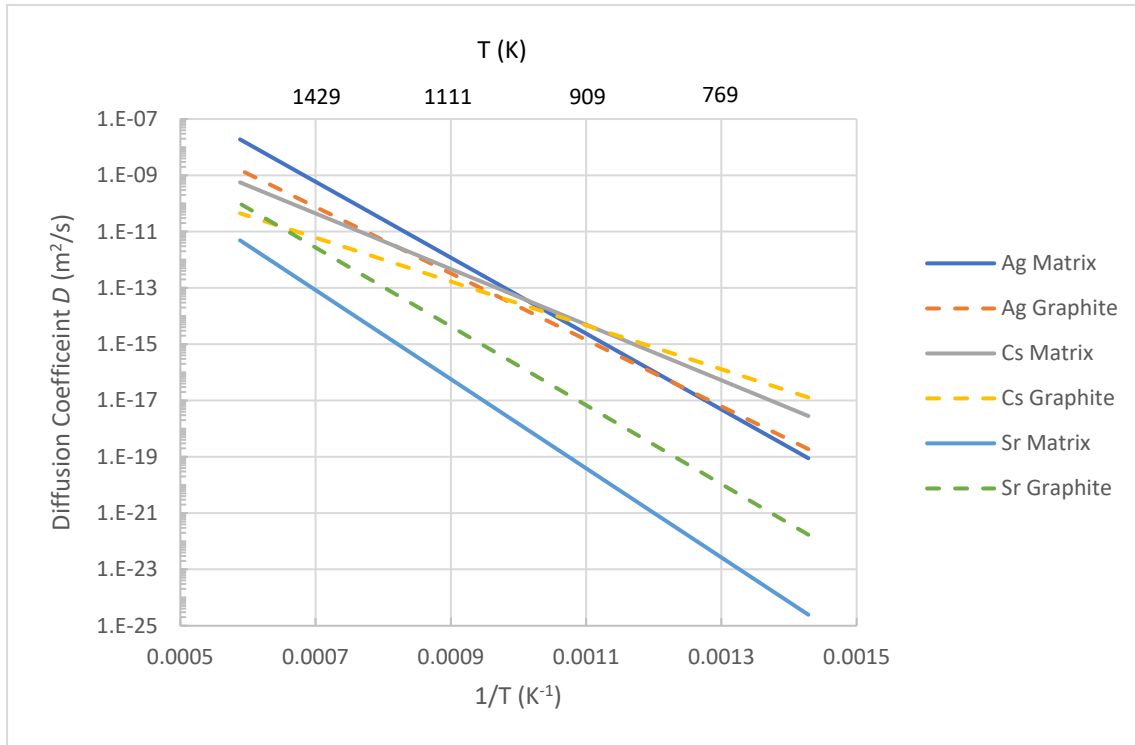
Figure 21. Diffusion coefficients as a function of temperature.

The temperature boundary conditions at the outer fuel compact surface, inner/outer matrix surface, inner/outer graphite surface and inner/outer sink surface are obtained from a prior Abaqus analysis [33]. The presence of gaps results in discontinuities in the FP concentration across rings. Established sorption isotherms are used to determine the surface concentration between the two surfaces (subscripts 1 and 2) by:

$$\exp\left(A_1 + \frac{B_1}{T_1}\right) C_1^{\left(D_1 + \frac{E_1}{T_1}\right)} + \exp\left[\left(A_1 + \frac{B_1}{T_1}\right) + \left(D_1 - 1 + \frac{E_1}{T_1}\right)\left(d_{1_1} - d_{2_1}T_1\right)\right] C_1 = \exp\left(A_2 + \frac{B_2}{T_2}\right) C_2^{\left(D_2 + \frac{E_2}{T_2}\right)} + \exp\left[\left(A_2 + \frac{B_2}{T_2}\right) + \left(D_2 - 1 + \frac{E_2}{T_2}\right)\left(d_{1_2} - d_{2_2}T_2\right)\right] C_2$$

The values A, B, D, E, d_1, and d_2 are sorption isotherm constants and their values for cesium and strontium are provided in Table 10. Since there is a lack of experimental data for silver, the cesium isotherm values are used in this analysis for the silver model.

Table 10. Sorption isotherm constants.

Material	Fission Product	A (-)	B (K)	D (-)	E (K)	d_1 (-)	d_2 (1/K)
Matrix	Cs	19.3	-47300	1.51	4340	3.4	6.15×10^{-4}
	Sr	54.3	-149000	-8.52	28500	3.13	0
Graphite	Cs	24.0	-35700	-1.56	6120	2.04	1.79×10^{-3}
	Sr	19.4	-40100	-0.32	4090	-2.12	0

The interfacial conditions are completed by a second boundary condition to ensure the mass flux balance across the gap:

$$D_{0_1} \exp\left(-\frac{Q_1}{RT_1}\right) \nabla C_1 \cdot n_1 = D_{0_2} \exp\left(-\frac{Q_2}{RT_2}\right) \nabla C_2 \cdot n_2$$

The interfacial conditions are enforced by a penalty method and implemented in BISON as a *InterfaceKernel* object.

5.2   COMSOL Benchmark

For verification purpose, BISON's simulation results are compared against the previous COMSOL simulation results for the AGR-3/4 experiment [34]. Due to lack of the COMSOL modeling data, some of the input parameters used in BISON were extracted from the COMSOL output. The temperature boundary conditions used in the benchmark are listed in Table 11. For this example, the inner ring was made of a matrix material.

Table 11. Temperature boundary conditions.

Compact	Matrix		Graphite		Sink	
Outer Temp (K)	Inner Temp (K)	Outer Temp (K)	Inner Temp (K)	Outer Temp (K)	Inner Temp (K)	Outer Temp (K)
1504	1432	1314	1290	1246	1235	855

The temperature profiles calculated by the two codes are shown in Figure 22. The BISON model shows good agreement with the COMSOL solution in the matrix, graphite, and sink rings. The discrepancy inside the compact is explained due to the two codes using a different heat source input. The BISON model calculated the heat source from its own particle simulation whereas COMSOL used the input from a previous PARFUME calculation. Since the PARFUME data is not readily accessible, the discrepancy between the temperature profiles within the compact cannot be further investigated.

The Cs concentration profile is shown in Figure 23. The Cs inside the matrix and graphite rings seems to diffuse faster in the BISON simulation than the COMSOL simulation. The BISON model uses the diffusion coefficients from Table 9. The COMSOL results were reported to use the same diffusion coefficients, but the actual values used by this COMSOL simulation is unknown due to the lack of the original data file. It is found that the use of the slightly modified diffusivity in BISON could improve the agreement. More importantly, the concentration variation across the "gaps" seem to match very well between BISON and COMSOL which verifies the BISON implementation of the interfacial isotherm sorption conditions.
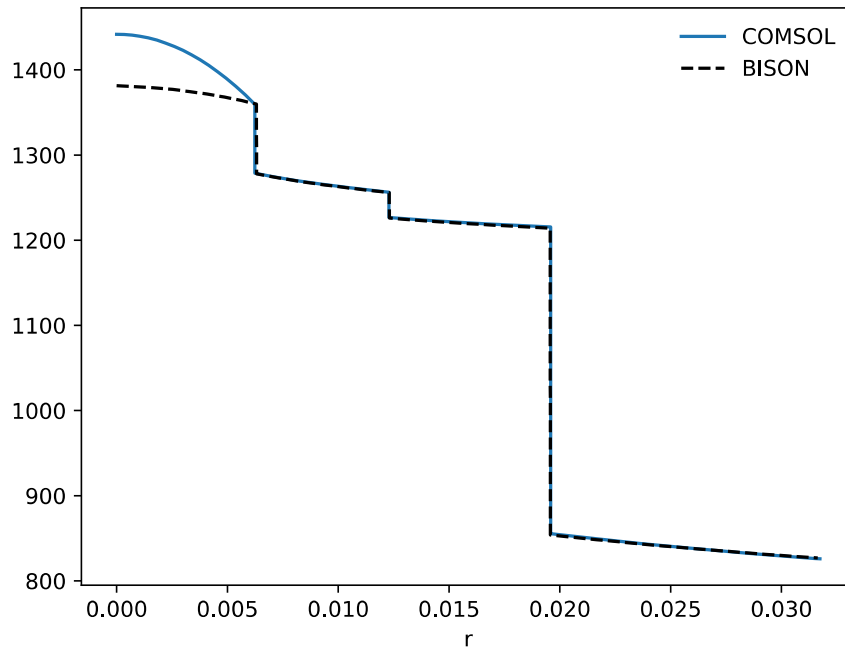

Figure 22. Radius *r* (m) temperature (K) profile of the COMSOL benchmark with comparison to BISON.
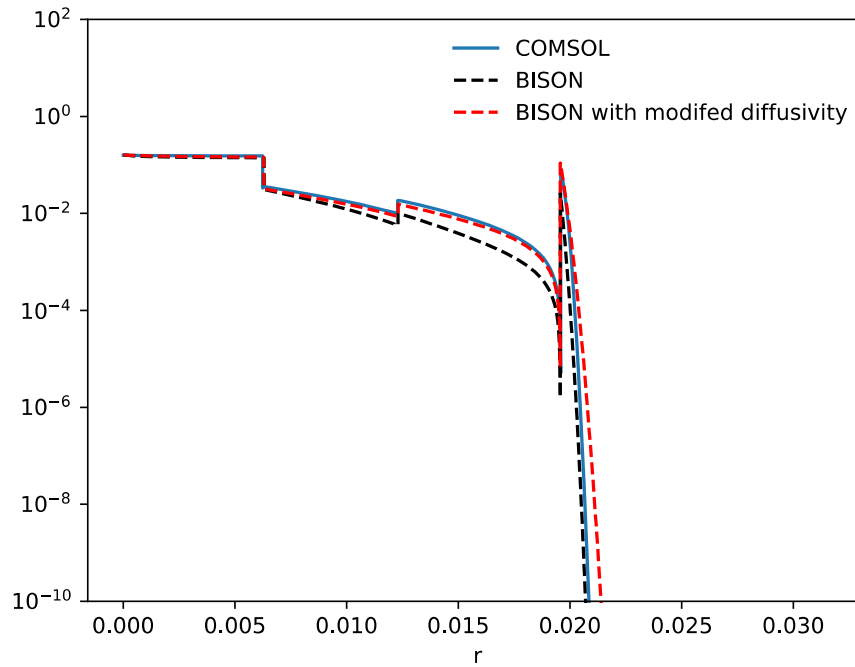
Figure 23. Radius r (m) Cs concentration (mol/m^3) profile of the COMSOL benchmark with comparison to BISON.

5.3   Modeling Input

Literature regarding AGR-3/4 experiment has referred to the concentric rings by various names: matrix or inner ring, graphite ring or outer ring. To avoid confusion since the first ring can comprised by both matrix and graphite material in the AGR-3/4 experiment, the first concentric ring surrounding the compact will be referred to as the inner ring when presented herein. Similarly, the second concentric ring between the inner ring and sink ring will be referred to herein as the outer ring. The concentric ring outside of the outer ring will be referred to as the sink ring.

5.3.1   AGR-3/4 Capsule Components

AGR-3/4 consisted of two types of capsules: "standard" (Std) and "fuel body" (FB) [35]. The standard type (Capsules 1, 3, 5, 7, 8, 10, and 12) outer ring (OR) is open on its top and bottom whereas the FB type (Capsules 2, 4, 6, 9, and 11) had a floor and a lid holding the fuel, inner ring (IR), and graphite ring as a single piece to allow for removal and further heat-up tests for FP migration analysis. The rings of both capsule types were either comprised of graphitic matrix material or structural graphite (IG-110 or PCEA). Toyo Tanso IG-110 is an isotopic graphite with fine grains while GrafTech PCEA is extruded graphite [35]. The capsule types used in the AGR-3/4 experiment along with the corresponding ring material within each capsule are summarized in Table 12. Only the seven standard type capsules and one FB type (Capsule 4) were considered in this analysis. The remaining capsules will be subjected to further post-irradiation heating tests.

Table 12. AGR-3/4 capsule types and ring materials.

Capsule	Type	Ring Material		
		Inner	Outer	Sink
1	Std	Matrix	PCEA	PCEA
2	FB	Matrix	PCEA	PCEA
3	Std	PCEA	PCEA	PCEA
4	FB	Matrix	PCEA	PCEA
5	Std	Matrix	PCEA	PCEA
6	FB	Matrix	PCEA	PCEA
7	Std	Matrix	PCEA	PCEA
8	Std	IG-110	IG-110	PCEA
9	FB	Matrix	IG-110	PCEA
10	Std	PCEA	PCEA	PCEA
11	FB	Matrix	PCEA	PCEA
12	Std	Matrix	PCEA	PCEA

5.3.2 Source Term

BISON used the as-run neutronics and thermal analysis to obtain the FP source term from both the driver fuel and DTF particles. The release fraction from the particles into the compact matrix for the FPs of interest are summarized in Table 13. The DTF particles were intended to be the primary source of FP release, but as Table 13 indicates, the driver fuel particle release is not negligible, especially in the case for silver release. The source term from driver fuel particles is amplified by the fact that there is a factor of approximately 100 more driver particles than DTF particles assumed in this study. The silver, cesium, and strontium source term on a per particle basis is summarized in Figure 24 - Figure 26. Appendix C contains the time evolution of the source term release for each capsule.

Table 13. FP release fraction from both driver and DTF fuel.

Capsule	Ag		Cs		Sr	
	Driver	DTF	Driver	DTF	Driver	DTF
1	0.02%	89.36%	0.00%	22.10%	0.00%	2.77%
3	23.25%	98.54%	0.00%	92.76%	0.85%	2.90%
4	3.15%	96.97%	0.00%	68.89%	0.13%	2.78%
5	4.05%	96.61%	0.00%	71.60%	0.17%	2.78%
7	64.12%	99.39%	0.20%	98.07%	4.74%	5.58%
8	3.15%	96.90%	0.00%	68.93%	0.13%	2.78%
10	32.52%	98.84%	0.01%	94.61%	1.17%	3.05%
12	0.00%	65.83%	0.00%	3.28%	0.00%	2.76%
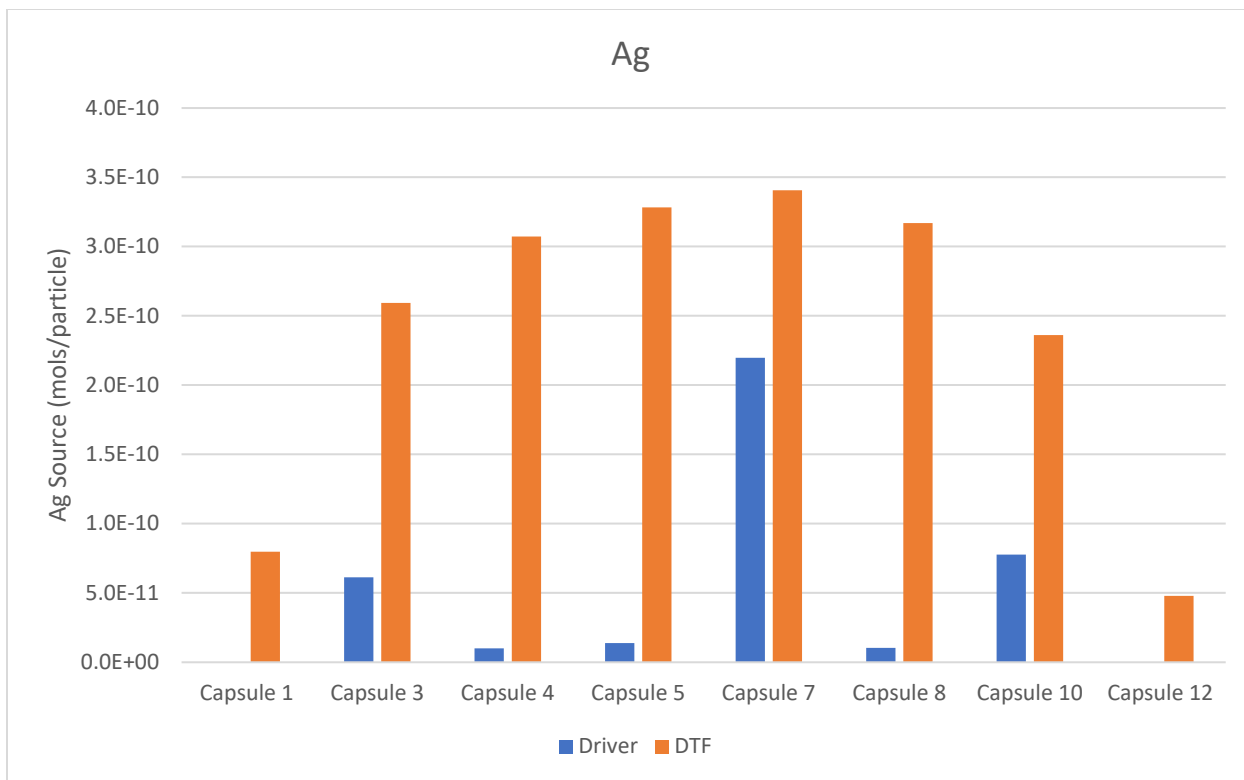
Figure 24. Silver source term per particle.
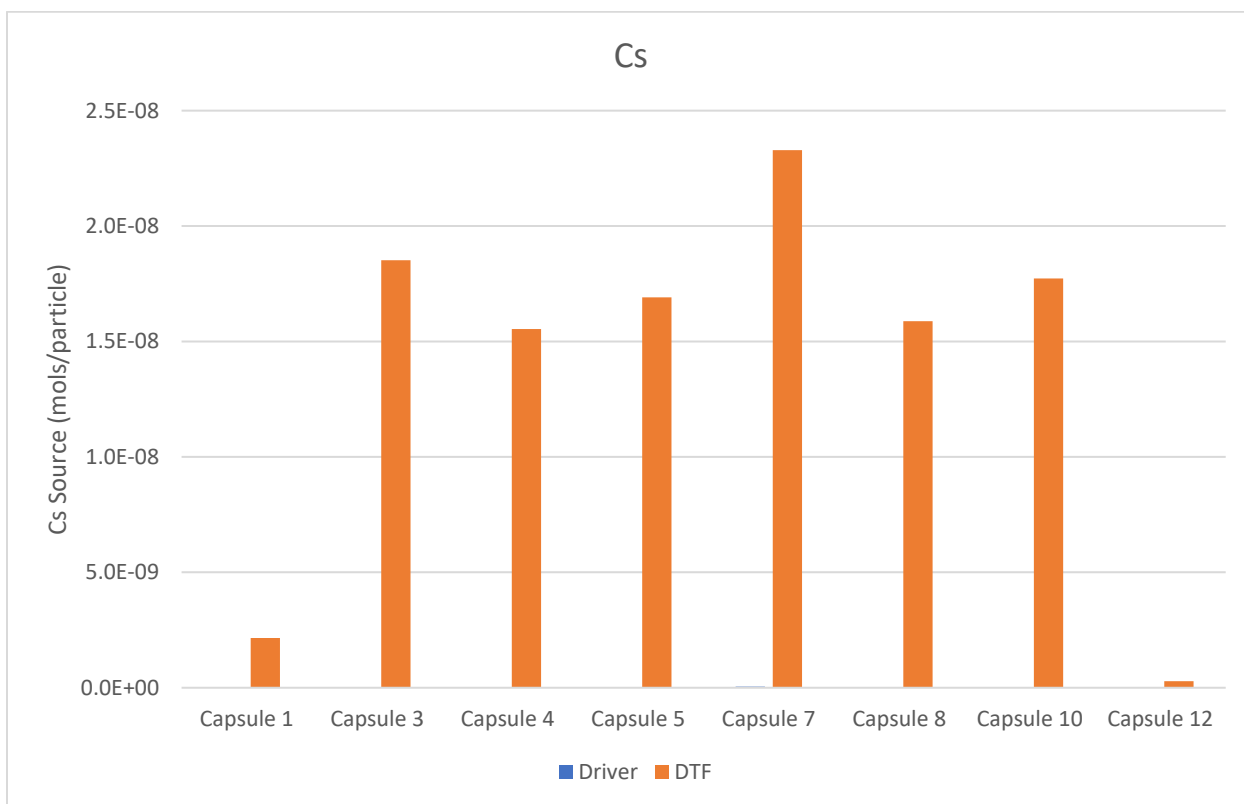
Figure 25. Cesium source term per particle.
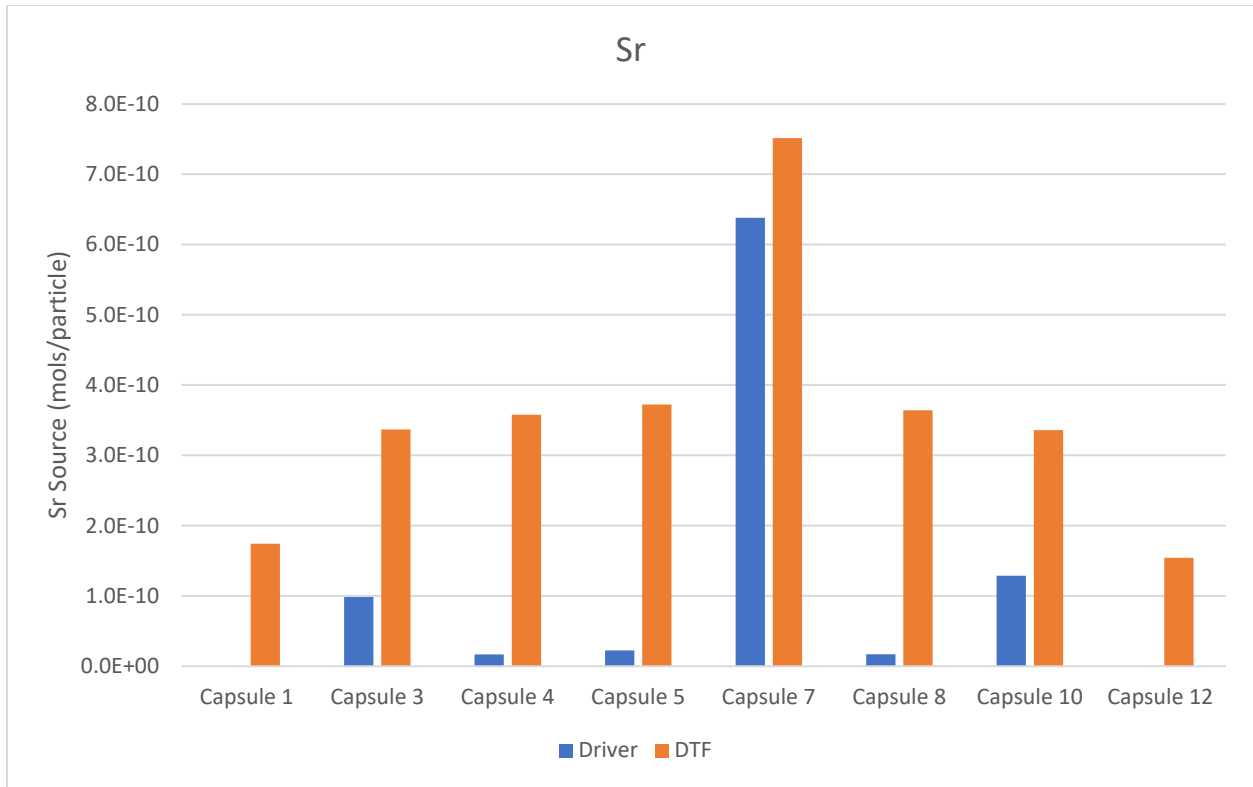
Figure 26. Strontium source term per particle.

5.3.3 Thermal Analysis

The model developed to benchmark BISON against the COMSOL simulation was modified to reflect the as-run irradiation conditions of the AGR-3/4 experiment. Specifically, this required the as-run temperature profile across the four BISON defined regions to capture the inner and outer temperatures of the compact/IR/OR/sink ring. These temperatures were obtained from the AGR-3/4 Daily As-Run Thermal Analysis [23] and their end of irradiation TAVA temperatures are summarized in Table 14. The TAVA daily temperature time evolution during irradiation for the compacts and capsule rings are illustrated in Appendix D.

Table 14. TAVA as-run inner and outer ring temperatures.

Capsule	TAVA (°C)	Compact Outer Temp. (°C)	Matrix Inner Temp. (°C)	Matrix Outer Temp. (°C)	Graphite Inner Temp. (°C)	Graphite Outer Temp. (°C)	Sink Inner Temp. (°C)	Sink Outer Temp. (°C)
12	854	849	795	771	737	731	496	486
10	1191	1159	1039	1016	975	957	665	635
8	1190	1123	1012	976	917	885	596	538
7	1345	1263	1185	1105	1028	1005	643	599
5	1015	1000	888	794	747	719	572	525
4	1008	990	901	814	771	746	609	571
3	1177	1139	1028	1004	963	952	550	519
1	927	928	874	848	757	752	511	501

5.3.4 Capsule Rings Dimensions

In addition, post-irradiation ring measurements were performed, and these dimensions were used in tracking FP migration [35]. These ring dimensions are summarized in Table 15. The BISON model developed for this analysis does not take into account the gaps between the rings; therefore, the gaps were ignored while the total thickness of the rings were conserved. Using these dimensions, the end of irradiation temperature profiles as calculated by BISON across the capsules are illustrated in Figure 27.

Table 15. AGR-3/4 ring dimensions from PIE.

Capsule	Matrix IR (mm)	Matrix OR (mm)	Graphite IR (mm)	Graphite OR (mm)	Sink IR (mm)	Sink OR (mm)
12	6.235	12.115	12.255	17.490	19.670	30.800
10	6.290	12.020	12.415	18.740	19.700	31.715
8	6.300	12.035	12.385	19.275	19.785	31.820
7	6.375	11.835	12.465	18.675	19.765	31.815
5	6.335	11.945	12.340	19.695	19.770	31.805
4	6.355	11.935	12.350	19.620	19.740	31.660
3	6.310	12.015	12.430	16.540	20.710	31.780
1	6.275	11.805	12.265	16.750	20.605	30.795
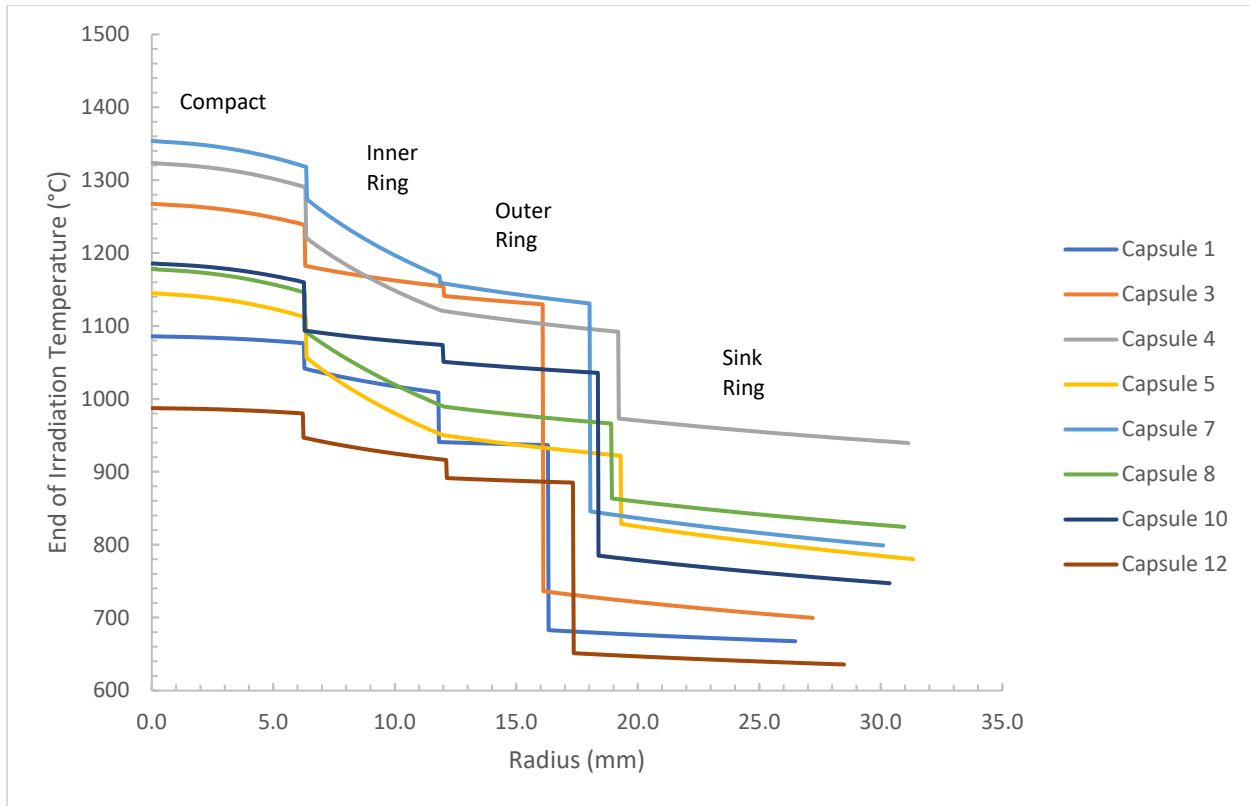
Figure 27. End of irradiation capsule temperature profiles calculated by BISON.

5.4   Fission Product Concentration Profiles

Using the input data from Section 5.3 and newly developed BISON sorption isotherm model, the FP transport concentration profiles across the four regions or "blocks" for each capsule were calculated. BISON calculates the FP release of all isotopes for a given element and does not distinguish between the source of individual isotopes. The BISON predicted silver concentration profile is illustrated in Figure 28. The concentration profiles show the four distinct regions modeled by BISON and the silver concentration eventually goes to zero in the sink ring. The cesium and strontium concentration profiles are shown in Figure 29 and Figure 30, respectively.

Figure 28. Silver concentration profiles as calculated by BISON.

Figure 29. Cesium concentration profiles as calculated by BISON.
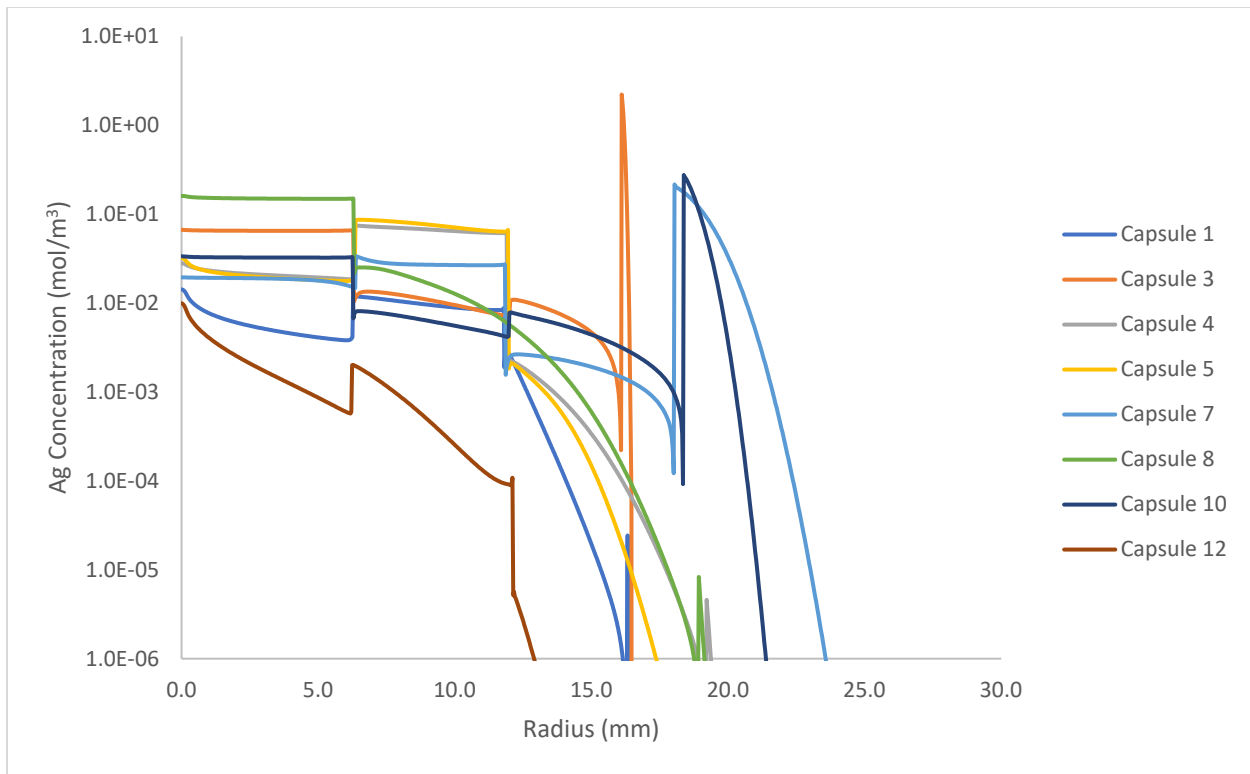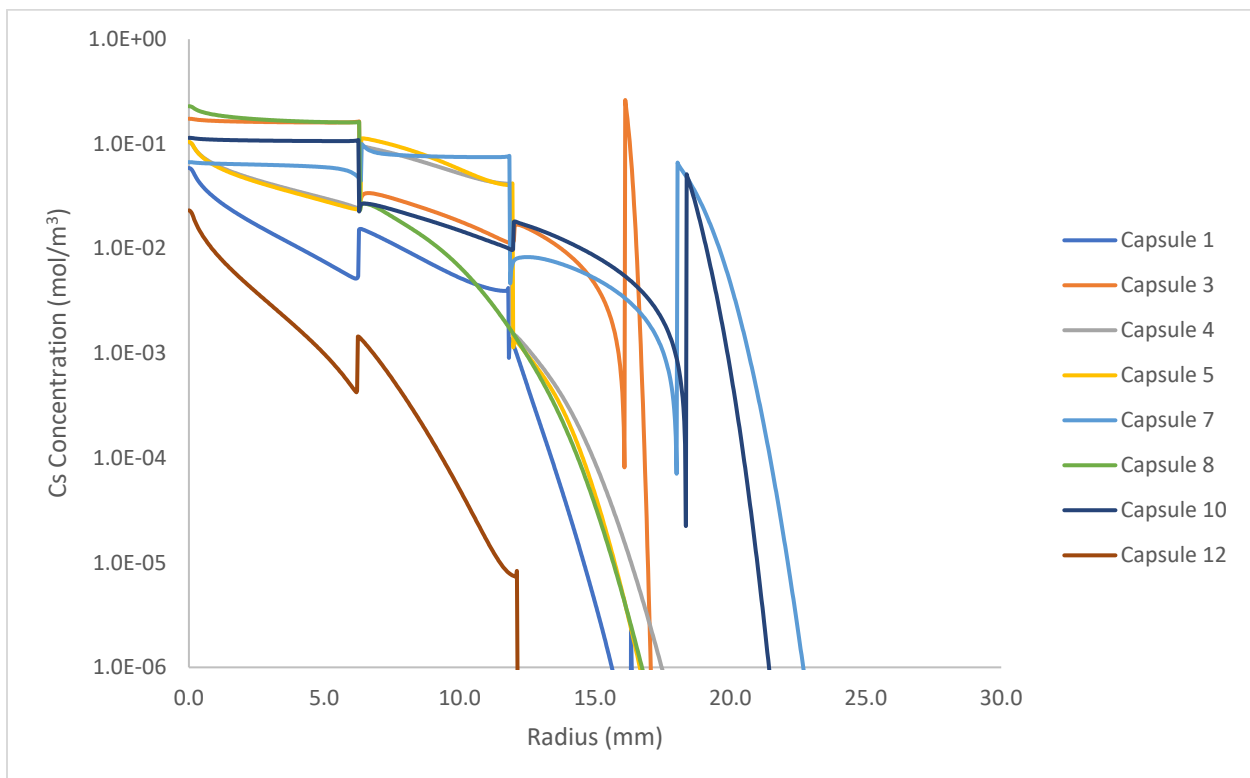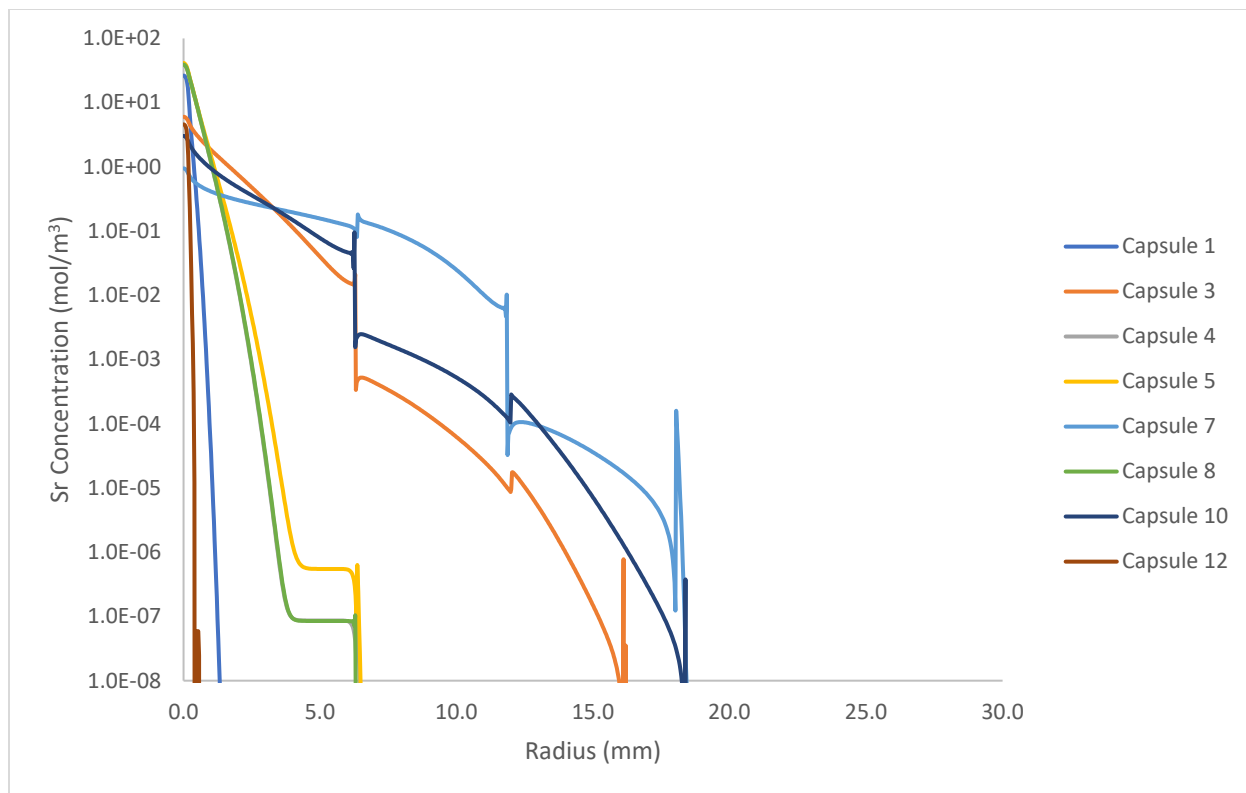
Figure 30. Strontium concentration profiles as calculated by BISON.

5.5   Comparison to PIE Data

FP concentration profiles were measured for the AGR-3/4 experiment [35] and the PIE data was used to compare to predicted BISON results. Since BISON does not distinguish between individual isotopes of a particular FP element, the measured data had to be adjusted using the calculated decay corrected mass fraction of that isotope from the as-run neutronics calculations. This was accomplished by averaging the middle two compacts calculated isotopes concentration and dividing it by the total concentration of that element. These correction factors are summarized in Table 16.

In addition, the measured data presented in Reference [35] are in units of activity and needed to be converted to mass (mols) of the isotope of interest (Ag-110m, Cs-134, Cs-137, and Sr-90) using their respective decay constants. Further, since BISON does not model gaps between the concentric rings, the radial BISON results had to be shifted to match the measured gaps that were obtained from Reference [35]. The BISON predictions and measured data were then plotted against each other, where PIE data existed. In some cases, PIE data was not available (Capsule 1 and Capsule 4). In other cases, particularly with Sr-90, the calculated concentration by BISON was significantly lower than the measured values and therefore are not included in this report (Capsule 12). As an example, Capsule 7's measured versus predicted silver concentration profile through the IR and OR is presented in Figure 31. The measured versus predicted concentration profiles for cesium and strontium can be found in Figure 32 and Figure 33, respectively. The remaining concentration profiles for the remaining compacts are presented in Appendix E, along with the measured PIE data used in this analysis.

Table 16. Adjustment factors based on isotope fractions of the middle two compacts.

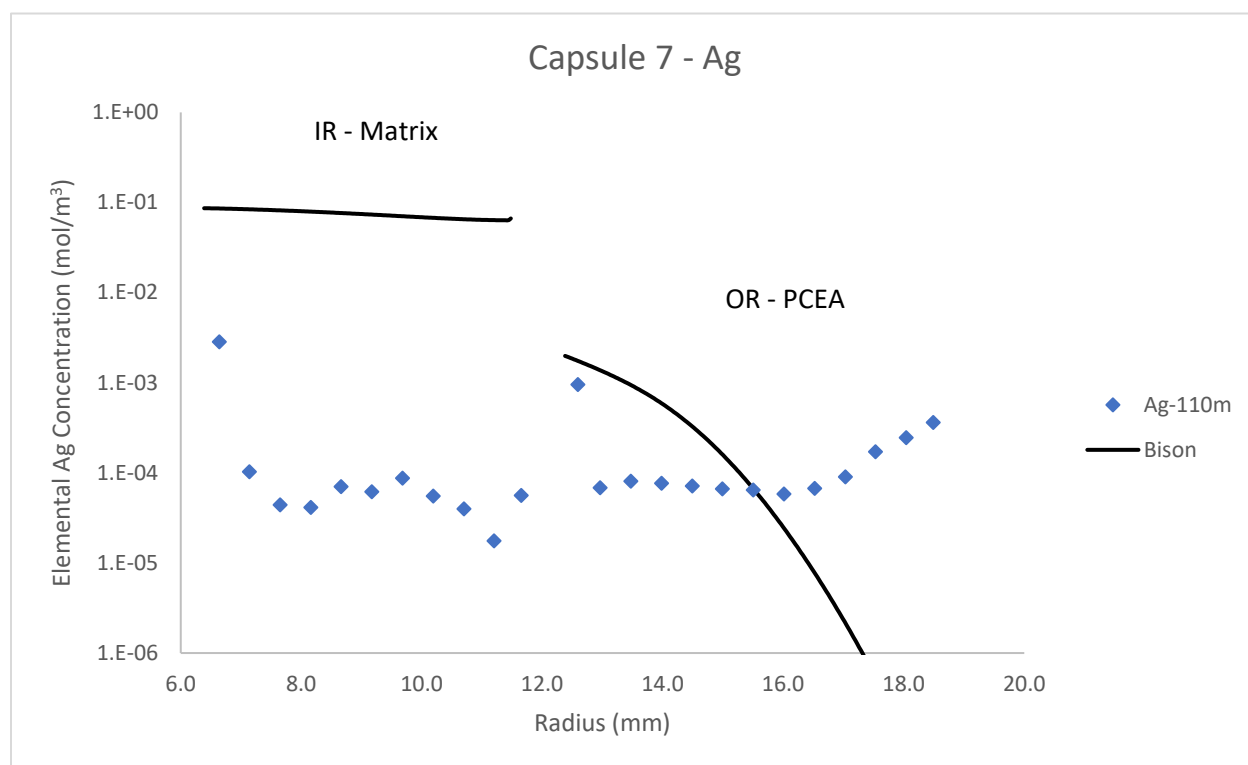| Capsule	Ag-110m Ag	Cs-134 Cs	Cs-137 Cs	Sr-90 Sr
1	0.00281	0.01362	0.41321	0.56574
3	0.00653	0.03339	0.44266	0.57015
4	0.00760	0.03904	0.44740	0.57147
5	0.00811	0.04144	0.44905	0.57185
7	0.00824	0.04164	0.44949	0.57200
8	0.00788	0.03968	0.44828	0.57166
10	0.00598	0.03020	0.43960	0.56947
12	0.00228	0.01077	0.40581	0.56514

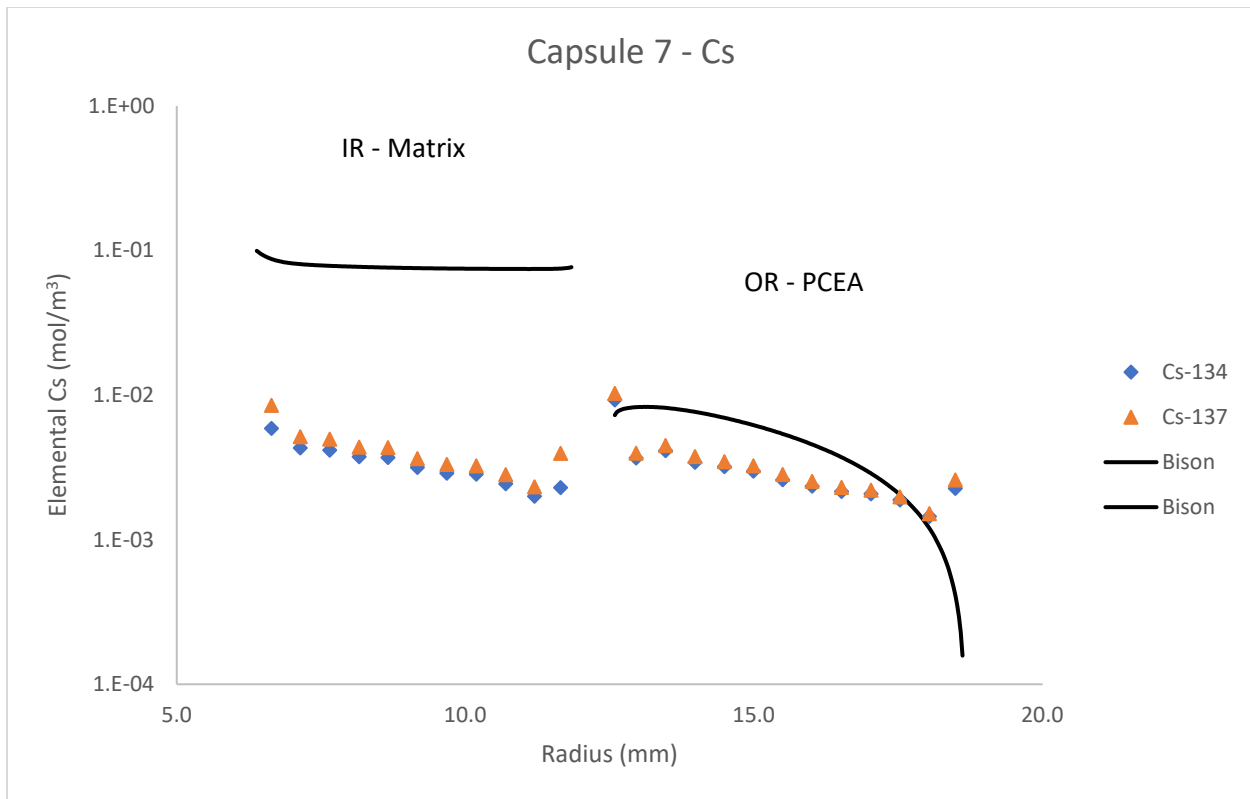Figure 31. Capsule 7 silver measured versus calculated concentration profile.

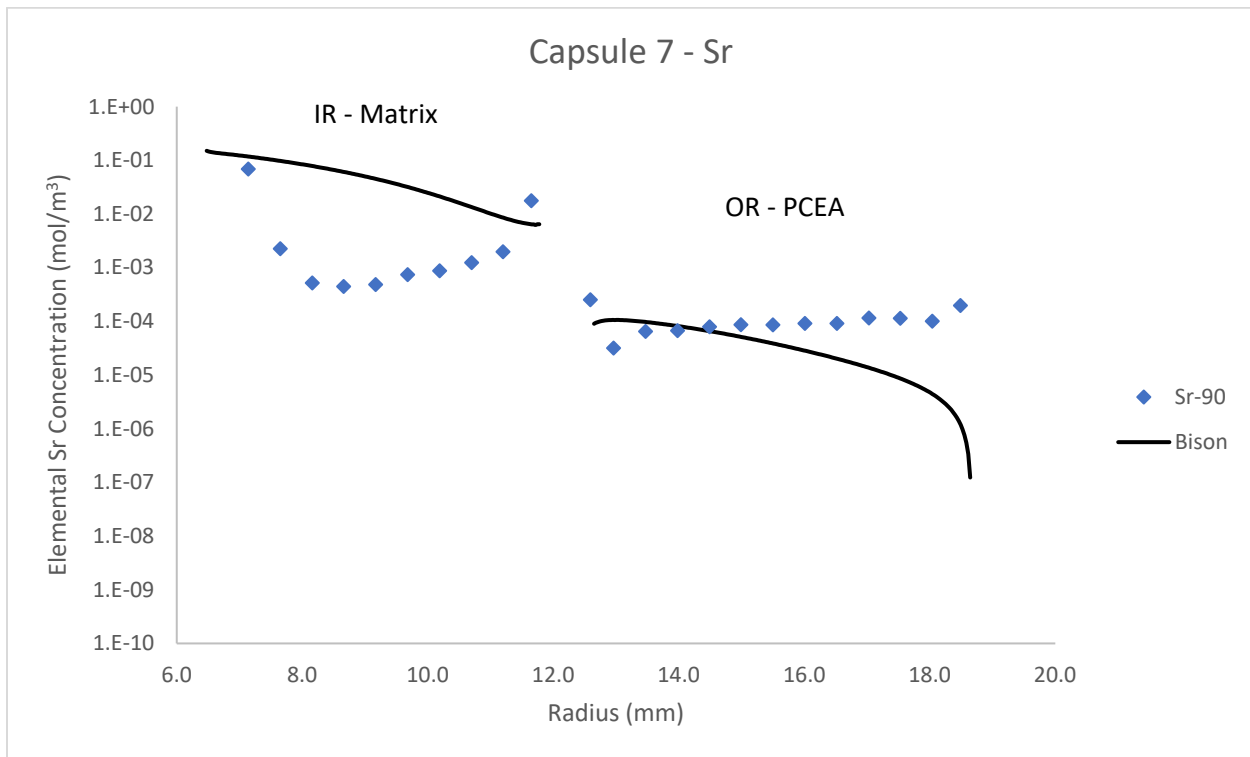Figure 32. Capsule 7 cesium measured versus calculated concentration profile.

Figure 33. Capsule 7 strontium measured versus calculated concentration profile.

5.6   Discussion of Diffusion Across Capsule Rings

In general, the FP diffusion profiles calculated by BISON showed relatively the same trend in concentration in the IR although the calculated values differed from the measured values by more than an order of magnitude in most cases. In the OR, the concentration profiles calculated by BISON were not in as good as agreement but showed somewhat the same trend though the ring. This could be attributed to several factors.

First, BISON uses the sorption isotherm parameters for graphite previously calculated to model the gaps, which may lead to the biases between the measured and calculated values. The uncertainty surrounding the sorption isotherm values are also unclear, which could result in additional discrepancies between the two. This could potentially explain why the OR's concentration profile were not in as good of agreement for the IR.

Secondly, the BISON uses the TAVA temperatures across the capsule's components, which could vary significantly between the top and bottom of the capsule. For example, Compacts 1 and 4 within given capsules generally experience a lower TAVA temperature than the middle Compacts, 2 and 3. This trend continues throughout the capsule's rings out to the sink. The contribution of the lower temperatures to the overall capsule TAVA temperature would have a significant impact on the overall diffusion profile across the capsule.

Finally, the measured values presented in this report were obtained from the PIE data obtained from sampling of the rings at the vertical center. In reality, the concentrations would vary axially across the rings due to differences in compact burnups and temperatures. Combined, these factors could significantly impact the predicted concentrations beyond the IR out to the sink ring.

Also, there was an elevated FP concentration on the inner and outer surfaces of the rings that was not predicted by the model. This has been theorized as being a result of a "short circuit" diffusion where the concentrations are elevated due to the gas between the gaps of the rings. This was particularly noted when the ring "nubs" used for handling were measured as part of the capsule mass balance. This "short circuit" diffusion path around the rings is not captured by the model implemented in BISON.

In general, the predicted FP concentration by BISON is essentially non-existent in the sink ring for all FP isotopes of interest for this analysis. Based on the mass balance concentrations from PIE, this is not the case and the sink ring contains a measurable amount of FPs. The concentration profiles calculated by BISON can be significantly impacted by the factors discussed above causing a cascading effect in predicting the amount of FPs in the OR and sink ring explaining the discrepancies.

6.   CONCLUSION

PARFUME and BISON were used to predict the silver release from TRISO-coated fuel particles and compacts during the AGR-3/4 experiment using the as-run irradiation conditions. The predicted silver release by these two codes was then compared to the measured values from compact gamma scanning during PIE. The compact release fractions were performed on a compact-level basis and the comparison to PIE values varied depending on the compact TAVA temperature history. Based on the analyses performed, it can be concluded that:

- The PARFUME and BISON calculated silver release fractions were in good agreement. The predicted BISON release fractions were slightly lower than the predicted values by PARFUME but the difference was negligible.

- Both PARFUME and BISON under-predicted the silver release at the compact level regardless of temperature. Capsule 7, the hottest capsule, showed the best agreement between the predicted and measured data.

- The uncertainties associate with the low temperature capsules (1 and 12) result in a release fraction that could vary as much as 80%; therefore, this data should be used with caution in formulating any conclusion regarding FP diffusion of silver at low temperatures.

- There is no correlation in the under-prediction of the calculated silver release and compact burnup levels.

- The under-predicted silver release is consistent with previous analyses from AGR-1 and AGR-2.

Additionally, BISON was used to model the FP concentration profiles across selected capsules' rings using daily as-run irradiation conditions and compared to measured PIE data. This required implementing a sorption isotherm model to capture FP diffusion across the gaps that were present between the IR and OR and OR and sink ring. To verify the model, BISON was compared to a previous COMSOL simulation using AGR-3/4 data.

Once the BISON model was verified, it was used to calculate the concentration profiles for silver, cesium, and strontium across the inner and outer rings. From these calculations, the following observations were made:

- The BISON calculated FP concentration profiles in the IR were similar to the measured values in terms of their shape but differed in the relative magnitude.

- The profiles in the OR were not in as good of agreement as the IR for all three FPs. This could be attributed to uncertainties in the sorption isotherm constants, temperature variations across the capsule, and averaging compact burnups across the capsule.

- The inner and outer surfaces of the capsule rings had elevated FP concentrations that were not predicted by BISON. It has been hypothesized that these higher concentrations were a result of "short circuit" FP diffusion between the gaps as FPs wrap around the concentric rings.

- BISON does not predict a substantial measure of FPs in the sink ring contrary to what was observed during PIE.

Using the model developed for these analyses, BISON now has the capability to estimate the FP diffusion coefficients for matrix and graphite materials at the engineering level scale. This will allow for more accurate modeling of FP transport from TRISO-coated fuel particles.

7.   REFERENCES

[1] P. A. Demkowicz, *Technical Program Plan for INL Advanced Reactor Technologies Advanced Gas Reactor Fuel Development and Qualification Program,* PLN-3636, Rev. 10, Idaho National Laboratory, 2021.

[2] G. K. Miller, D. A. Petti, J. T. Maki, D. L. Knudson and W. F. Skerjanc, *PARFUME Theory and Model Basis Report,* INL/EXT-08-14497, Rev. 1, Idaho National Laboratory, 2018.

[3] R. L. Williamson, J. D. Hales, S. R. Novascone, G. Pastore, K. A. Gamble, B. W. Spencer, W. Jiang, S. A. Pitts, A. Casagranda, D. Schwen, A. X. Zabriskie, A. Toptan, R. Gardner, C. Mathews, W. Liu and H. Chen, "BISON: A Flexible Code for Advanced Simulation of the Performance of Multiple Nuclear Fuel Forms," *Nuclear Technology,* vol. 207, no. 7, pp. 954 - 980, 2021.

[4] B. P. Collin, *Comparison of Fission Product Release Predictions using PARFUME with Results from the AGR-1 Irradiation Experiment,* INL/EXT-14-31975, Rev. 0, Idaho National Laboratory, 2014.

[5] W. F. Skerjanc, *Comparison of Fission Product Release Predictions using PARFUME with Results from the AGR-2 Irradiation Experiment,* INL/EXT-20-59448, Rev. 0, Idaho National Laboratory, 2020.

[6] W. J. Kovacs, K. Bongartz and D. T. Goodin, "High-Temperture Gas-Cooled Reactor Fuel Pressure Vessel Peerformance Models," *Nuclear Technology,* vol. 68, pp. 344-354, 1985.

[7] D. G. Martin, "Considerations Pertaining to the Achievement of High Burn-ups in HTR Fuel," *Nuclear Engineering and Design,* vol. 213, pp. 241-258, 2002.

[8] C. J. Permann, D. R. Gaston, D. Andrs, R. W. Carlsen, F. Kong, A. D. Lindsay, J. M. Miller, J. W. Peterson, A. E. Slaughter, R. H. Stogner and R. C. Martineau, "MOOSE: Enabling Massively Parallel Multiphysics Simulation," *SoftwareX,* vol. 11: 100430, 2020.

[9] J. D. Hales, *BISON TRISO Modeling Advancemtns and Validation the AGR-1 Data,* INL/EXT-20-59368, Rev. 0, Idaho National Laboratory, 2021.

[10] J. D. Hales, A. Toptan, W. Jiang and B. W. Spencer, "Numerical Evaluation of AGR-2 Fission Product Release," *Journal of Nuclear Materials,* vol. 558: 153325, 2022.

[11] W. Jiang, J. D. Hales, B. W. Spencer, B. P. Collin, A. E. Slaughter, S. R. Novascone, A. Toptan, K. A. Gamble and R. Gardner, "TRISO Particle Fuel Performance and Failure Analysis with BISON," *Journal of Nuclear Materials,* vol. 548: 152795, 2021.

[12] W. Jiang, G. Singh, J. D. Hales, A. Toptan, B. W. Spencer, S. R. Novascone, S. L. N. Dhulipala and Z. M. Prince, "Efficient High-fidelity TRISO Statistical Failure Analysis using BISON: Applications to AGR-2 Irradiation Testing," *Journal of Nuclear Materials,* vol. 562: 153585, 2022.

[13] C. M. Barnes, *AGR-1 Fuel Product Specification and Characterization Guidance,* EDF-4380, Rev. 8, Idaho National Laboratory, 2006.

[14] C. M. Barnes, *AGR-3 & 4 Fuel Product Specification,* EDF-6638, Rev 1, Idaho National Laboratory, 2006.

[15] D. W. Marshal, *AGR-3/4 DTF Fuel and Capsule Component Material Specifications,* SPC-1214, Rev. 1, Idaho National Laboratory, 2011.

[16] BWXT, *Industrial Fuel Fabrication and Development Lot G73V-20-69303,* Data Certification Package, BWX Technologies, 2006.

[17] J. D. Hunn, *Data Compilation for AGR-3/4 Driver Fuel Coated Particle Composite LEU03-09T,* ORN/TM-2007/019, Oak Ridge National Laboratory, 2007.

[18] J. D. Hunn, *Data Compilation for AGR-3/4 Designed-To-Fail (DTF) Fuel Particle Batch LEU03-07DTF,* ORNL/TM-2011/109, Oak Ridge National Laboratory, 2011.

[19] B. P. Collin, *AGR-3/4 Irradiation Test Final As-Run Report,* INL/EXT-15-35550, Rev. 1, Idaho National Laboratory, 2016.

[20] J. T. Maki, *AGR-3/4 Irradiation Test Specification,* SPC-1345, Idaho National Laboratory, 2011.

[21] P. A. Demkowicz, *AGR-3/4 Phase 2 Post-Irradiation Examination Plan,* PLN-5382, Rev. 0, Idaho National Laboratory, 2017.

[22] J. W. Sterbentz, *JMOCUP As-Run Daily Physics Depletion Calculation for the AGR-3/4 TRISO Particle Experiment in ATR Northeast Flux Trap,* ECAR-2753, Rev. 1, Idaho National Laboratory, 2015.

[23] G. L. Hawkes, *AGR-3/4 Daily As-Run Thermal Analyses,* ECAR-2807, Rev. 1, Idaho National Laboratory, 2016.

[24] *NP-MHTGR Material Models of Pyrocarbon and Pyrolytic Silicon Carbide,* CEGA-002820, Rev. 1, CEGA Corporation, 1993.

[25] IAEA, *Fuel Performance and Fission Product Behaviour in Gas Cooled Reactors,* TECDOC-9787, 1997.

[26] G. K. Miller and D. L. Knudson, *AGR-1 Pre-Test Prediction Analysis using the PARFUME Code,* Idaho National Laboratory, EDF-5741, Rev. 1, 2007.

[27] W. F. Skerjanc and B. P. Collin, *Assessment of Material Properties for TRISO Fuel Particles used in PARFUME,* Idaho National Laboratory, INL/EXT-18-44631, Rev. 0, 2018.

[28] G. R. Longhurst, D. F. Holland, J. L. Jones and B. J. Merrill, *TMAP4 User's Manual,* Idaho National Laboratory, EGG-FSP-10315, 1992.

[29] J. M. Harp, J. D. Stempien and P. A. Demkowicz, *Gamma Spectrometry Examination of the AGR-3/4 Irradiation,* Idaho National Laboratory, INL/EXT-20-58254, Rev. 1, 2021.

[30] J. D. Stempien, P. A. Demkowicz, J. M. Harp and P. L. Winston, *AGR-3/4 Experiment Preliminary Mass Balance,* INL/EXT-18-46049, Rev. 0, Idaho National Laboratory, 2018.

[31] X.-5. M. C. Team, *"MCNP - A General Monte Carlo N-Particle Transport Code, Version 5,* Volume I, LA-UR-03-1987 and Volume II, LA-CP-0245, Los Alamos National Laboratory, 2004.

[32] A. G. Croff, "ORIGEN2: A Versatile Computer Code for Calculating the Nuclide Compositions and Characteristics of Nuclear Materials," *Nuclear Technology,* vol. 62, pp. 335-352, 1983.

[33] R. G. Ambrosek, *Thermal Evaluations for AGR-3/4 Experment in the NEFT,* ECAR-1361, Rev. 0, Idaho National Laboratory, 2011.

[34] P. W. Humrichouse, B. P. Collin, G. L. Hawkes, J. M. Harp, P. A. Demkowicz and D. A. Petti, *Modeling and Analysis of Fission Product Transport in the AGR-3/4 Experiment,* 2016 International Topical Meeting on High Temperature Reactor Technology, 2016.

[35] J. D. Stempien, *Measurement of Fission Product Concentration Profiles in AGR-3/4 TRISO Fuel Graphitic Matrix and Nuclear Graphites,* INL/EXT-21-62863, Rev. 0, Idaho National Laboratory, 2021.

Appendix A

Compact Distribution for Burnup, Fluence, and TAVA Temperature
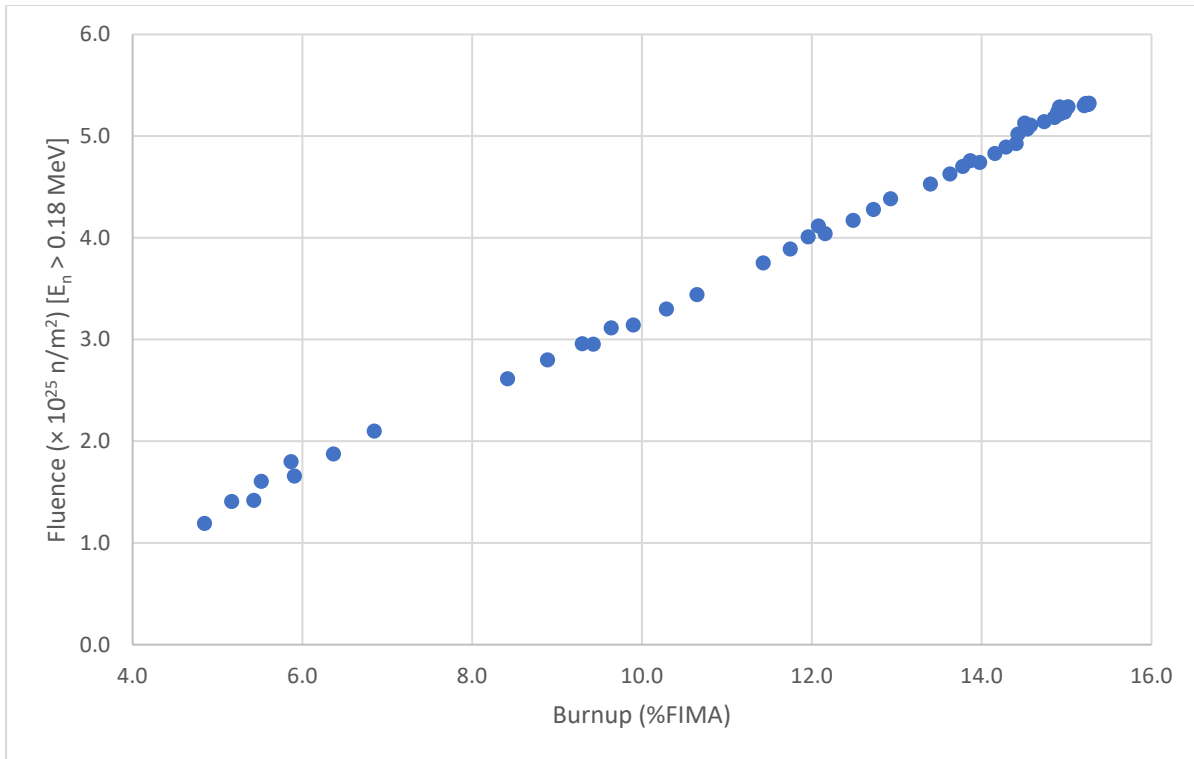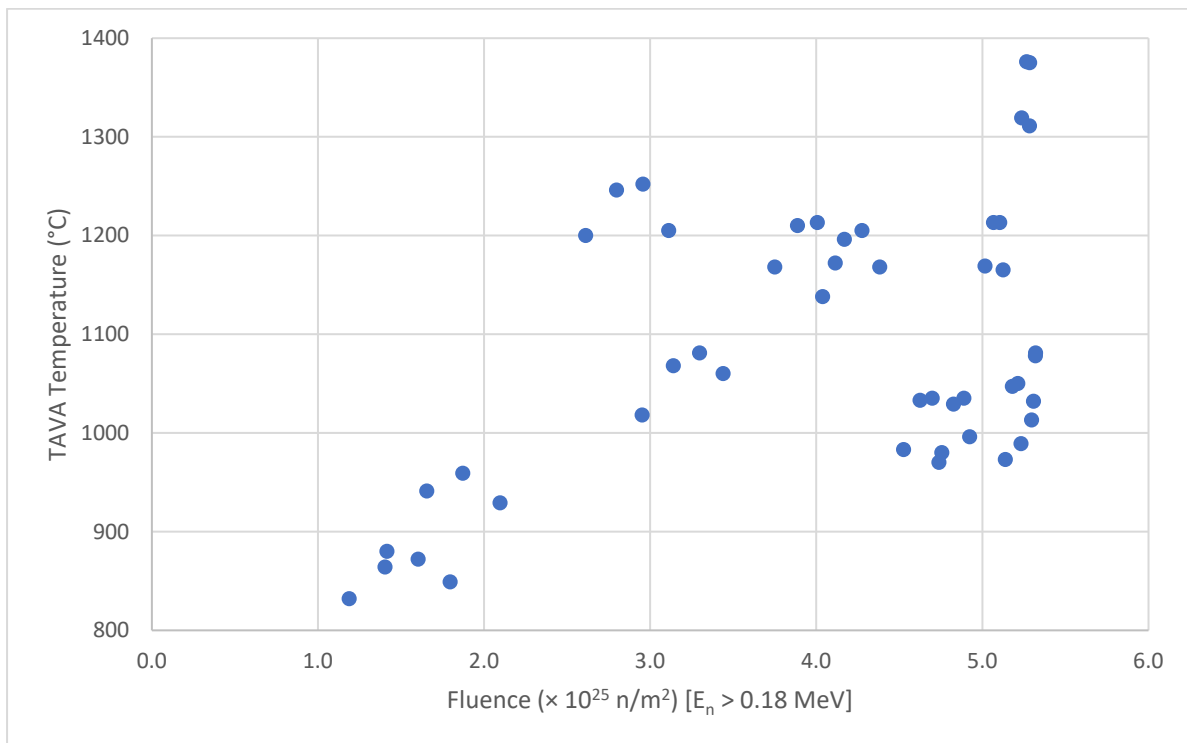
Figure A1. Compact fluence versus burnup.

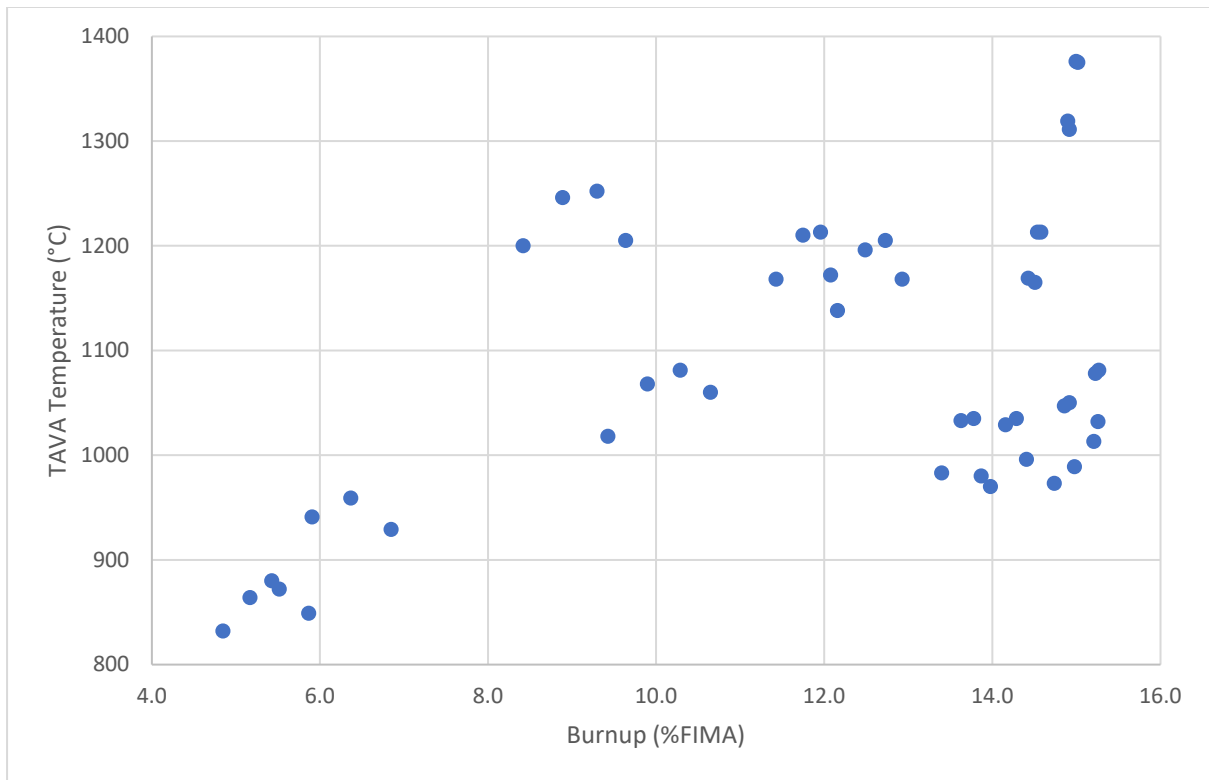Figure A2. Compact TAVA temperature versus fluence.

Figure A3. Compact TAVA temperature versus burnup.

Appendix B

Ag Release Fraction from Compact Gamma Scanning

Table B1. Ag gamma scan measured and calculated Ag release fraction.

| Compact	TAVA (°C)	PIE	PARFUME Driver + DTF	PARFUME Δ (Meas. - Calc.)	BISON Driver + DTF	BISON Δ (Meas. - Calc.)
			Ag Release Fraction			
12-4	832	7.72E-01	8.86E-03	0.76	1.06E-02	0.76
12-3	864	7.88E-01	9.72E-03	0.78	1.06E-02	0.78
12-2	872	5.62E-01	9.85E-03	0.55	1.06E-02	0.55
12-1	849	3.37E-01	9.43E-03	0.33	1.06E-02	0.33
10-4	1168	9.50E-01	2.15E-01	0.73	2.01E-01	0.75
10-3	1210	9.15E-01	3.39E-01	0.58	3.19E-01	0.60
10-2	1213	8.04E-01	3.49E-01	0.46	3.28E-01	0.48
10-1	1172	8.45E-01	2.25E-01	0.62	2.10E-01	0.64
8-4	1169	8.40E-01	4.00E-01	0.44	3.74E-01	0.47
8-3	1213	8.37E-01	5.60E-01	0.28	5.31E-01	0.31
8-2	1213	8.57E-01	5.61E-01	0.30	5.32E-01	0.32
8-1	1165	8.22E-01	3.88E-01	0.43	3.62E-01	0.46
7-4	1319	8.50E-01	7.83E-01	0.07	7.63E-01	0.09
7-3	1376	8.79E-01	8.79E-01	0.00	8.69E-01	0.01
7-2	1375	8.89E-01	8.78E-01	0.01	8.67E-01	0.02
7-1	1311	8.74E-01	7.67E-01	0.11	7.45E-01	0.13
5-4	989	2.97E-01	1.23E-02	0.28	1.20E-02	0.28
5-3	1050	2.28E-01	3.54E-02	0.19	3.27E-02	0.20
5-2	1047	1.94E-01	3.31E-02	0.16	3.06E-02	0.16
5-1	973	3.17E-01	1.12E-02	0.31	1.11E-02	0.31
4-4	996	2.91E-01	1.32E-02	0.28	1.28E-02	0.28
4-3	1035	3.29E-01	2.60E-02	0.30	2.42E-02	0.30
4-2	1029	2.87E-01	2.31E-02	0.26	2.16E-02	0.27
4-1	970	3.41E-01	1.12E-02	0.33	1.10E-02	0.33
3-4	1168	9.51E-01	1.84E-01	0.77	1.71E-01	0.78
3-3	1205	9.08E-01	2.83E-01	0.63	2.65E-01	0.64
3-2	1196	9.29E-01	2.60E-01	0.67	2.43E-01	0.69
3-1	1138	9.36E-01	1.27E-01	0.81	1.18E-01	0.82
1-4	929	1.90E-01	1.06E-02	0.18	1.06E-02	0.18
1-3	959	1.78E-01	1.08E-02	0.17	1.07E-02	0.17
1-2	941	4.41E-01	1.06E-02	0.43	1.06E-02	0.43
1-1	880	2.39E-01	1.05E-02	0.23	1.06E-02	0.23
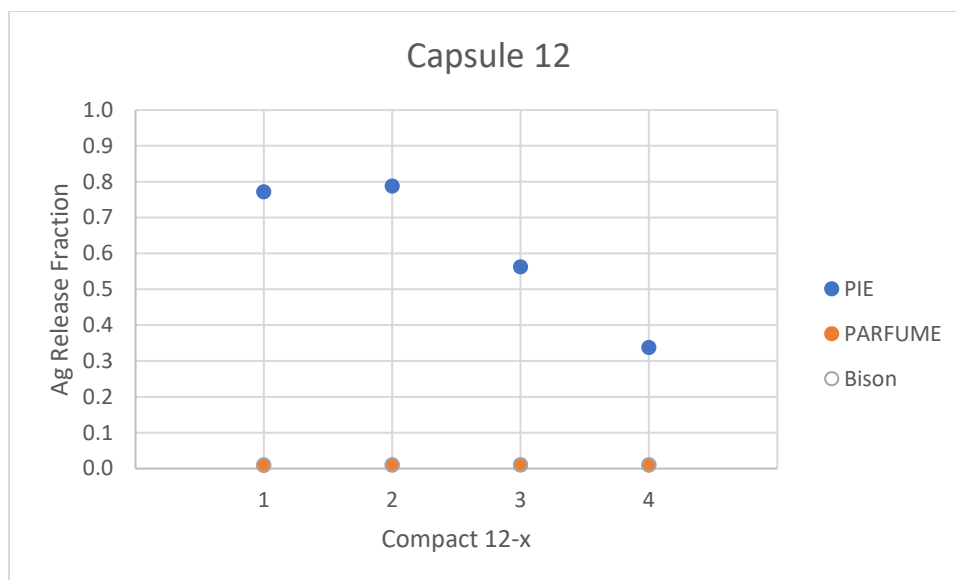
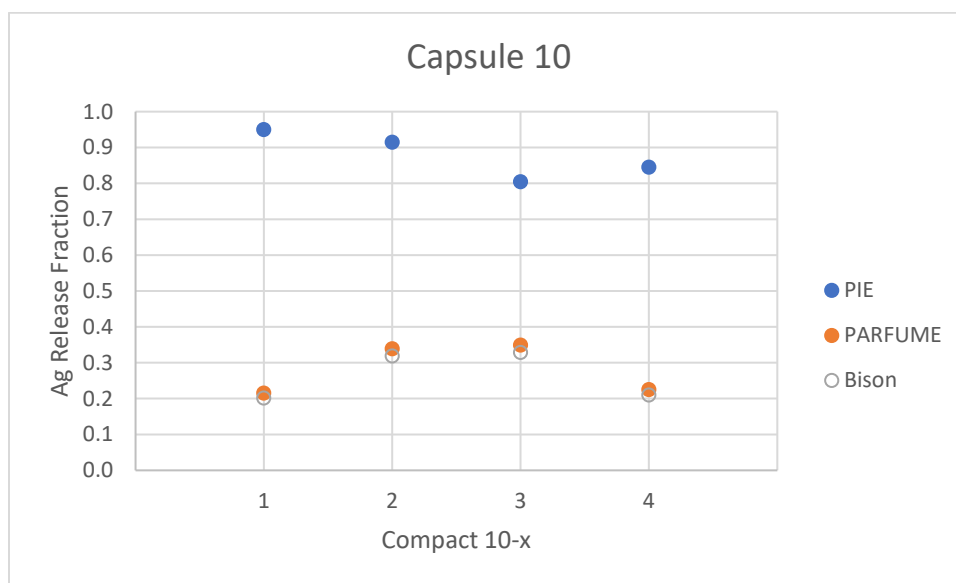Figure B1. Capsule 12 compact gamma scan Ag release fraction.

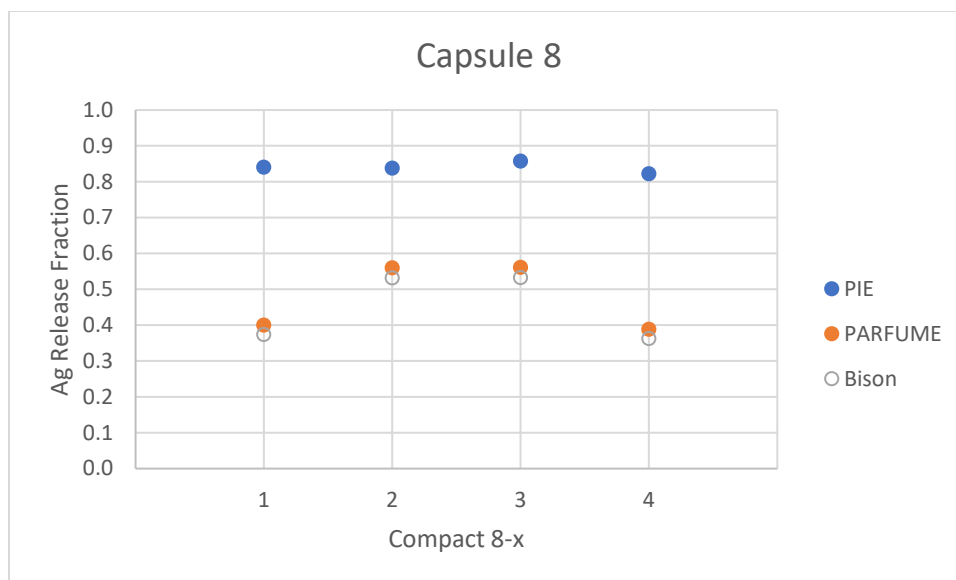Figure B2. Capsule 10 compact gamma scan Ag release fraction.

Figure B3. Capsule 8 compact gamma scan Ag release fraction.
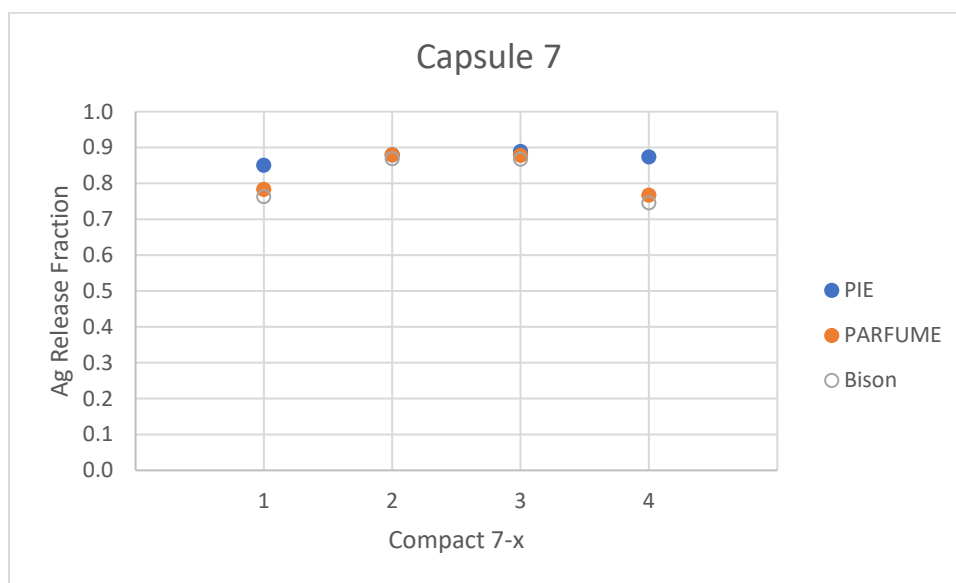

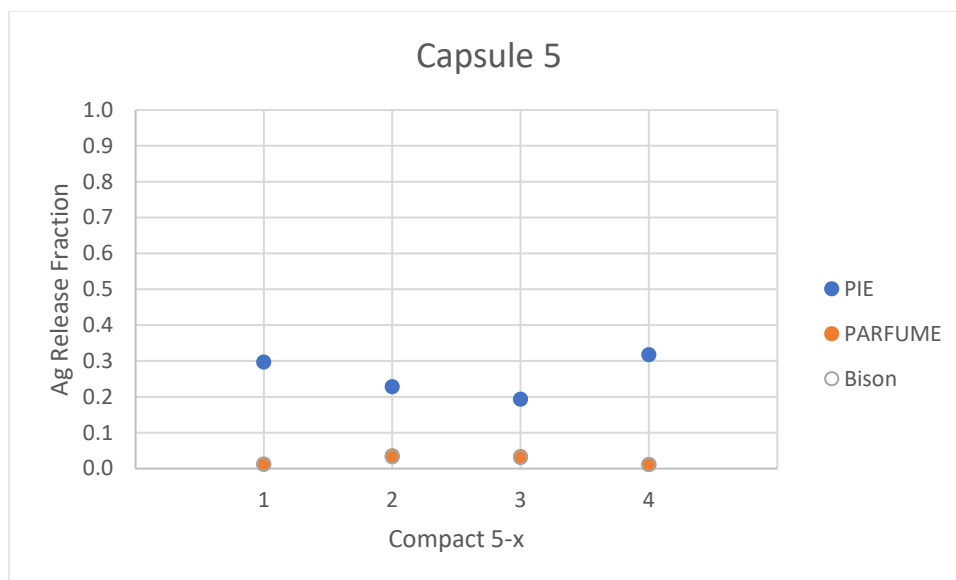Figure B4. Capsule 7 compact gamma scan Ag release fraction.

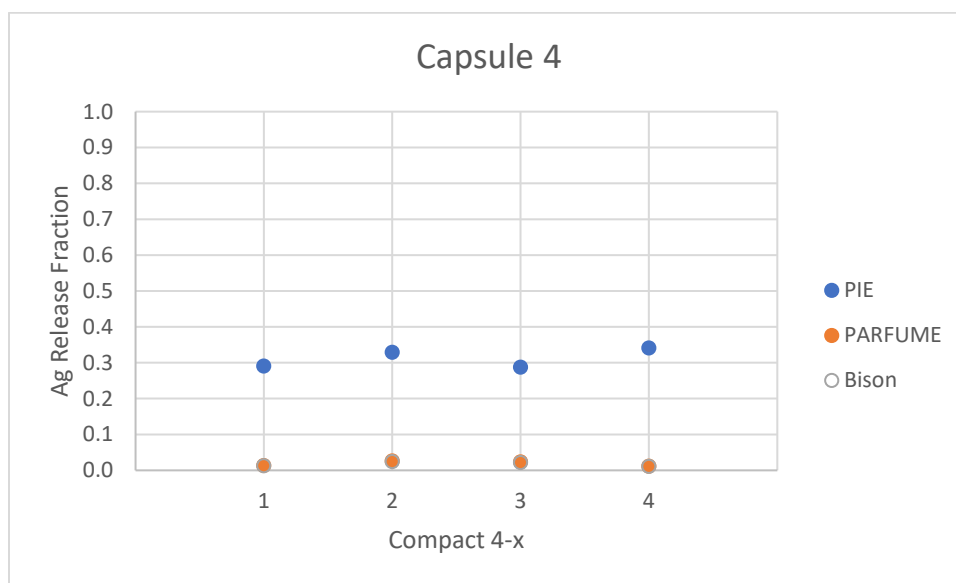Figure B5. Capsule 5 compact gamma scan Ag release fraction.

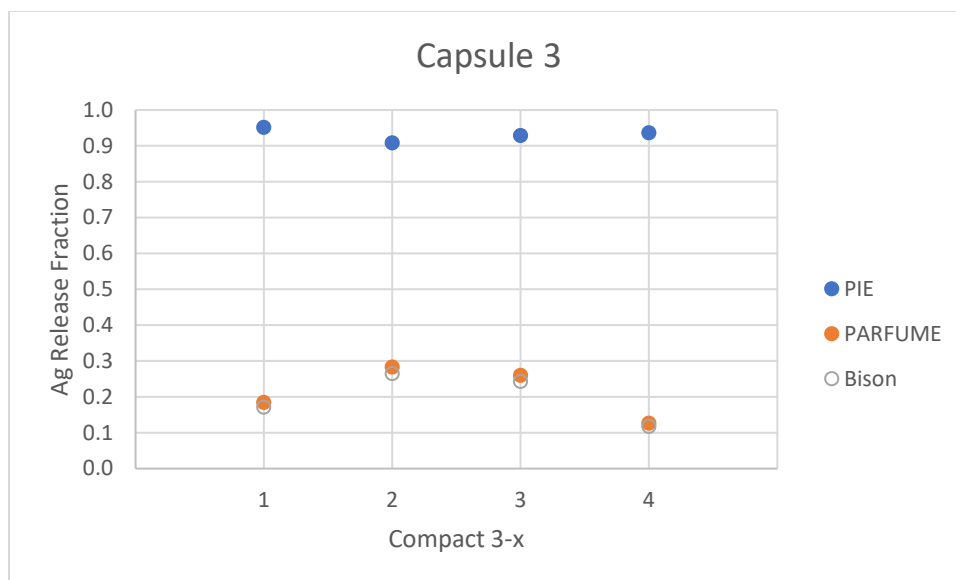Figure B6. Capsule 4 compact gamma scan Ag release fraction.

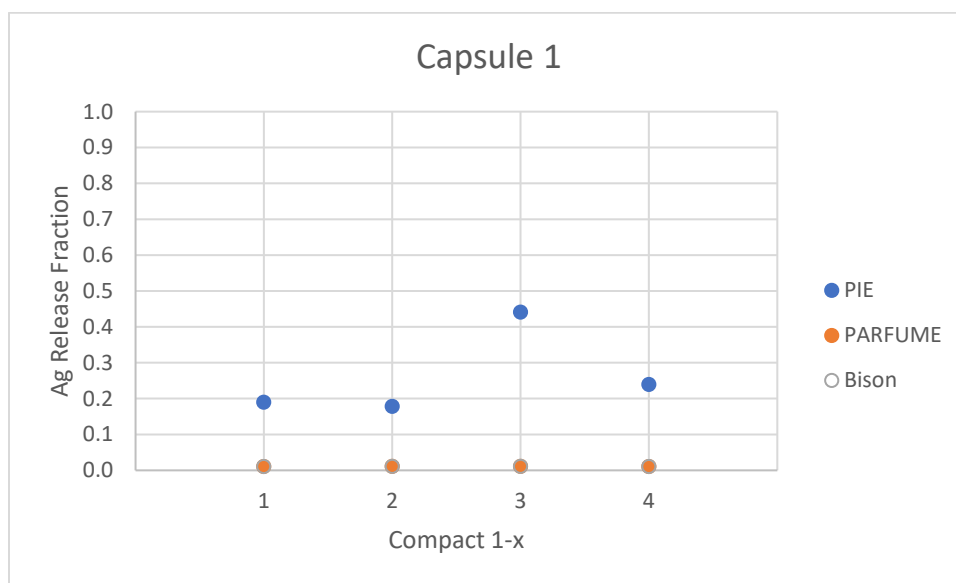Figure B7. Capsule 3 compact gamma scan Ag release fraction.

Figure B8. Capsule 1 compact gamma scan Ag release fraction.

Appendix C

Fission Product Source Term

The total source term for silver, cesium, and strontium used to calculate the FP diffusion through the compact/IR/OR/sink ring are summarized in Table C1. The values presented in Table C1 are the total source term from both the driver and DTF particles.

Table C1. FP source term (mols).

Capsule	Ag			Cs			Sr		
	Driver	DTF	Total[1]	Driver	DTF	Total[1]	Driver	DTF	Total[1]
12	5.86E-20	4.78E-11	5.06E-13	8.59E-33	2.78E-10	2.94E-12	5.36E-19	1.54E-10	1.63E-12
10	7.77E-11	2.36E-10	7.93E-11	2.03E-12	1.77E-08	1.89E-10	1.29E-10	3.36E-10	1.31E-10
8	1.03E-11	3.17E-10	1.35E-11	7.02E-17	1.59E-08	1.68E-10	1.68E-11	3.64E-10	2.05E-11
7	2.20E-10	3.41E-10	2.21E-10	4.80E-11	2.33E-08	2.94E-10	6.38E-10	7.51E-10	6.39E-10
5	1.37E-11	3.28E-10	1.71E-11	4.54E-16	1.69E-08	1.79E-10	2.24E-11	3.72E-10	2.61E-11
4	9.96E-12	3.07E-10	1.31E-11	7.03E-17	1.55E-08	1.64E-10	1.66E-11	3.58E-10	2.02E-11
3	6.12E-11	2.59E-10	6.33E-11	8.81E-13	1.85E-08	1.97E-10	9.84E-11	3.37E-10	1.01E-10
1	1.67E-14	7.97E-11	8.59E-13	1.02E-27	2.15E-09	2.28E-11	6.13E-14	1.74E-10	1.90E-12

1. Total = Driver × (1872/1892) + DTF × (20/1892).

Figure C1. Capsule 1 FP source term time evolution.

Figure C2. Capsule 3 FP source term time evolution.
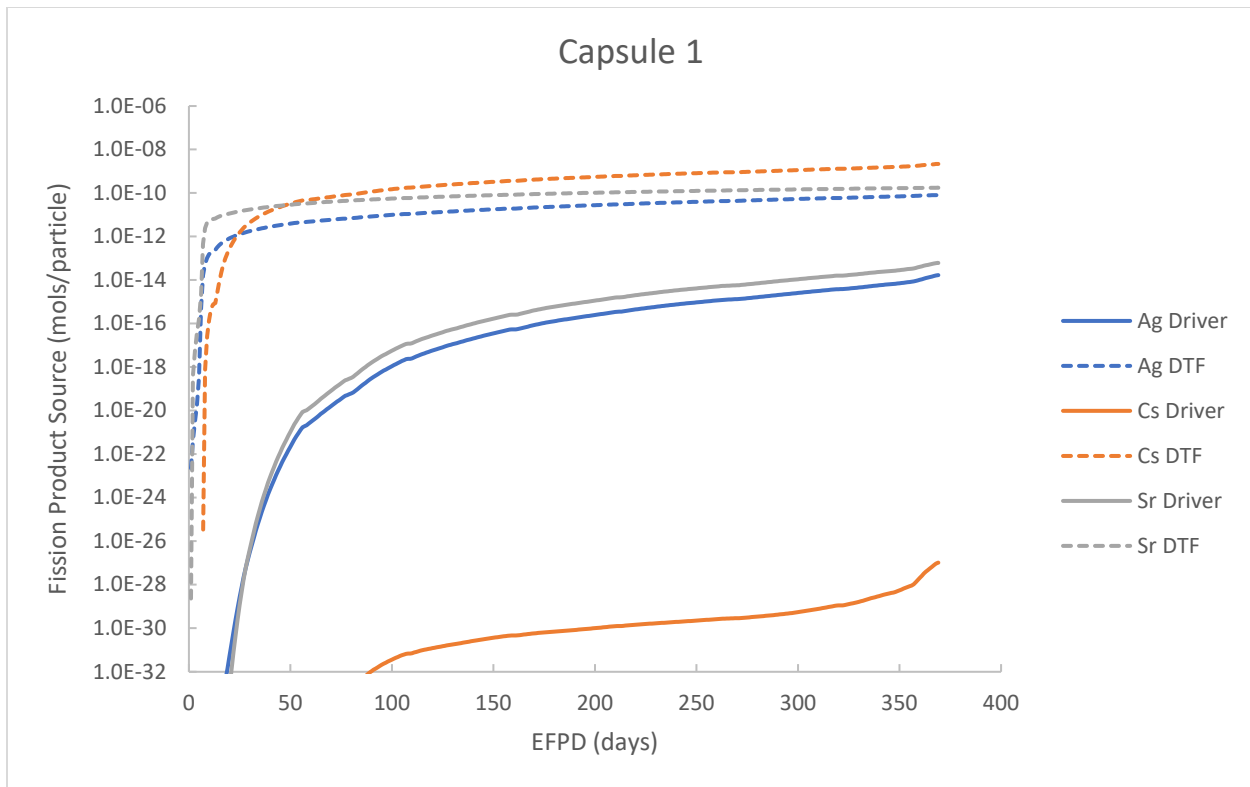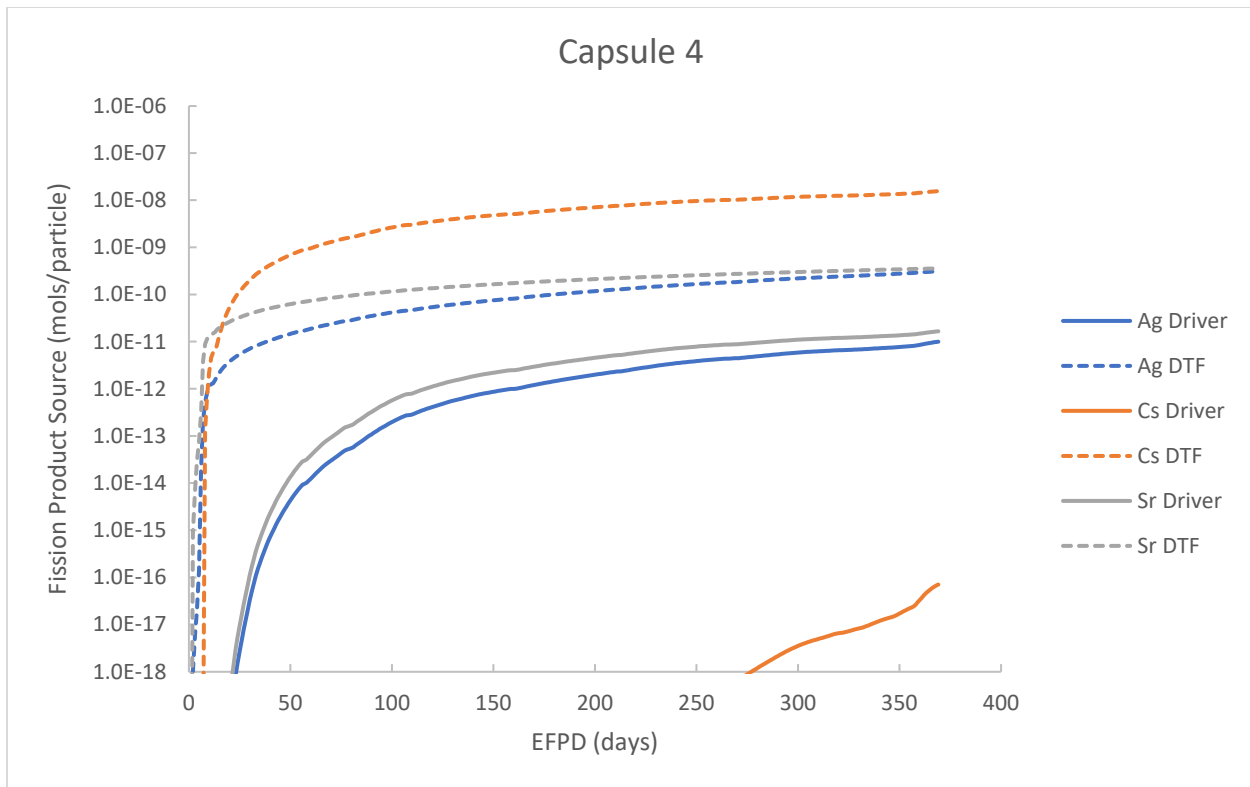
Figure C3. Capsule 4 FP source term time evolution.
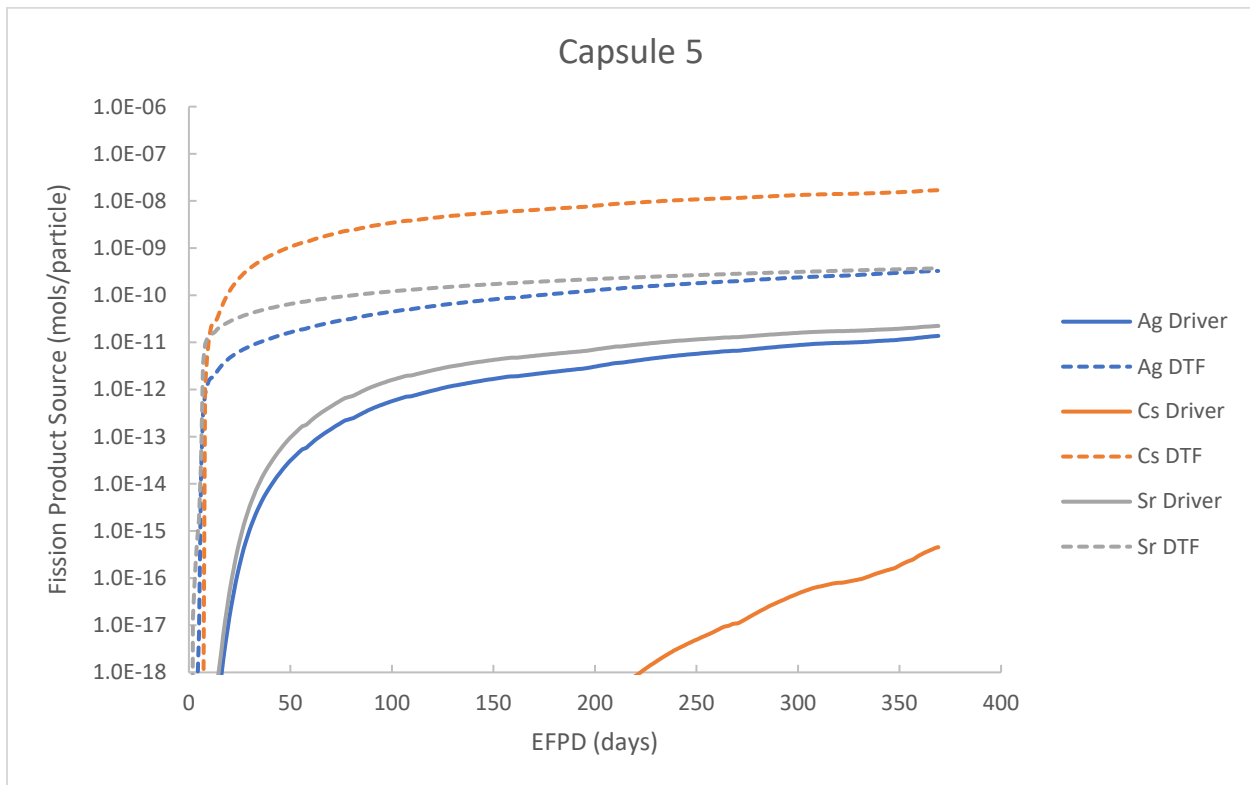
Figure C4. Capsule 5 FP source term time evolution.
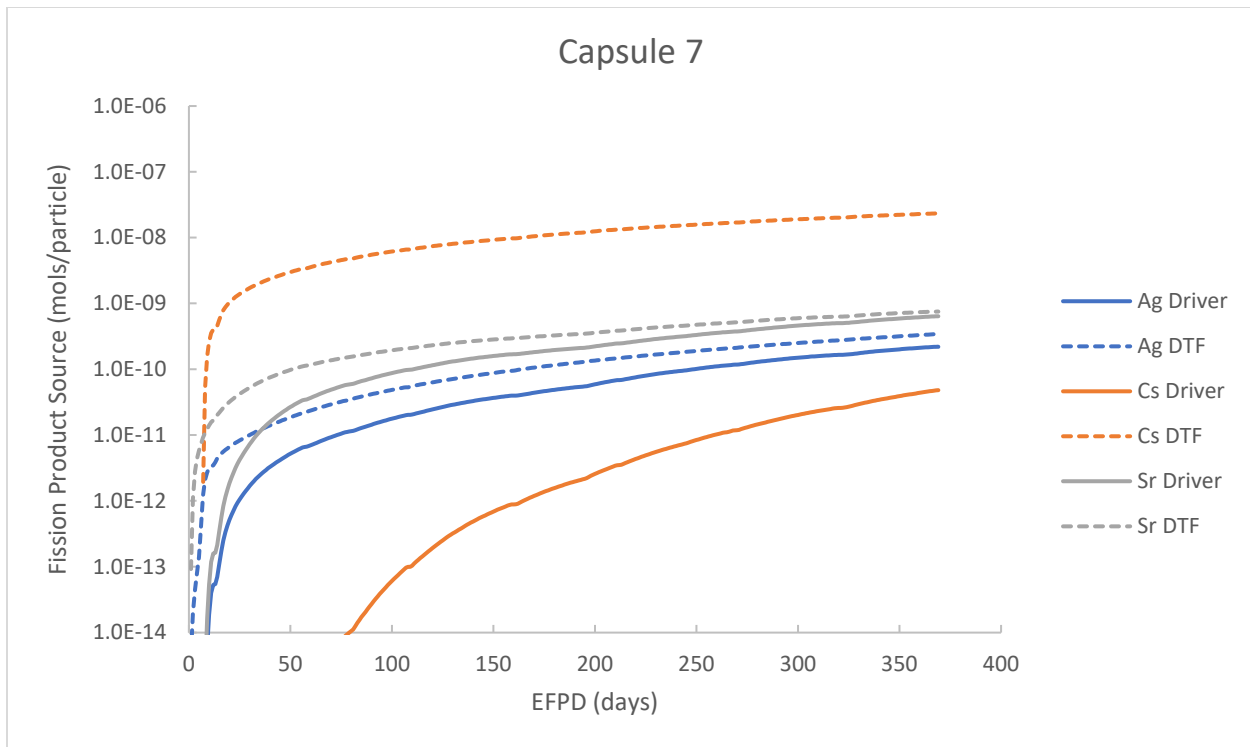
Figure C5. Capsule 7 FP source term time evolution.

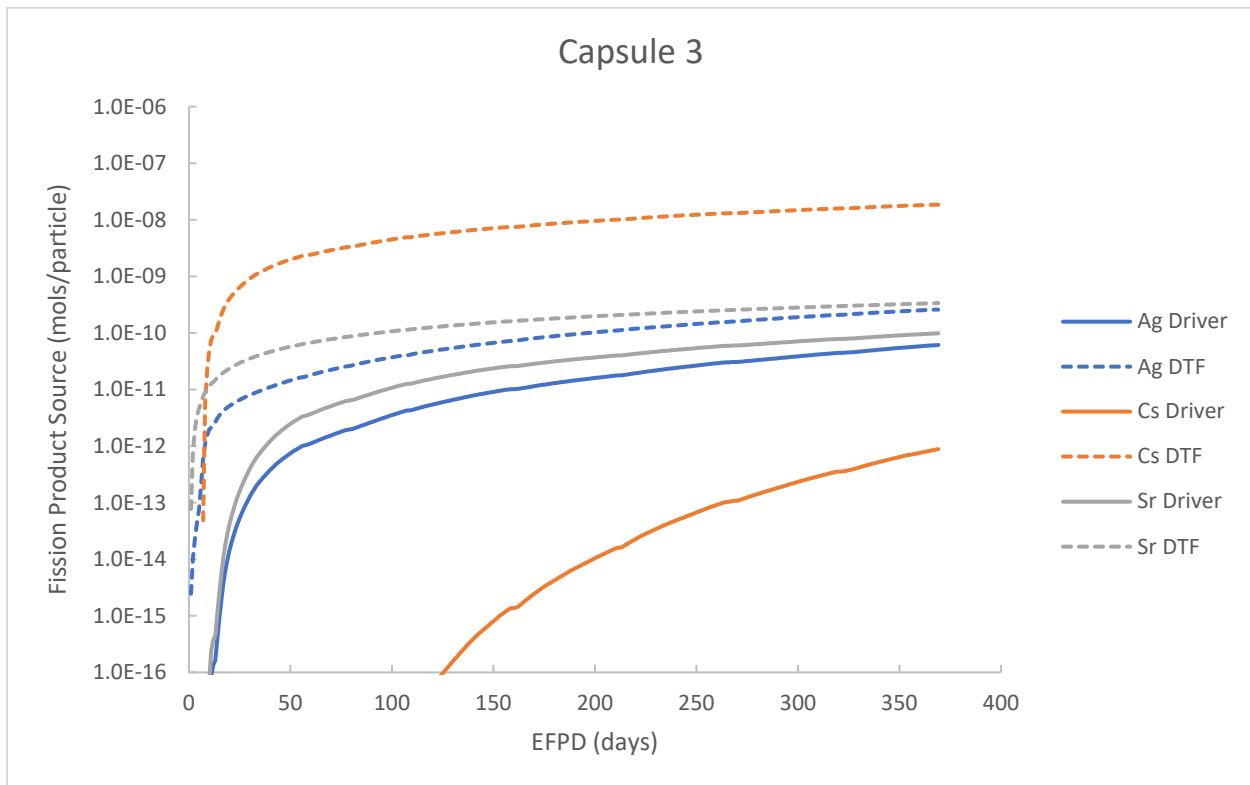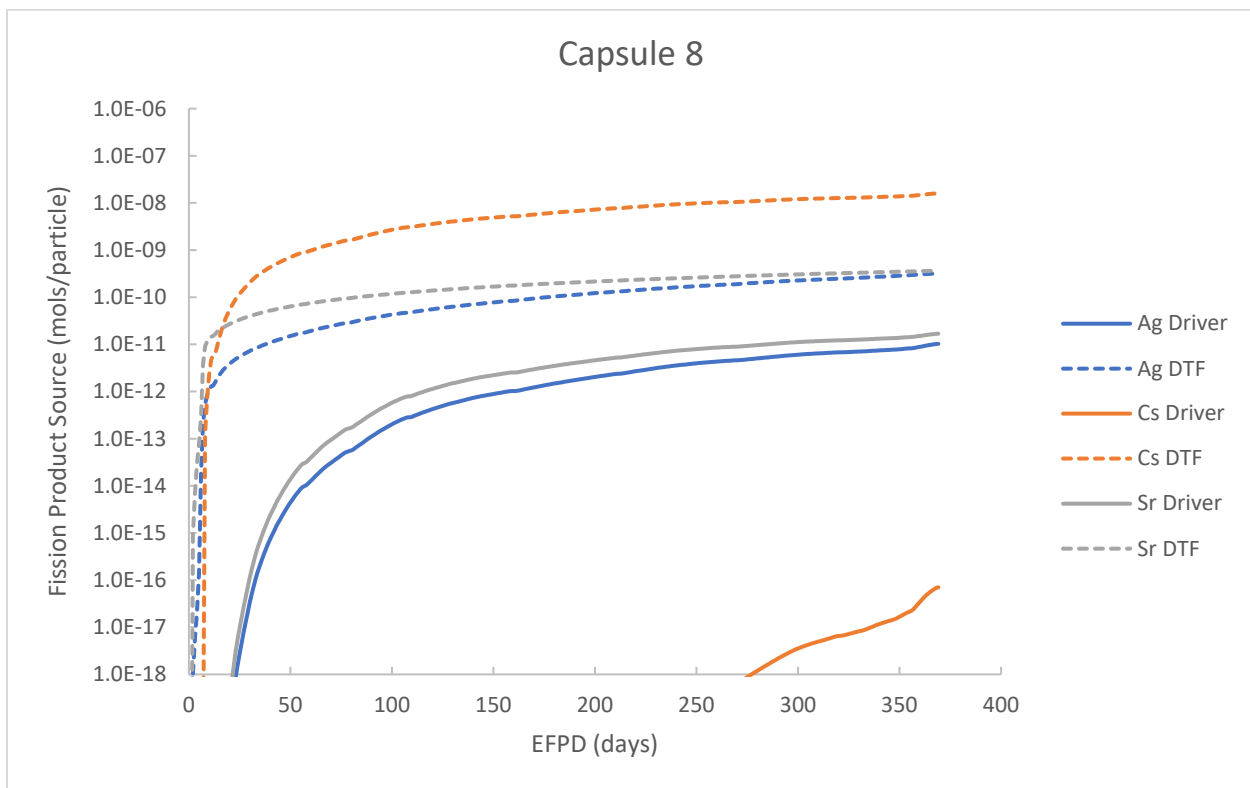Figure C6. Capsule 8 FP source term time evolution.
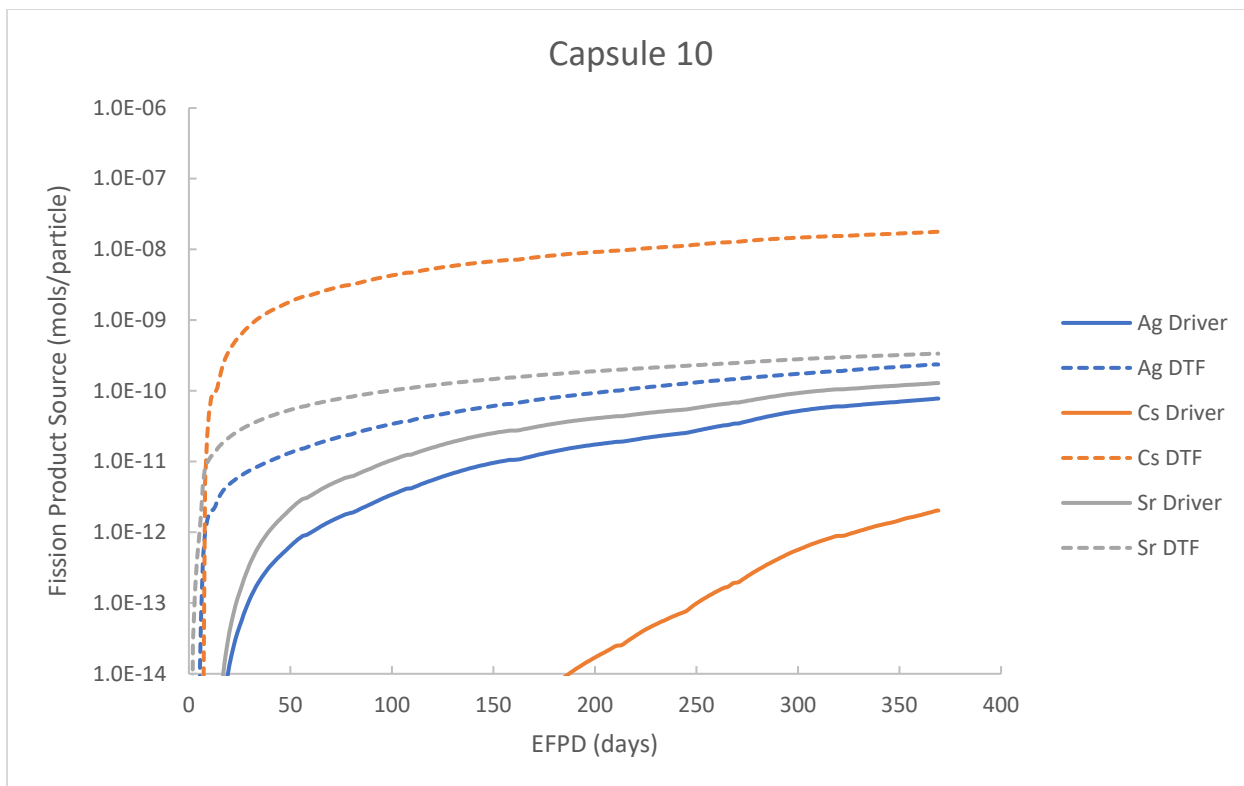
Figure C7. Capsule 10 FP source term time evolution.
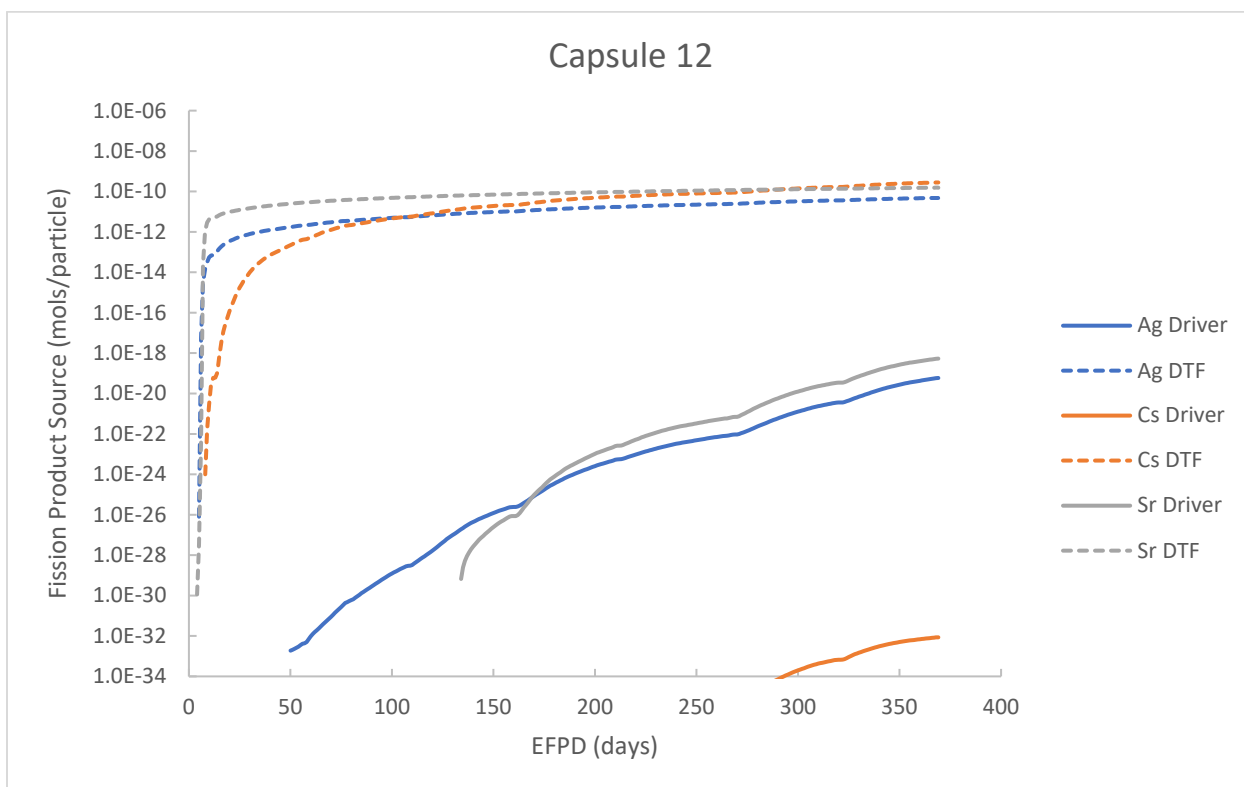
Figure C8. Capsule 12 FP source term time evolution.

Appendix D

Capsule Compact and Ring Temperatures
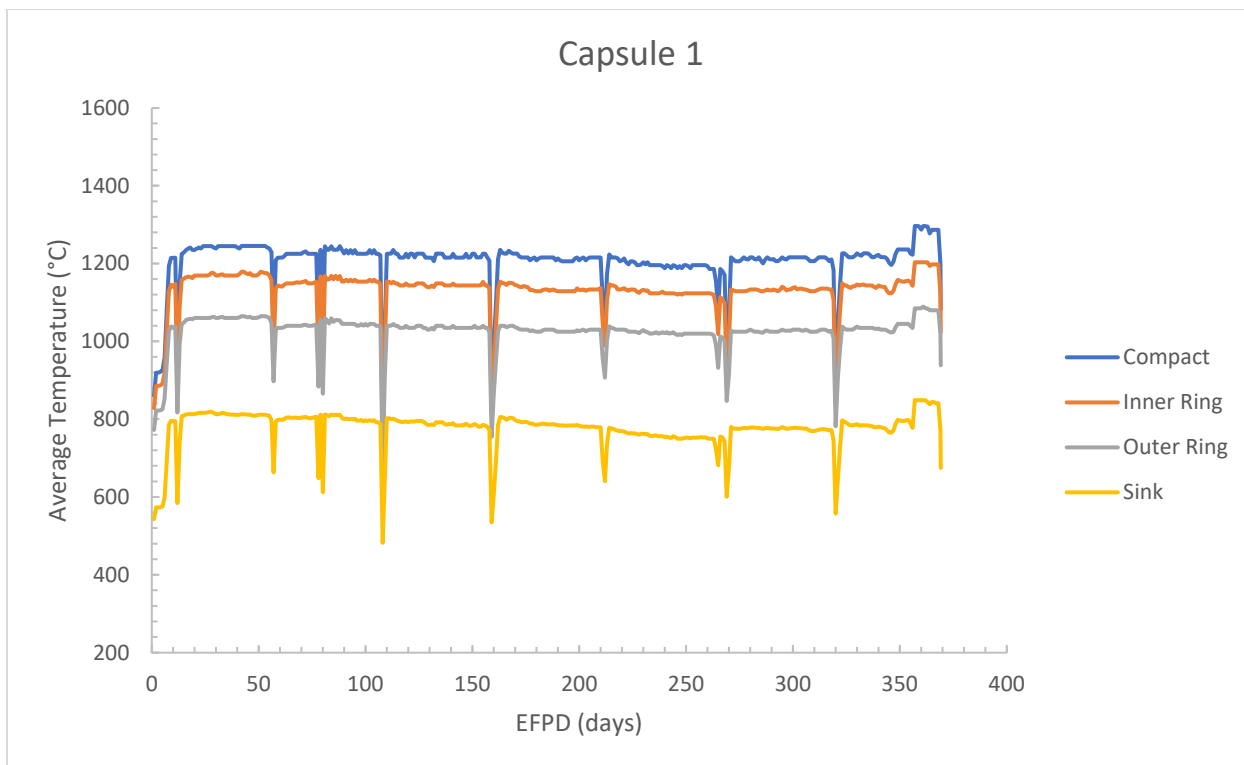
Figure D1. Capsule 1 TAVA daily temperatures.
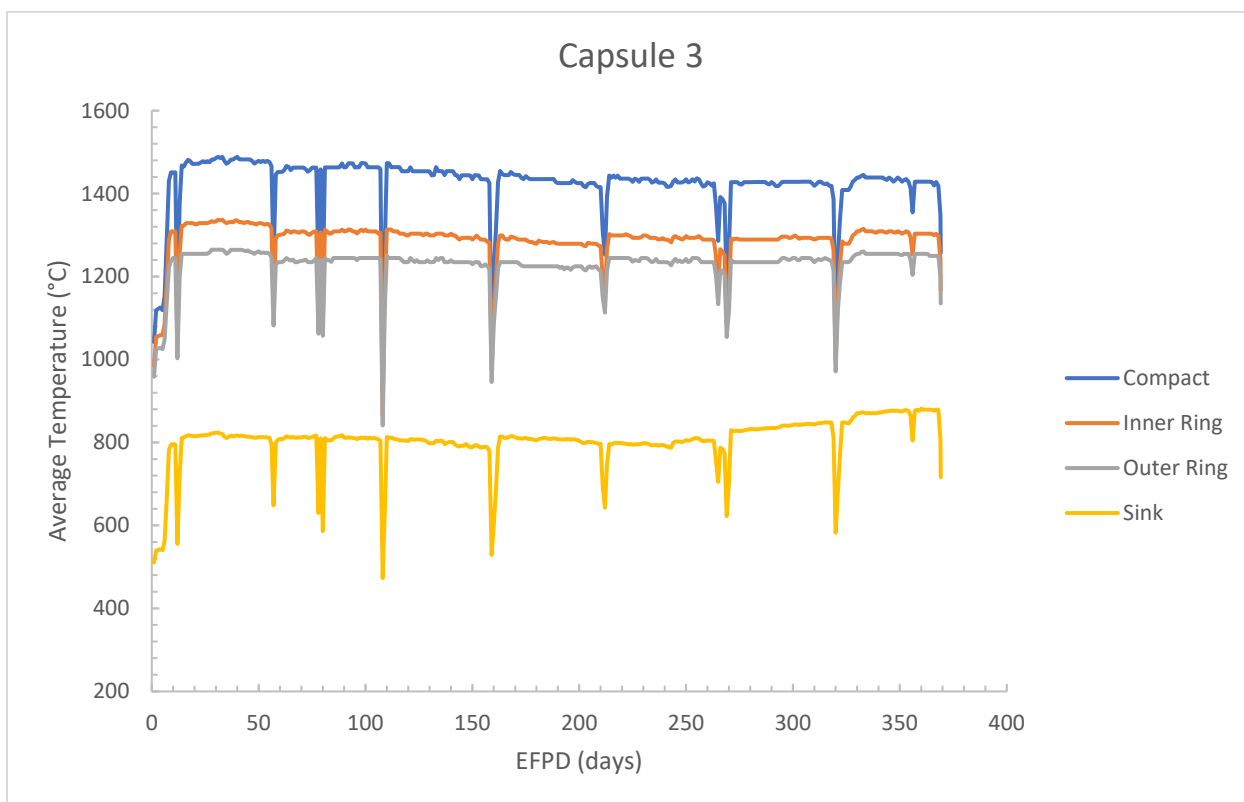
Figure D2. Capsule 3 TAVA daily temperatures.
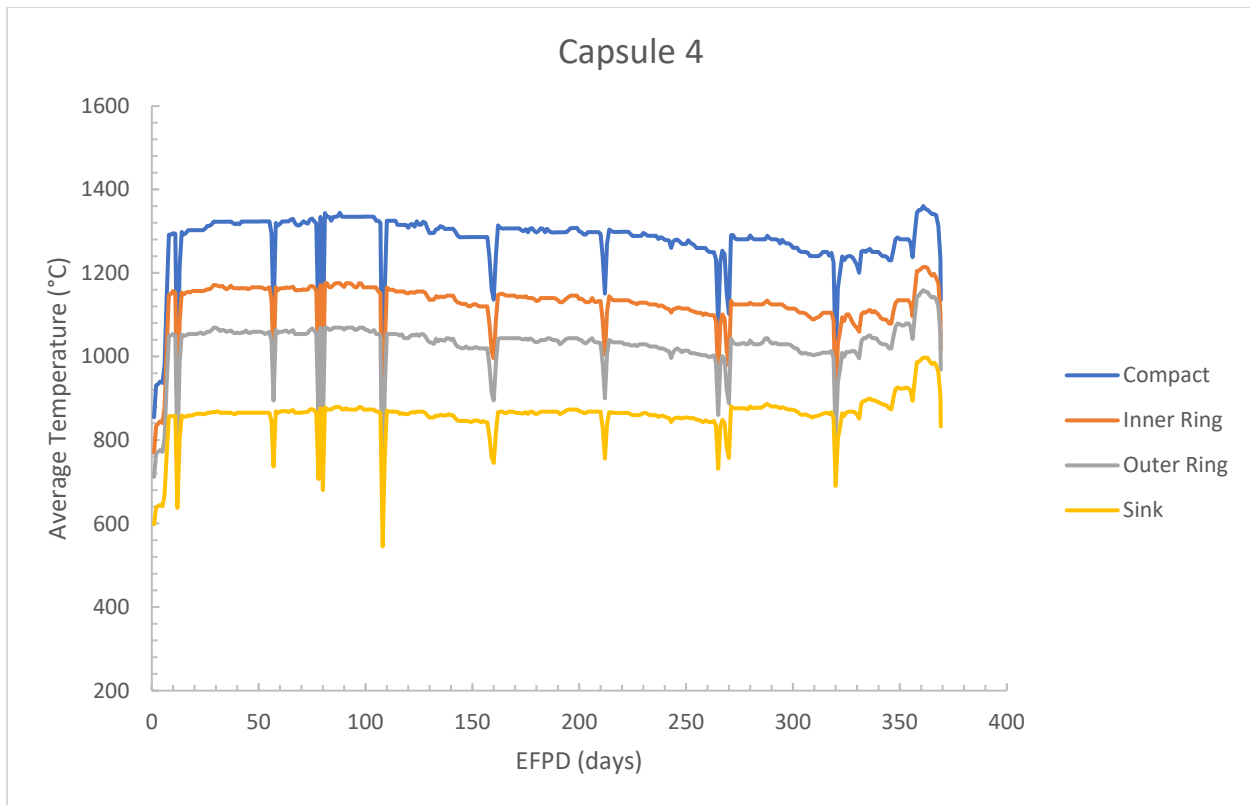
Figure D3. Capsule 4 TAVA daily temperatures.
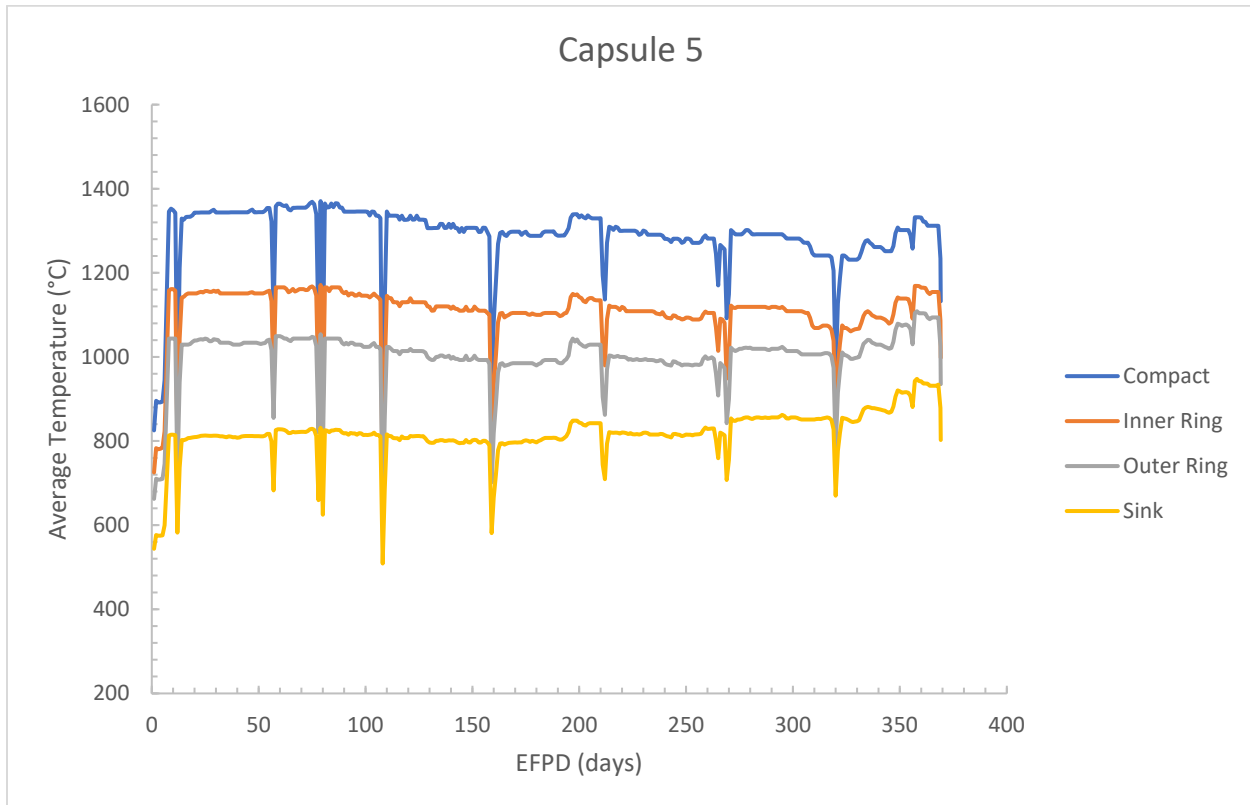
Figure D4. Capsule 5 TAVA daily temperatures.

Figure D5. Capsule 7 TAVA daily temperatures.

Figure D6. Capsule 8 TAVA daily temperatures.

Figure D7. Capsule 10 TAVA daily temperatures.

Figure D8. Capsule 12 TAVA daily temperatures.

Appendix E

PIE Data and Measured vs. Calculated Concentration Profiles

Table E1. Capsule 3 measured inner and outer ring radial concentrations [35].

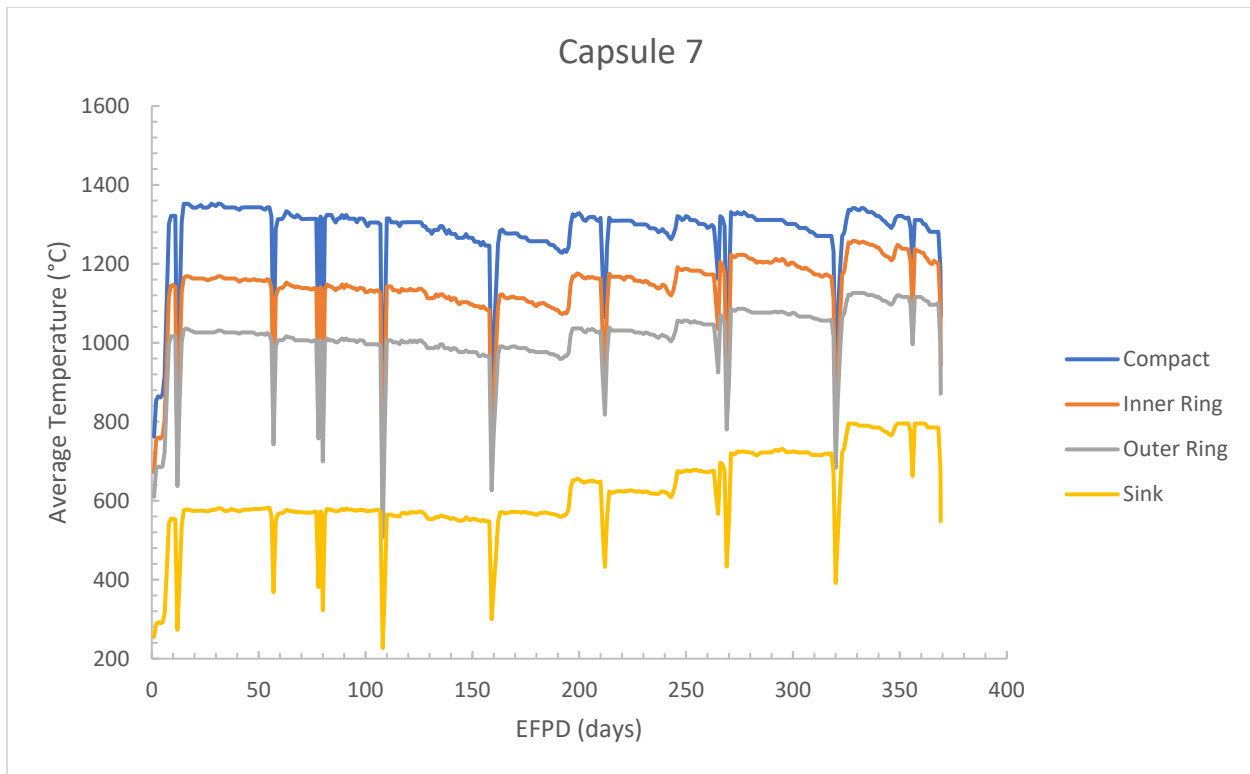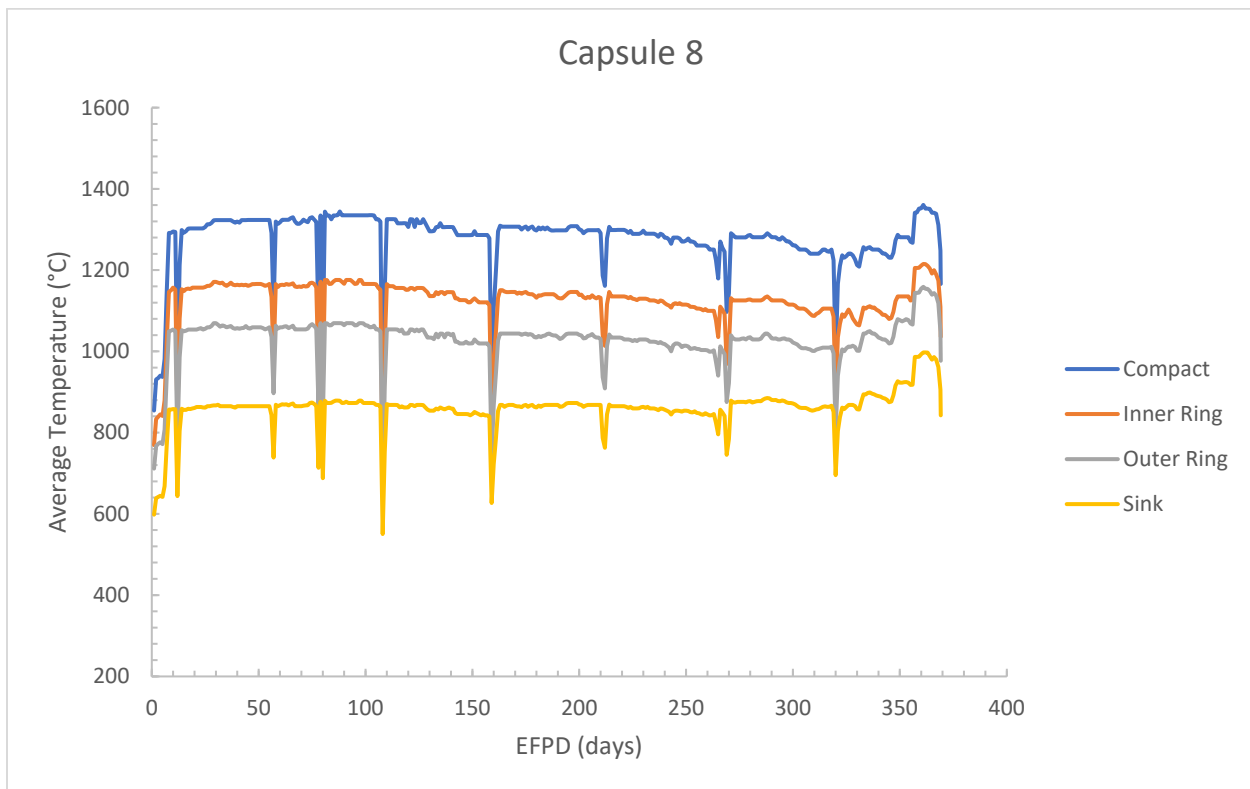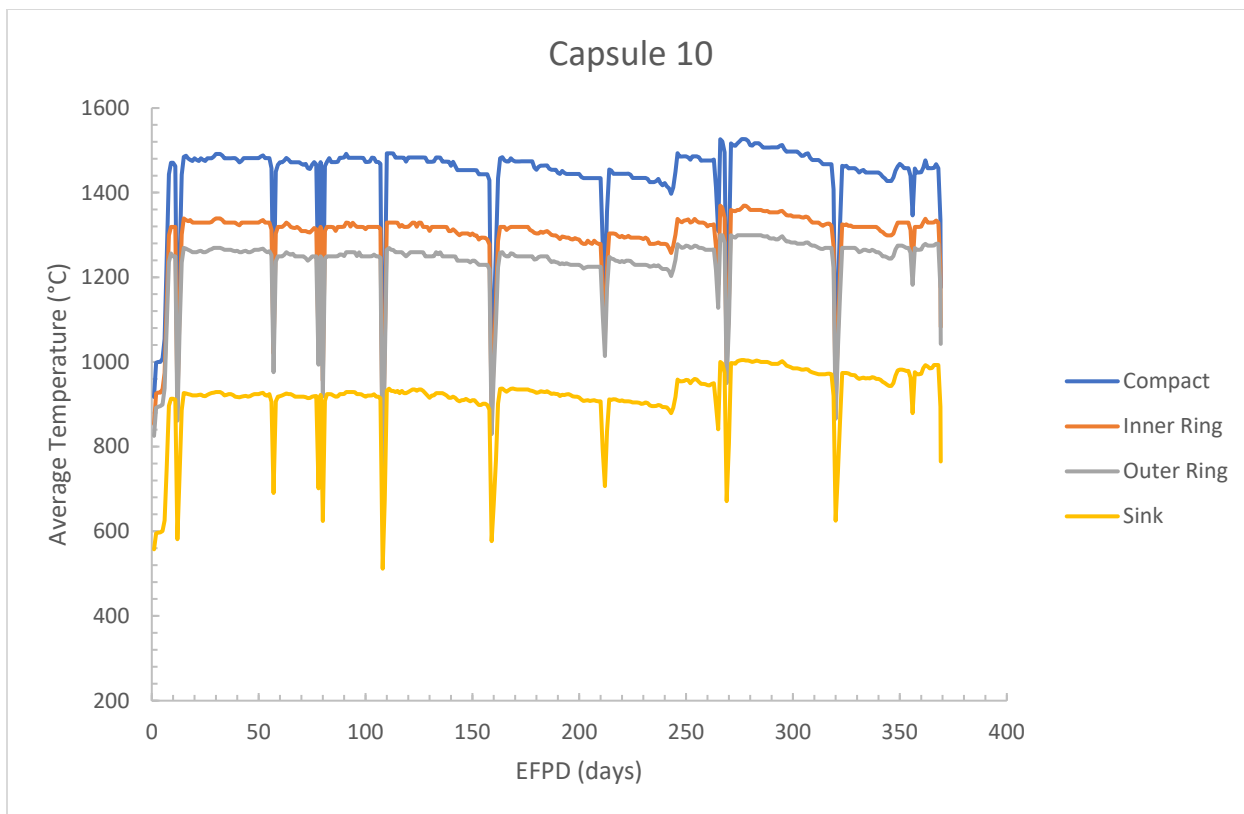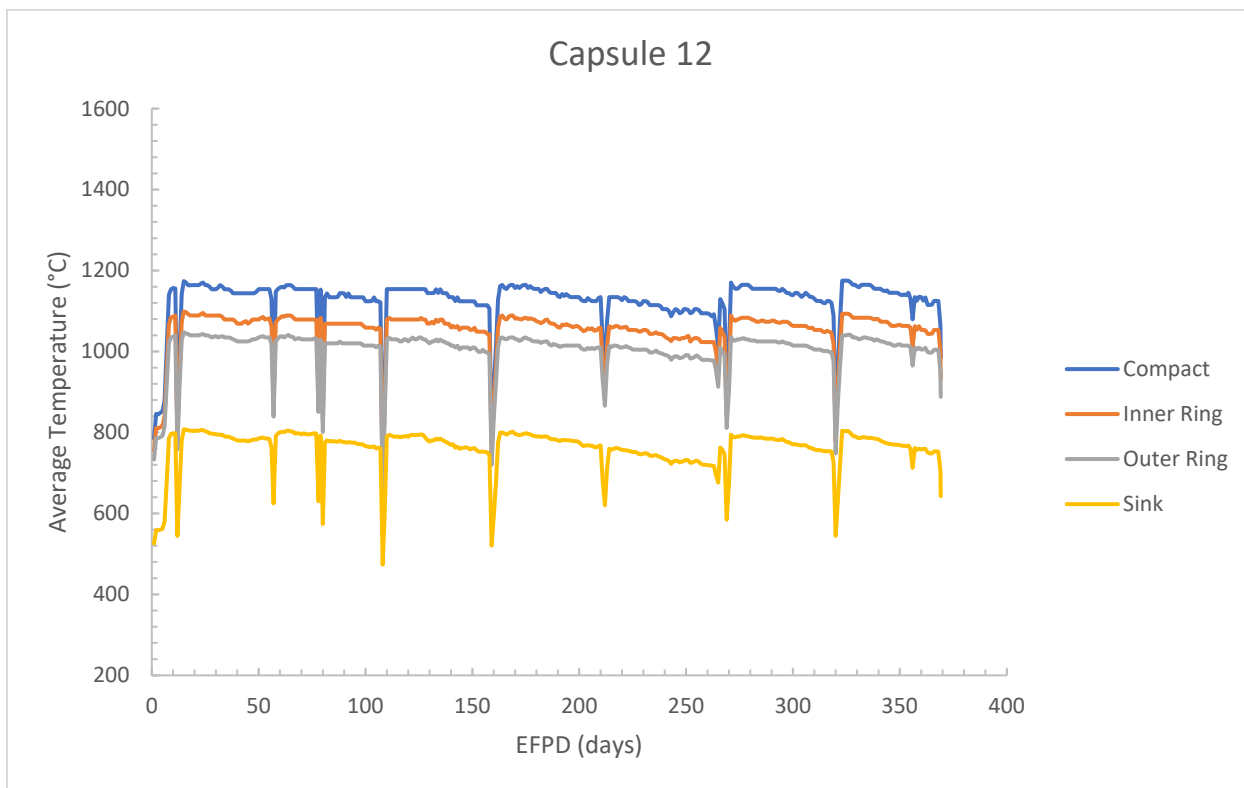| Ring	Radius (mm)	Ag-110m (Bq/mm^3)	Ag-110m (mol/m^3)	Cs-134 (Bq/mm^3)	Cs-134 (mol/m^3)	Cs-137 (Bq/mm^3)	Cs-137 (mol/m^3)	Sr-90 (Bq/mm^3)	Sr-90 (mol/m^3)
		Capsule 3							
Inner	11.82	1.99E+02	1.58E-03	3.36E+02	1.57E-03	4.94E+02	2.54E-03	4.91E+02	1.87E-03
	11.38	4.27E+02	3.38E-03	5.29E+02	2.47E-03	5.96E+02	3.06E-03	1.83E+02	6.98E-04
	10.87	3.25E+02	2.57E-03	4.50E+02	2.10E-03	4.90E+02	2.52E-03	5.72E+01	2.18E-04
	10.36	3.33E+02	2.64E-03	5.39E+02	2.52E-03	5.96E+02	3.06E-03	4.40E+01	1.68E-04
	9.85	4.09E+02	3.24E-03	7.27E+02	3.40E-03	7.98E+02	4.10E-03	4.07E+01	1.55E-04
	9.34	2.24E+02	1.77E-03	7.23E+02	3.38E-03	7.87E+02	4.04E-03	3.64E+01	1.39E-04
	8.84	1.07E+02	8.48E-04	8.81E+02	4.12E-03	9.62E+02	4.94E-03	3.30E+01	1.26E-04
	8.33	8.30E+01	6.57E-04	1.03E+03	4.82E-03	1.12E+03	5.75E-03	1.32E+01	5.04E-05
	7.82	7.39E+01	5.85E-04	1.10E+03	5.14E-03	1.20E+03	6.16E-03	2.05E+01	7.82E-05
	7.31	7.92E+01	6.27E-04	1.28E+03	5.98E-03	1.38E+03	7.09E-03	1.68E+03	6.41E-03
	6.80	6.42E+01	5.09E-04	1.16E+03	5.42E-03	1.27E+03	6.52E-03	5.23E+04	2.00E-01
	6.43	5.61E+01	4.44E-04	1.52E+03	7.11E-03	1.79E+03	9.19E-03	6.11E+04	2.33E-01
Outer	16.36	5.35E+01	4.24E-04	4.19E+02	1.96E-03	5.19E+02	2.67E-03	1.55E+02	5.91E-04
	15.97	1.10E+02	8.71E-04	2.40E+02	1.12E-03	2.43E+02	1.25E-03	5.57E+01	2.12E-04
	15.59	1.78E+02	1.41E-03	2.54E+02	1.19E-03	2.58E+02	1.32E-03	5.46E+01	2.08E-04
	15.21	2.42E+02	1.92E-03	2.87E+02	1.34E-03	2.98E+02	1.53E-03	5.11E+01	1.95E-04
	14.83	3.05E+02	2.42E-03	3.03E+02	1.42E-03	3.10E+02	1.59E-03	5.22E+01	1.99E-04
	14.45	3.65E+02	2.89E-03	3.45E+02	1.61E-03	3.61E+02	1.85E-03	5.47E+01	2.09E-04
	14.07	4.23E+02	3.35E-03	3.70E+02	1.73E-03	3.89E+02	2.00E-03	4.76E+01	1.82E-04
	13.69	4.59E+02	3.64E-03	3.77E+02	1.76E-03	3.97E+02	2.04E-03	4.37E+01	1.67E-04
	13.31	6.11E+02	4.84E-03	4.77E+02	2.23E-03	5.08E+02	2.61E-03	5.04E+01	1.92E-04
	12.93	5.70E+02	4.52E-03	4.44E+02	2.08E-03	4.71E+02	2.42E-03	3.70E+01	1.41E-04
	12.58	9.31E+02	7.37E-03	1.10E+03	5.14E-03	1.21E+03	6.21E-03	1.10E+02	4.20E-04

Table E2. Capsule 5 measured inner and outer ring radial concentrations [35].

Ring	Radius	Ag-110m		Cs-134		Cs-137		Sr-90	
	(mm)	(Bq/mm^3)	(mol/m^3)	(Bq/mm^3)	(mol/m^3)	(Bq/mm^3)	(mol/m^3)	(Bq/mm^3)	(mol/m^3)
Inner	11.75	2.74E+00	1.75E-05	2.45E+03	9.23E-03	1.65E+03	8.35E-03	3.56E+01	1.35E-04
	11.31	6.16E+00	3.93E-05	2.57E+03	9.68E-03	1.65E+03	8.35E-03	8.39E+00	3.19E-05
	10.80	8.91E+00	5.68E-05	4.24E+03	1.60E-02	2.74E+03	1.39E-02	4.81E+00	1.83E-05
	10.29	1.88E+01	1.20E-04	6.25E+03	2.35E-02	4.21E+03	2.13E-02	3.50E+00	1.33E-05
	9.78	1.51E+01	9.63E-05	8.17E+03	3.08E-02	5.54E+03	2.80E-02	1.28E+00	4.87E-06
	9.27	3.34E+01	2.13E-04	1.08E+04	4.07E-02	7.30E+03	3.70E-02	2.43E+00	9.24E-06
	8.77	3.69E+01	2.35E-04	1.40E+04	5.27E-02	9.56E+03	4.84E-02	1.39E+00	5.29E-06
	8.26	2.30E+01	1.47E-04	1.85E+04	6.97E-02	1.27E+04	6.43E-02	–	–
	7.75	1.13E+02	7.20E-04	2.29E+04	8.63E-02	1.62E+04	8.20E-02	6.72E+00	2.56E-05
	7.24	7.17E+01	4.57E-04	2.63E+04	9.91E-02	1.84E+04	9.32E-02	–	–
	6.73	2.54E+02	1.62E-03	3.20E+04	1.21E-01	2.34E+04	1.18E-01	1.20E+00	4.56E-06
	6.42	3.27E+03	2.08E-02	1.33E+05	5.01E-01	1.01E+05	5.11E-01	2.03E+02	7.72E-04
Outer	19.50	1.65E+00	1.05E-05	1.05E+02	3.95E-04	1.11E+02	5.62E-04	2.61E+01	9.93E-05
	19.06	5.33E-01	3.40E-06	4.66E+01	1.76E-04	3.52E+01	1.78E-04	9.53E+00	3.62E-05
	18.55	7.41E-01	4.72E-06	4.45E+01	1.68E-04	3.26E+01	1.65E-04	7.00E+00	2.66E-05
	18.04	2.97E-01	1.89E-06	4.83E+01	1.82E-04	3.51E+01	1.78E-04	6.84E+00	2.60E-05
	17.54	2.09E+00	1.33E-05	5.50E+01	2.07E-04	3.90E+01	1.97E-04	7.03E+00	2.67E-05
	17.03	6.01E-01	3.83E-06	1.68E+01	6.33E-05	1.18E+01	5.97E-05	5.19E+00	1.97E-05
	16.52	1.93E+00	1.23E-05	4.18E+01	1.57E-04	2.99E+01	1.51E-04	4.83E+00	1.84E-05
	16.01	8.98E-01	5.73E-06	4.65E+01	1.75E-04	3.19E+01	1.61E-04	4.54E+00	1.73E-05
	15.50	1.38E+00	8.80E-06	5.66E+01	2.13E-04	3.89E+01	1.97E-04	7.44E+00	2.83E-05
	15.00	2.12E+00	1.35E-05	5.67E+01	2.14E-04	3.90E+01	1.97E-04	5.80E+00	2.21E-05
	14.49	9.32E-01	5.94E-06	6.41E+01	2.41E-04	5.06E+01	2.56E-04	7.32E+00	2.78E-05
	13.98	1.26E+00	8.03E-06	3.90E+01	1.47E-04	2.65E+01	1.34E-04	1.96E+00	7.45E-06
	13.47	1.08E+00	6.89E-06	6.29E+01	2.37E-04	4.38E+01	2.22E-04	3.88E+00	1.48E-05
	12.96	9.28E-01	5.92E-06	6.66E+01	2.51E-04	4.45E+01	2.25E-04	4.16E+00	1.58E-05
	12.53	1.88E+01	1.20E-04	2.96E+02	1.11E-03	2.03E+02	1.03E-03	8.17E+00	3.11E-05

Table E3. Capsule 7 measured inner and outer ring radial concentrations [35].

Ring	Radius (mm)	Ag-110m (Bq/mm³)	Ag-110m (mol/m³)	Cs-134 (Bq/mm³)	Cs-134 (mol/m³)	Cs-137 (Bq/mm³)	Cs-137 (mol/m³)	Sr-90 (Bq/mm³)	Sr-90 (mol/m³)
Inner	11.65	8.94E+00	5.61E-05	6.11E+02	2.29E-03	7.82E+02	3.96E-03	4.66E+03	1.77E-02
	11.20	2.80E+00	1.76E-05	5.33E+02	2.00E-03	4.59E+02	2.32E-03	5.20E+02	1.98E-03
	10.70	6.35E+00	3.99E-05	6.50E+02	2.44E-03	5.57E+02	2.82E-03	3.26E+02	1.24E-03
	10.19	8.80E+00	5.52E-05	7.57E+02	2.84E-03	6.41E+02	3.24E-03	2.31E+02	8.78E-04
	9.68	1.39E+01	8.72E-05	7.68E+02	2.88E-03	6.55E+02	3.31E-03	1.95E+02	7.41E-04
	9.17	9.83E+00	6.17E-05	8.42E+02	3.16E-03	7.19E+02	3.64E-03	1.28E+02	4.87E-04
	8.66	1.12E+01	7.03E-05	9.87E+02	3.70E-03	8.57E+02	4.33E-03	1.18E+02	4.49E-04
	8.16	6.60E+00	4.14E-05	1.00E+03	3.75E-03	8.64E+02	4.37E-03	1.37E+02	5.21E-04
	7.65	7.03E+00	4.41E-05	1.11E+03	4.16E-03	9.80E+02	4.96E-03	5.93E+02	2.25E-03
	7.14	1.64E+01	1.03E-04	1.15E+03	4.31E-03	1.02E+03	5.16E-03	1.82E+04	6.92E-02
	6.64	4.54E+02	2.85E-03	1.57E+03	5.89E-03	1.68E+03	8.50E-03	4.47E+05	1.70E+00
Outer	18.49	5.78E+01	3.63E-04	6.03E+02	2.26E-03	5.12E+02	2.59E-03	5.20E+01	1.98E-04
	18.04	3.92E+01	2.46E-04	3.86E+02	1.45E-03	2.99E+02	1.51E-03	2.65E+01	1.01E-04
	17.53	2.73E+01	1.71E-04	5.02E+02	1.88E-03	3.91E+02	1.98E-03	3.01E+01	1.14E-04
	17.03	1.44E+01	9.04E-05	5.53E+02	2.07E-03	4.35E+02	2.20E-03	3.05E+01	1.16E-04
	16.52	1.07E+01	6.72E-05	5.75E+02	2.16E-03	4.54E+02	2.30E-03	2.41E+01	9.16E-05
	16.01	9.27E+00	5.82E-05	6.25E+02	2.34E-03	5.01E+02	2.53E-03	2.41E+01	9.16E-05
	15.50	1.03E+01	6.46E-05	6.92E+02	2.59E-03	5.59E+02	2.83E-03	2.26E+01	8.59E-05
	14.99	1.06E+01	6.65E-05	7.94E+02	2.98E-03	6.41E+02	3.24E-03	2.28E+01	8.67E-05
	14.49	1.14E+01	7.16E-05	8.54E+02	3.20E-03	6.85E+02	3.46E-03	2.08E+01	7.91E-05
	13.98	1.22E+01	7.66E-05	9.15E+02	3.43E-03	7.42E+02	3.75E-03	1.77E+01	6.73E-05
	13.47	1.29E+01	8.10E-05	1.10E+03	4.12E-03	8.86E+02	4.48E-03	1.71E+01	6.50E-05
	12.96	1.09E+01	6.84E-05	9.79E+02	3.67E-03	7.83E+02	3.96E-03	8.35E+00	3.18E-05
	12.59	1.52E+02	9.54E-04	2.47E+03	9.26E-03	2.03E+03	1.03E-02	6.64E+01	2.52E-04

Table E4. Capsule 8 measured inner and outer ring radial concentrations [35].

Ring	Radius (mm)	Ag-110m (Bq/mm^3)	Ag-110m (mol/m^3)	Cs-134 (Bq/mm^3)	Cs-134 (mol/m^3)	Cs-137 (Bq/mm^3)	Cs-137 (mol/m^3)	Sr-90 (Bq/mm^3)	Sr-90 (mol/m^3)
Inner	11.84	7.06E+02	4.63E-03	1.12E+03	4.41E-03	1.09E+03	5.53E-03	1.84E+02	7.00E-04
	11.39	5.54E+02	3.64E-03	9.99E+02	3.93E-03	9.07E+02	4.60E-03	2.79E+01	1.06E-04
	10.88	3.45E+02	2.26E-03	9.83E+02	3.87E-03	9.23E+02	4.68E-03	1.85E+01	7.04E-05
	10.37	2.16E+02	1.42E-03	9.83E+02	3.87E-03	9.25E+02	4.69E-03	1.38E+01	5.25E-05
	9.87	1.61E+02	1.06E-03	9.10E+02	3.58E-03	8.60E+02	4.36E-03	1.49E+01	5.67E-05
	9.36	1.34E+02	8.80E-04	9.30E+02	3.66E-03	9.14E+02	4.64E-03	1.15E+01	4.38E-05
	8.85	1.18E+02	7.75E-04	9.57E+02	3.76E-03	9.22E+02	4.68E-03	3.13E+01	1.19E-04
	8.34	9.12E+01	5.99E-04	9.96E+02	3.92E-03	9.69E+02	4.91E-03	1.64E+02	6.24E-04
	7.83	7.47E+01	4.90E-04	1.01E+03	3.97E-03	9.88E+02	5.01E-03	1.71E+03	6.51E-03
	7.33	6.83E+01	4.48E-04	9.04E+02	3.56E-03	9.00E+02	4.56E-03	4.83E+03	1.84E-02
	6.82	6.81E+01	4.47E-04	8.63E+02	3.39E-03	8.72E+02	4.42E-03	1.40E+04	5.33E-02
	6.44	1.72E+02	1.13E-03	1.53E+03	6.02E-03	1.58E+03	8.01E-03	7.85E+04	2.99E-01
Outer	19.08	1.04E+03	6.83E-03	2.55E+03	1.00E-02	2.17E+03	1.10E-02	1.92E+01	7.31E-05
	18.64	8.81E+02	5.78E-03	2.00E+03	7.87E-03	1.69E+03	8.57E-03	5.43E+00	2.07E-05
	18.13	1.29E+03	8.47E-03	2.09E+03	8.22E-03	1.77E+03	8.98E-03	4.59E+00	1.75E-05
	17.62	1.93E+03	1.27E-02	2.19E+03	8.62E-03	1.87E+03	9.48E-03	5.14E+00	1.96E-05
	17.12	2.99E+03	1.96E-02	2.22E+03	8.73E-03	1.89E+03	9.58E-03	4.45E+00	1.69E-05
	16.61	3.80E+03	2.49E-02	2.34E+03	9.21E-03	1.99E+03	1.01E-02	3.69E+00	1.40E-05
	16.10	4.43E+03	2.91E-02	2.50E+03	9.83E-03	2.16E+03	1.10E-02	5.01E+00	1.91E-05
	15.59	5.86E+03	3.85E-02	2.88E+03	1.13E-02	2.49E+03	1.26E-02	4.37E+00	1.66E-05
	15.08	6.56E+03	4.31E-02	2.75E+03	1.08E-02	2.39E+03	1.21E-02	4.29E+00	1.63E-05
	14.58	6.75E+03	4.43E-02	2.66E+03	1.05E-02	2.30E+03	1.17E-02	4.08E+00	1.55E-05
	14.07	6.50E+03	4.27E-02	3.04E+03	1.20E-02	2.66E+03	1.35E-02	4.57E+00	1.74E-05
	13.56	4.64E+03	3.05E-02	2.74E+03	1.08E-02	2.39E+03	1.21E-02	3.86E+00	1.47E-05
	13.05	4.30E+03	2.82E-02	3.09E+03	1.22E-02	2.70E+03	1.37E-02	4.97E+00	1.89E-05
	12.59	5.50E+03	3.61E-02	5.21E+03	2.05E-02	4.64E+03	2.35E-02	1.52E+01	5.78E-05

Table E5. Capsule 10 measured inner and outer ring radial concentrations [35].

Ring	Radius (mm)	Ag-110m (Bq/mm³)	(mol/m³)	Cs-134 (Bq/mm³)	(mol/m³)	Cs-137 (Bq/mm³)	(mol/m³)	Sr-90 (Bq/mm³)	(mol/m³)
		Capsule 10							
Inner	11.83	1.75E+02	1.51E-03	7.14E+02	3.69E-03	9.58E+02	4.95E-03	3.29E+02	1.26E-03
	11.38	2.20E+02	1.90E-03	5.44E+02	2.81E-03	5.92E+02	3.06E-03	5.10E+01	1.95E-04
	10.88	2.70E+02	2.34E-03	5.66E+02	2.93E-03	6.33E+02	3.27E-03	3.26E+01	1.25E-04
	10.37	4.14E+02	3.58E-03	6.84E+02	3.54E-03	7.53E+02	3.89E-03	2.86E+01	1.09E-04
	9.86	3.85E+02	3.33E-03	7.10E+02	3.67E-03	7.95E+02	4.11E-03	4.41E+01	1.68E-04
	9.35	4.23E+02	3.66E-03	8.82E+02	4.56E-03	9.64E+02	4.99E-03	1.88E+01	7.18E-05
	8.84	3.63E+02	3.14E-03	1.03E+03	5.32E-03	1.05E+03	5.43E-03	1.69E+01	6.45E-05
	8.34	1.56E+02	1.35E-03	9.64E+02	4.98E-03	1.09E+03	5.64E-03	1.46E+01	5.58E-05
	7.83	1.55E+02	1.34E-03	1.18E+03	6.10E-03	1.31E+03	6.77E-03	1.62E+01	6.19E-05
	7.32	1.33E+02	1.15E-03	1.23E+03	6.36E-03	1.37E+03	7.08E-03	8.48E+01	3.24E-04
	6.81	1.26E+02	1.09E-03	1.44E+03	7.44E-03	1.61E+03	8.33E-03	1.76E+04	6.72E-02
	6.44	2.27E+02	1.96E-03	2.52E+03	1.30E-02	2.91E+03	1.50E-02	1.13E+05	4.32E-01
Outer	18.55	2.80E+02	2.42E-03	3.04E+02	1.57E-03	5.36E+02	2.77E-03	3.82E+02	1.46E-03
	18.11	7.43E+02	6.43E-03	2.65E+02	1.37E-03	2.80E+02	1.45E-03	5.42E+01	2.07E-04
	17.60	1.21E+03	1.05E-02	3.04E+02	1.57E-03	3.26E+02	1.69E-03	3.55E+01	1.36E-04
	17.09	1.54E+03	1.33E-02	3.31E+02	1.71E-03	3.55E+02	1.84E-03	3.19E+01	1.22E-04
	16.58	2.25E+03	1.95E-02	4.86E+02	2.51E-03	5.47E+02	2.83E-03	2.57E+01	9.82E-05
	16.07	2.14E+03	1.85E-02	4.74E+02	2.45E-03	5.09E+02	2.63E-03	2.12E+01	8.10E-05
	15.57	2.29E+03	1.98E-02	6.12E+02	3.16E-03	6.82E+02	3.53E-03	3.10E+01	1.18E-04
	15.06	1.93E+03	1.67E-02	7.09E+02	3.66E-03	7.80E+02	4.03E-03	1.80E+01	6.87E-05
	14.55	1.13E+03	9.77E-03	7.02E+02	3.63E-03	7.66E+02	3.96E-03	1.71E+01	6.53E-05
	14.04	6.57E+02	5.68E-03	7.26E+02	3.75E-03	7.93E+02	4.10E-03	1.58E+01	6.03E-05
	13.53	5.48E+02	4.74E-03	8.04E+02	4.16E-03	8.80E+02	4.55E-03	8.68E+00	3.32E-05
	13.03	5.23E+02	4.52E-03	7.62E+02	3.94E-03	8.35E+02	4.32E-03	6.68E+00	2.55E-05
	12.60	4.62E+02	4.00E-03	1.07E+03	5.53E-03	1.22E+03	6.31E-03	1.19E+01	4.55E-05

Table E6. Capsule 12 measured inner and outer ring radial concentrations [35].

| Ring	Radius (mm)	Ag-110m (Bq/mm^3)	(mol/m^3)	Cs-134 (Bq/mm^3)	(mol/m^3)	Cs-137 (Bq/mm^3)	(mol/m^3)	Sr-90 (Bq/mm^3)	(mol/m^3)
			Capsule 12						
Inner	11.85	4.24E+00	9.60E-05	5.88E+00	8.52E-05	7.32E+01	4.10E-04	3.03E+01	1.17E-04
	11.33	4.50E+00	1.02E-04	4.70E+00	6.81E-05	1.60E+01	8.96E-05	6.27E+00	2.41E-05
	10.82	2.68E+00	6.07E-05	2.71E+00	3.93E-05	1.42E+01	7.95E-05	5.60E+00	2.16E-05
	10.31	4.43E+00	1.00E-04	1.01E+01	1.46E-04	4.76E+01	2.67E-04	1.95E+01	7.50E-05
	9.80	4.24E+00	9.60E-05	6.75E+00	9.78E-05	2.68E+01	1.50E-04	6.01E+00	2.31E-05
	9.29	4.13E+00	9.35E-05	1.07E+01	1.55E-04	4.57E+01	2.56E-04	7.24E+00	2.79E-05
	8.79	5.20E+00	1.18E-04	1.84E+01	2.67E-04	9.57E+01	5.36E-04	5.33E+00	2.05E-05
	8.28	5.67E+00	1.28E-04	4.03E+01	5.84E-04	1.21E+02	6.78E-04	1.31E+01	5.04E-05
	7.77	8.96E+00	2.03E-04	7.39E+01	1.07E-03	2.01E+02	1.13E-03	2.79E+01	1.07E-04
	7.26	7.07E+00	1.60E-04	1.59E+02	2.30E-03	3.88E+02	2.17E-03	5.67E+00	2.18E-05
	6.75	1.65E+01	3.74E-04	3.18E+02	4.61E-03	7.98E+02	4.47E-03	3.63E+00	1.40E-05
	6.37	2.43E+01	5.50E-04	1.14E+03	1.65E-02	3.19E+03	1.79E-02	7.61E+01	2.93E-04
Outer	17.22	2.95E+00	6.68E-05	3.30E+00	4.78E-05	6.15E+01	3.45E-04	2.93E+01	1.13E-04
	16.70	2.44E+00	5.52E-05	5.54E-01	8.03E-06	1.70E+01	9.52E-05	6.15E+00	2.37E-05
	16.19	1.98E+00	4.48E-05	2.41E-01	3.49E-06	1.38E+01	7.73E-05	4.54E+00	1.75E-05
	15.69	2.90E+00	6.57E-05	2.81E-01	4.07E-06	1.06E+01	5.94E-05	2.73E+00	1.05E-05
	15.18	1.88E+00	4.26E-05	3.80E-01	5.51E-06	1.13E+01	6.33E-05	2.94E+00	1.13E-05
	14.67	3.54E+00	8.01E-05	4.52E-01	6.55E-06	1.29E+01	7.23E-05	2.95E+00	1.14E-05
	14.16	5.44E+00	1.23E-04	3.23E-01	4.68E-06	1.56E+01	8.74E-05	2.35E+00	9.04E-06
	13.65	2.29E+00	5.18E-05	4.04E-01	5.85E-06	2.35E+01	1.32E-04	3.59E+00	1.38E-05
	13.15	2.66E+00	6.02E-05	3.86E-01	5.59E-06	1.43E+01	8.01E-05	2.52E+00	9.70E-06
	12.64	2.68E+00	6.07E-05	4.20E-01	6.08E-06	1.47E+01	8.23E-05	2.46E+00	9.47E-06
	12.32	1.62E+01	3.67E-04	5.19E+00	7.52E-05	1.68E+02	9.41E-04	3.66E+01	1.41E-04
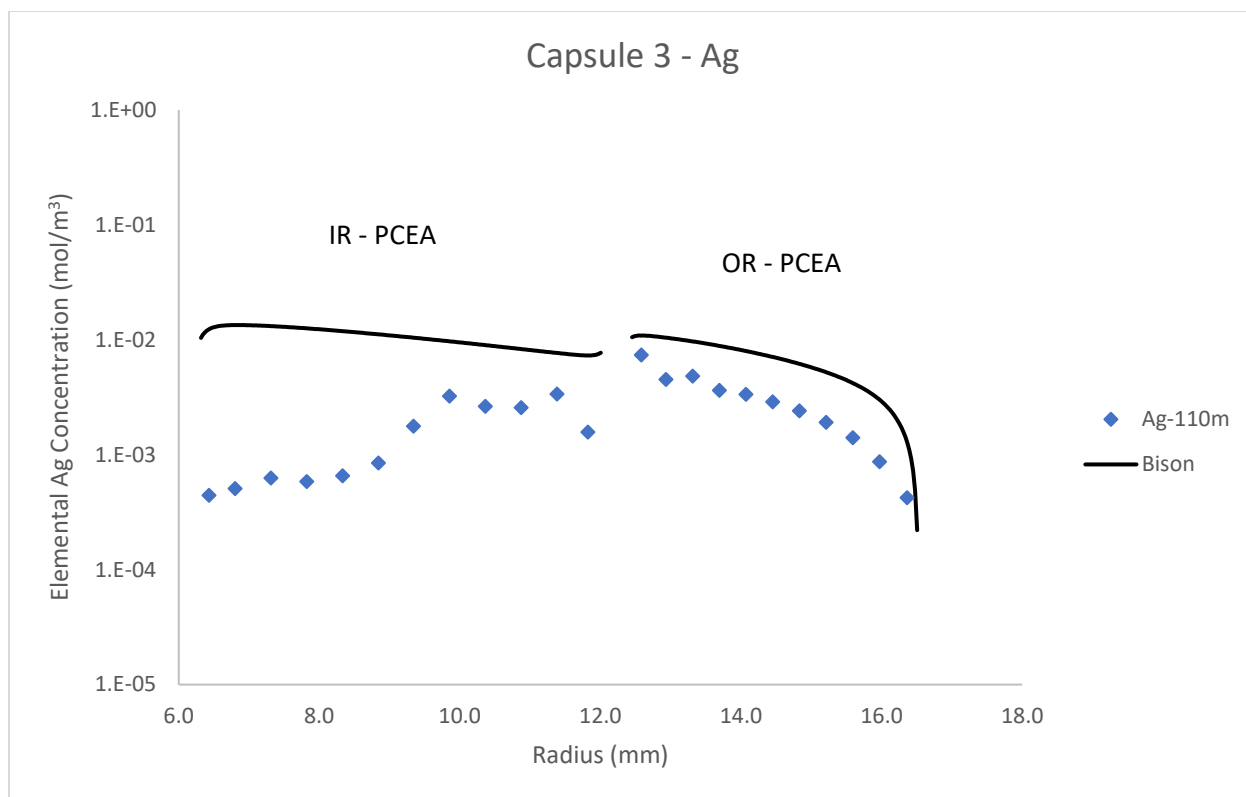
Figure E1. Capsule 3 Ag measured versus calculated concentration profile.
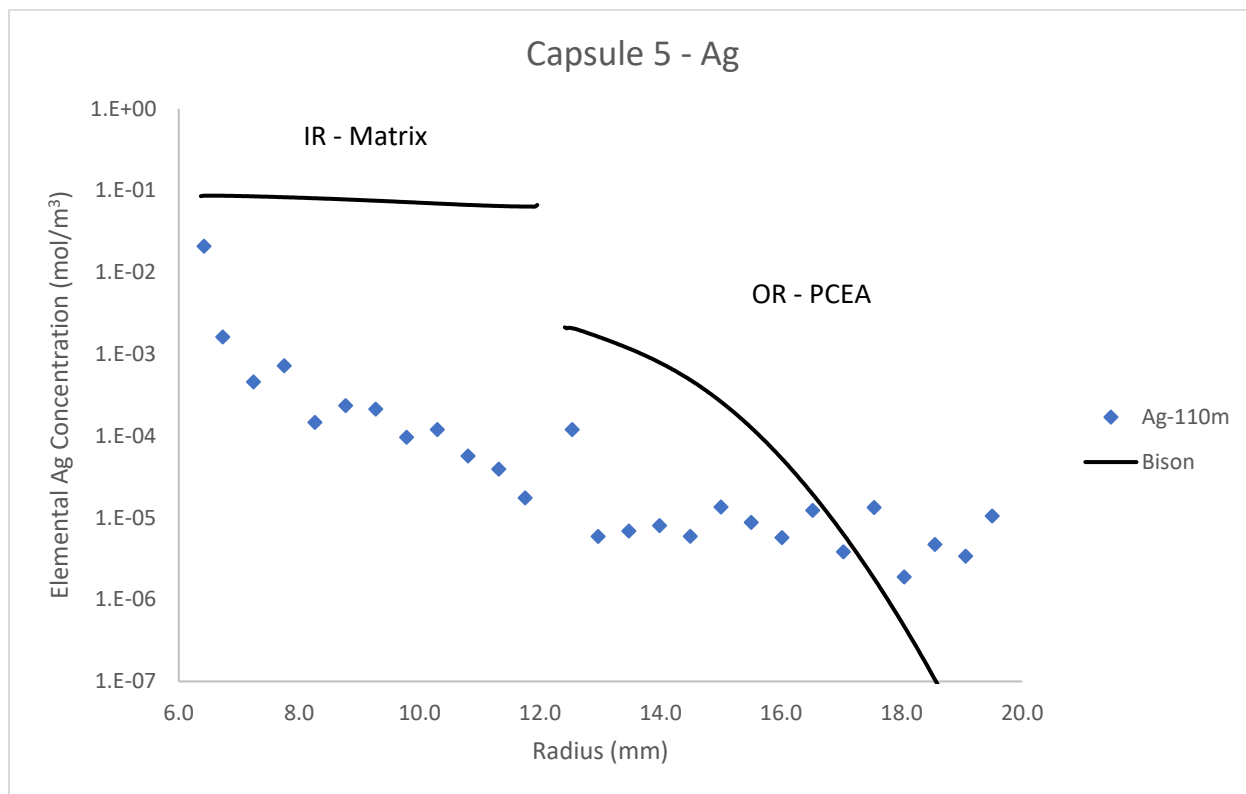

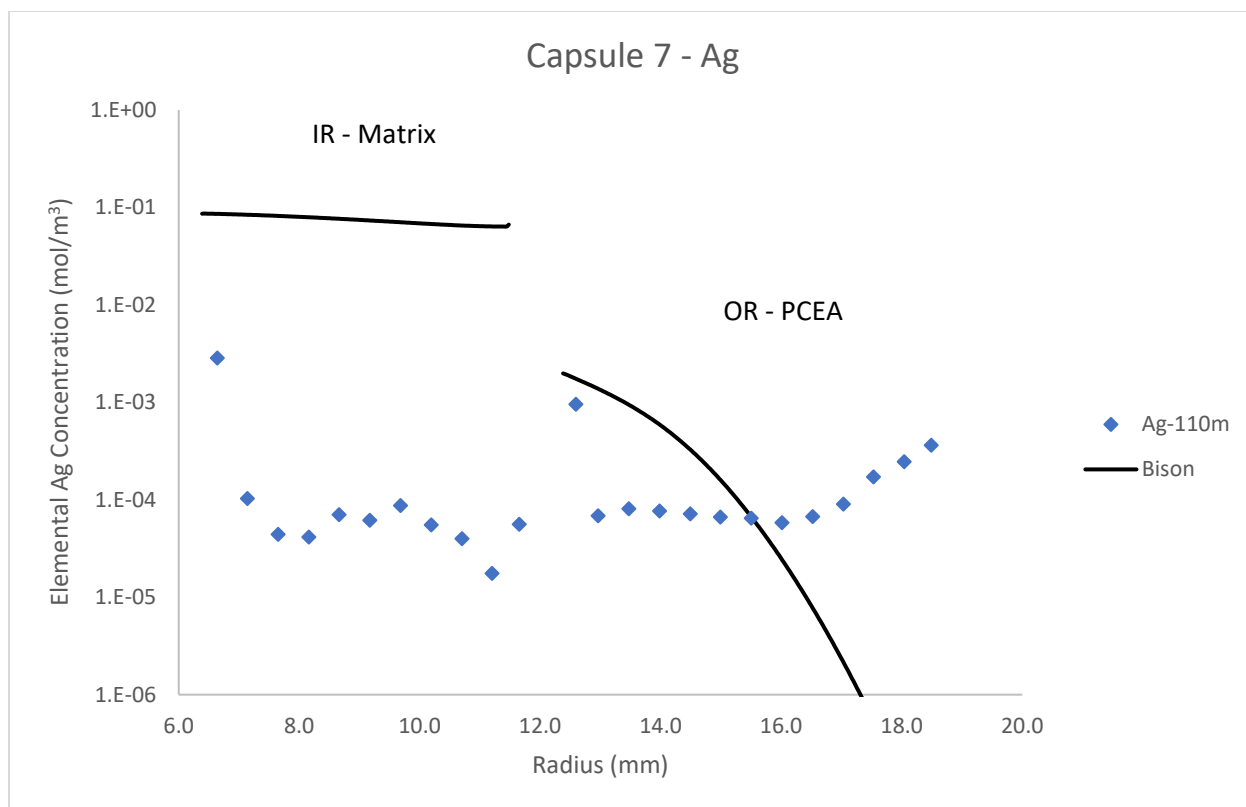Figure E2. Capsule 5 Ag measured versus calculated concentration profile.

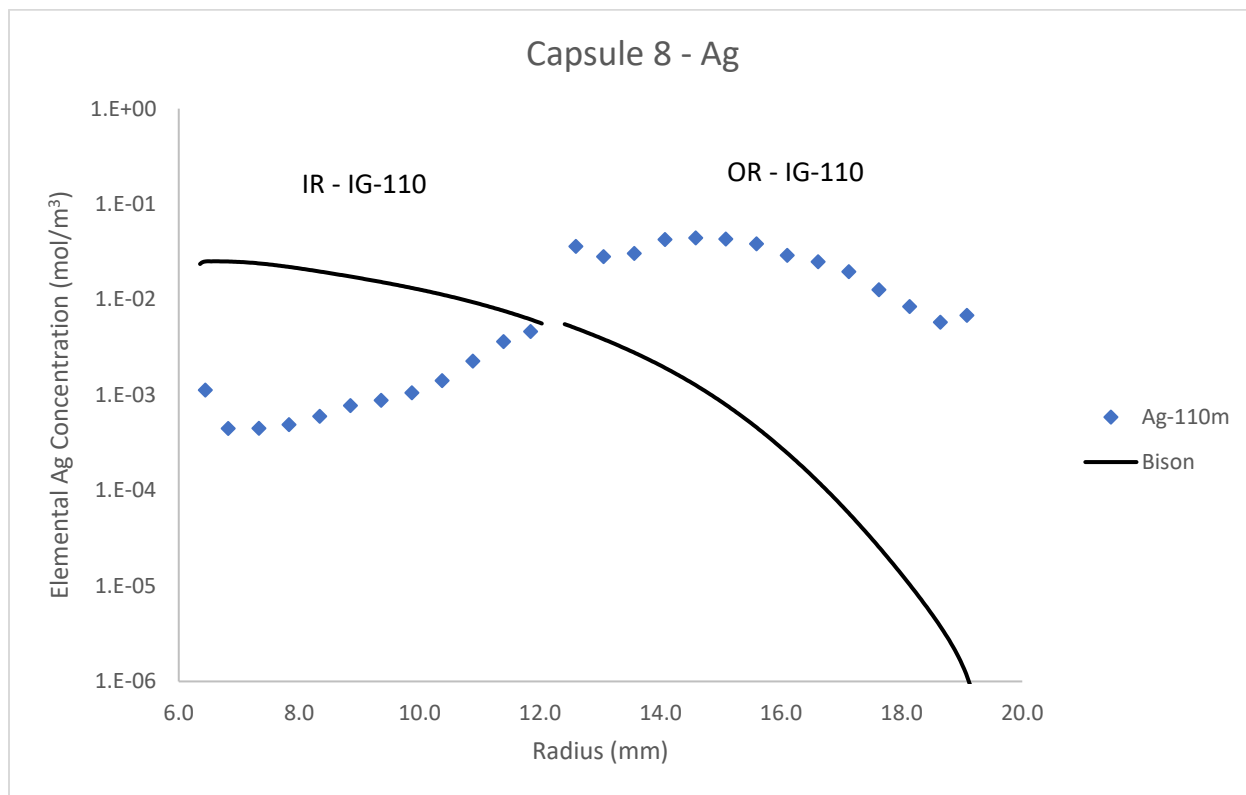Figure E3. Capsule 7 Ag measured versus calculated concentration profile.

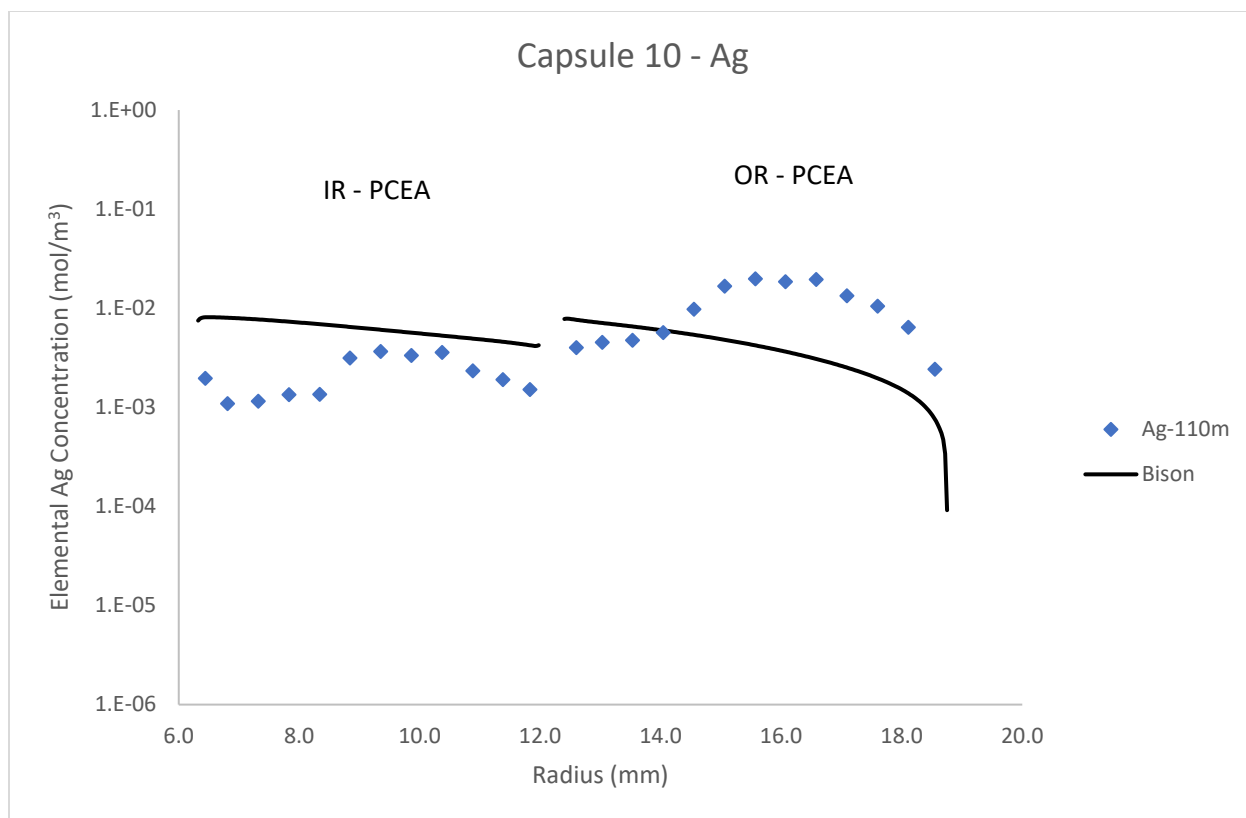Figure E4. Capsule 8 Ag measured versus calculated concentration profile.

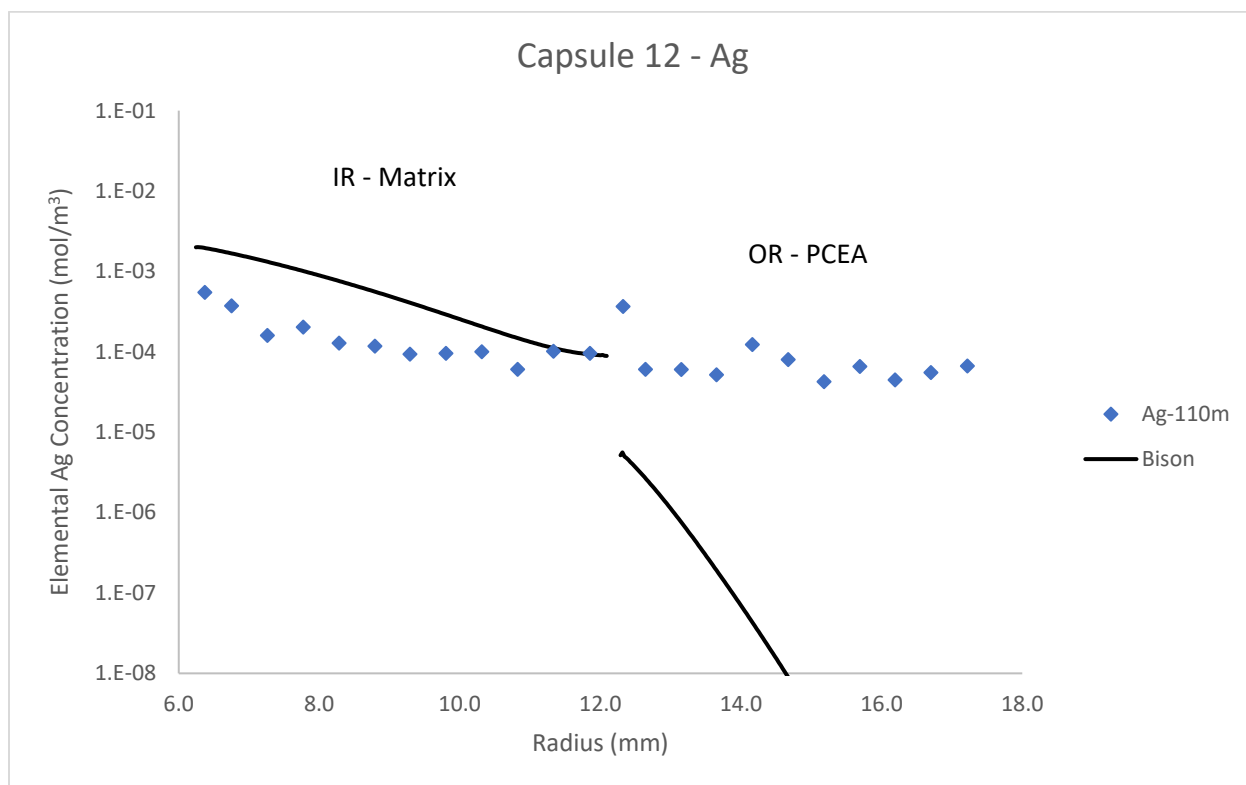Figure E5. Capsule 10 Ag measured versus calculated concentration profile.

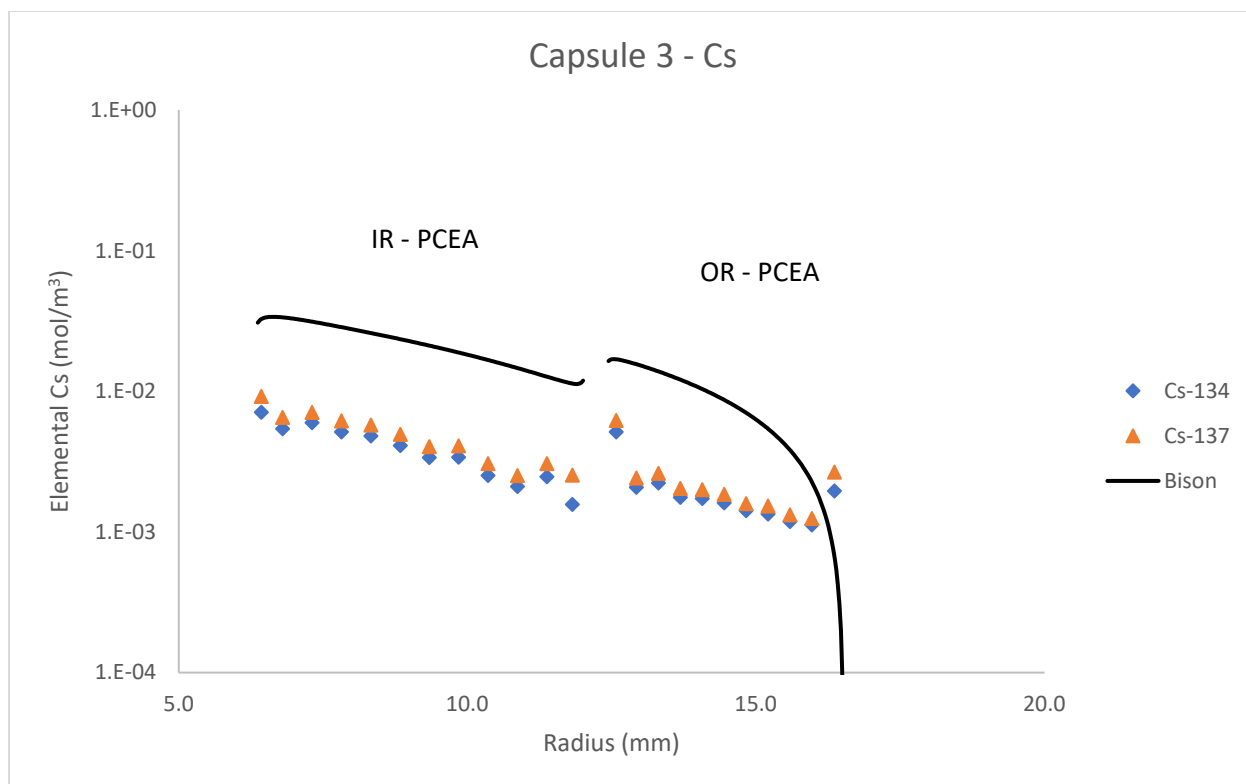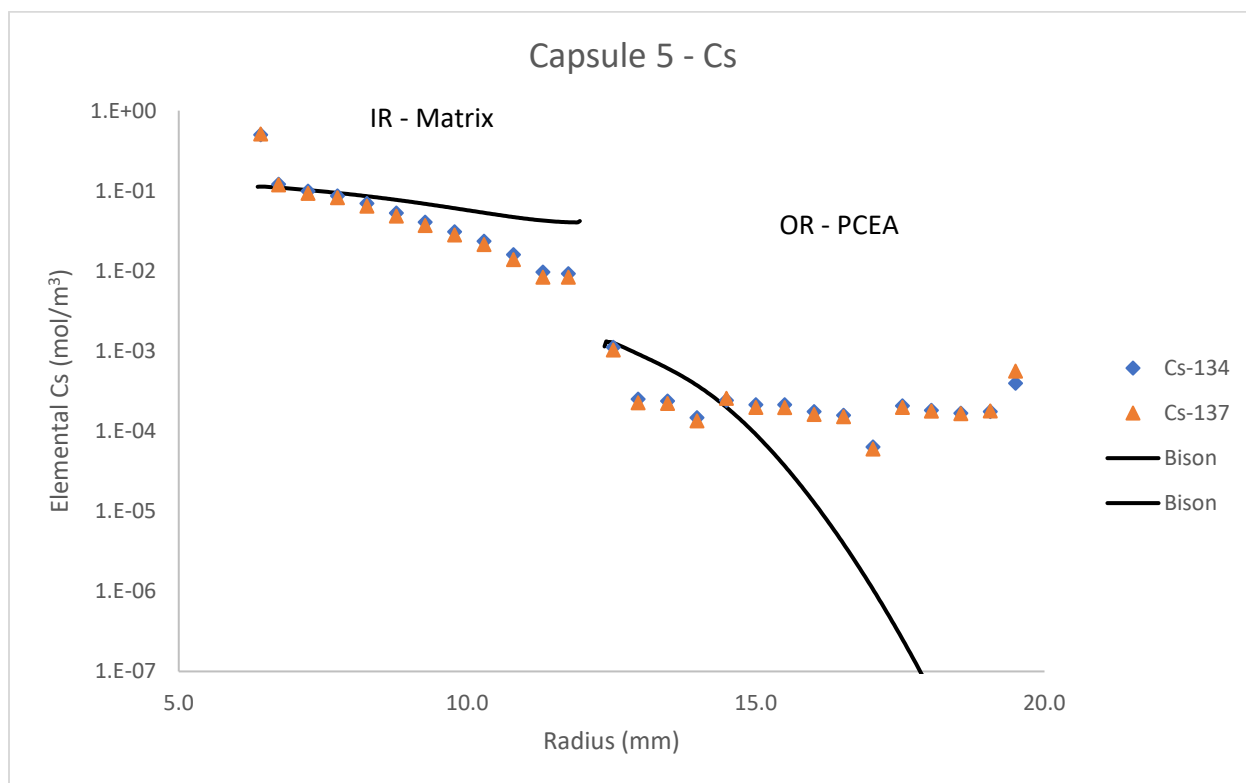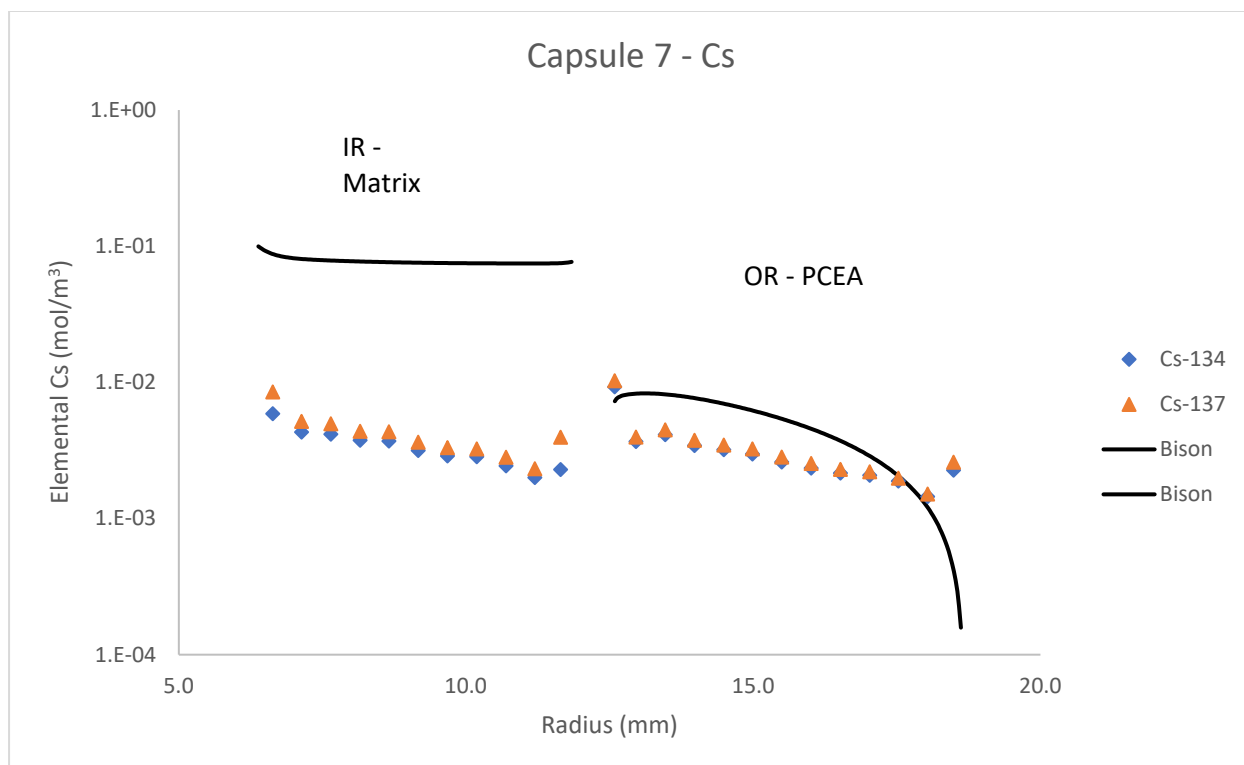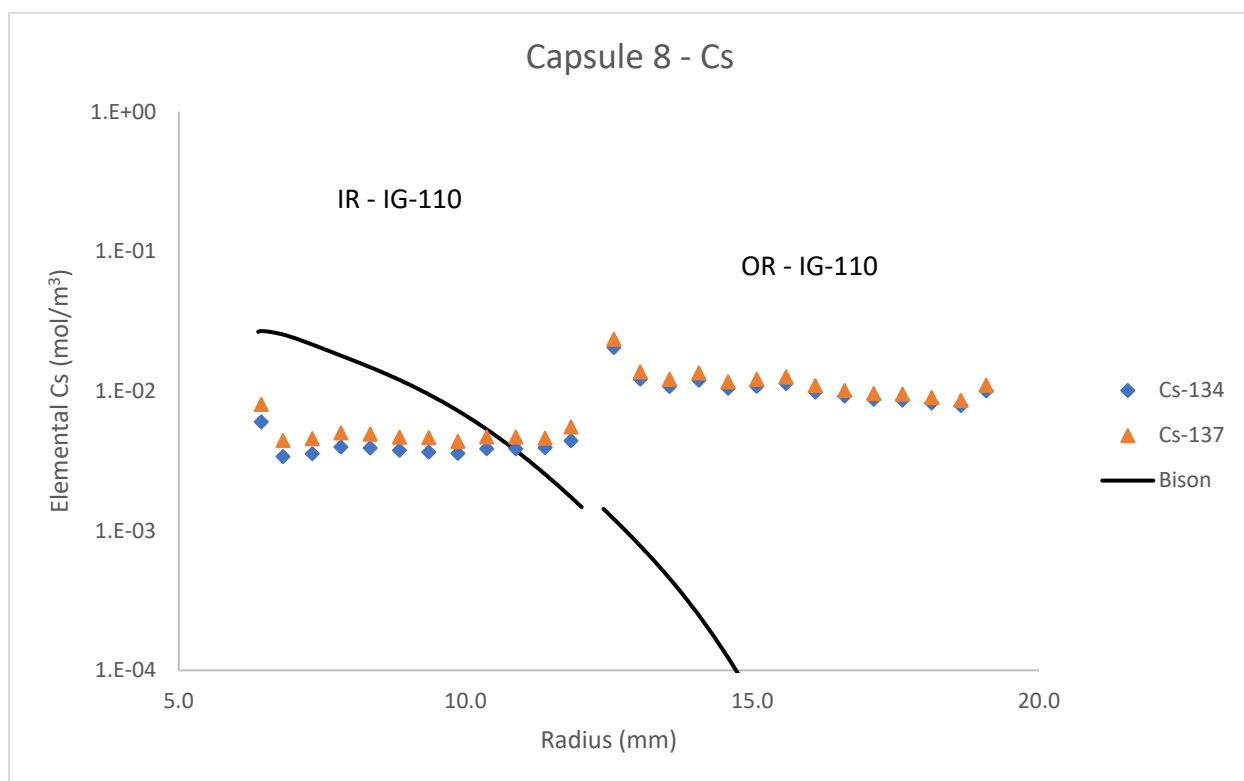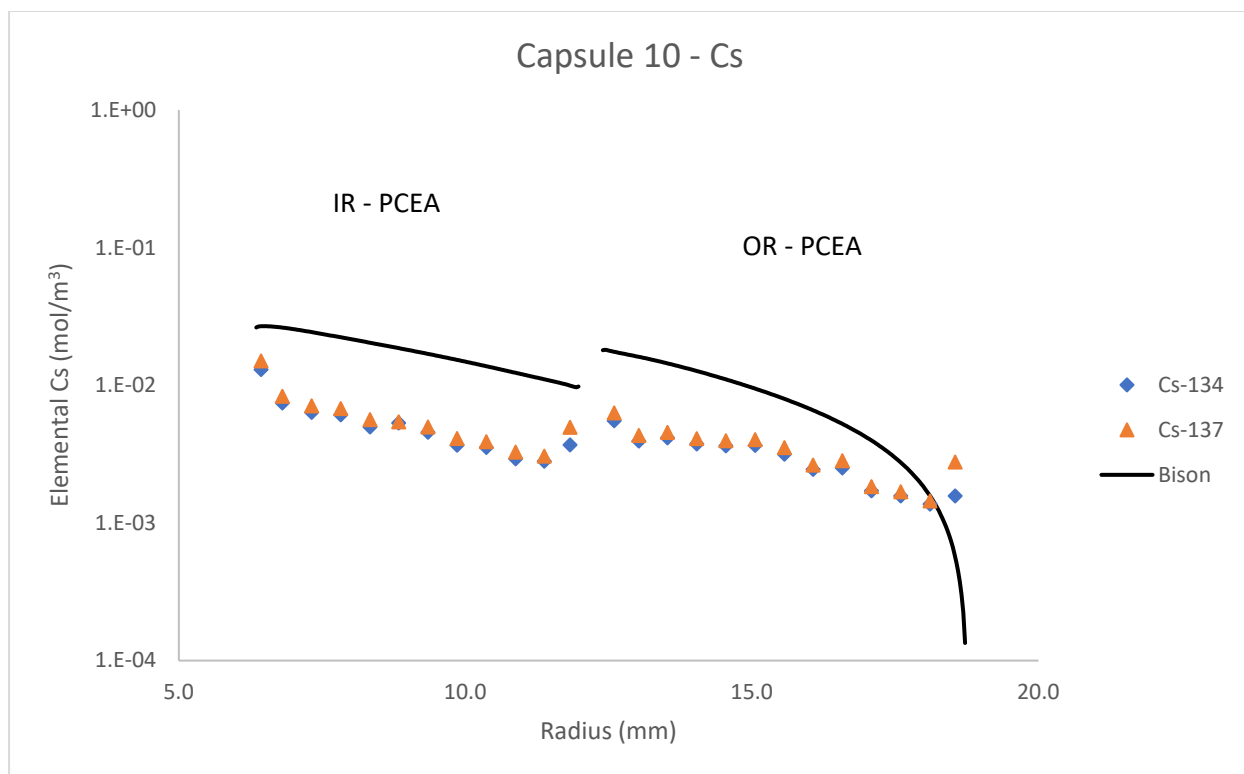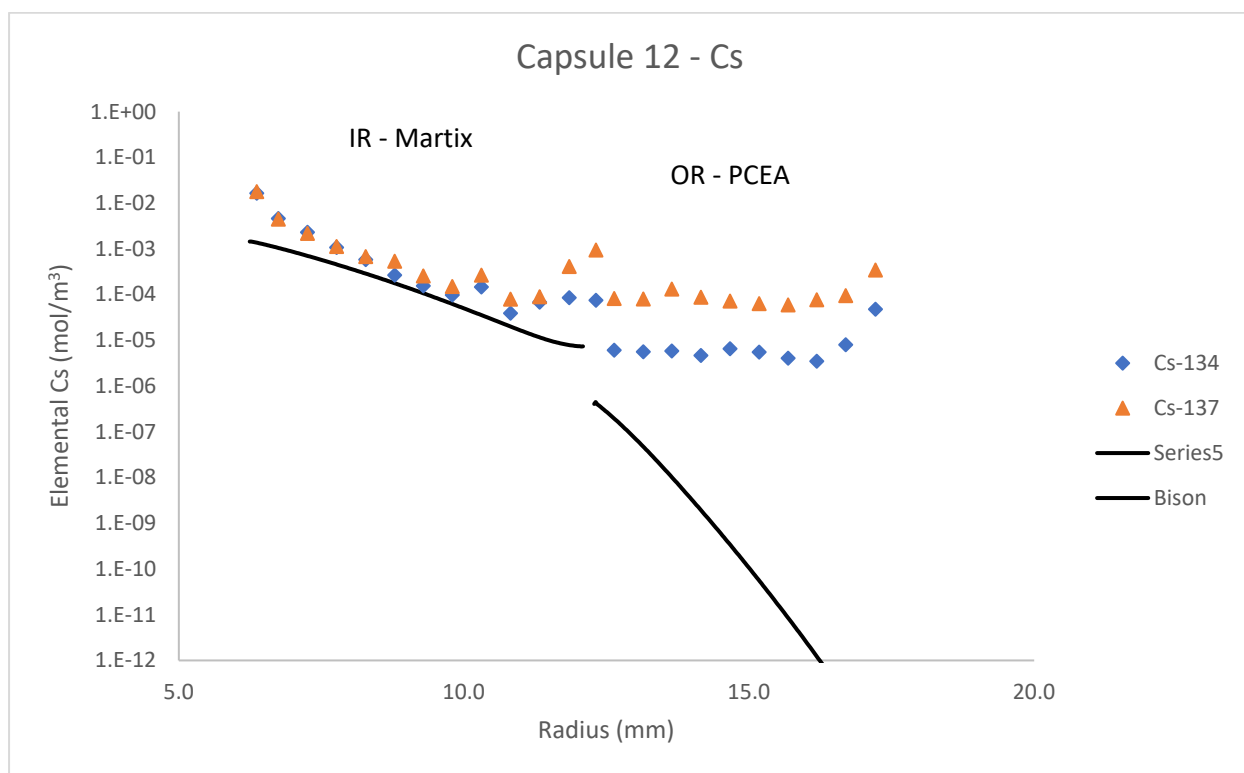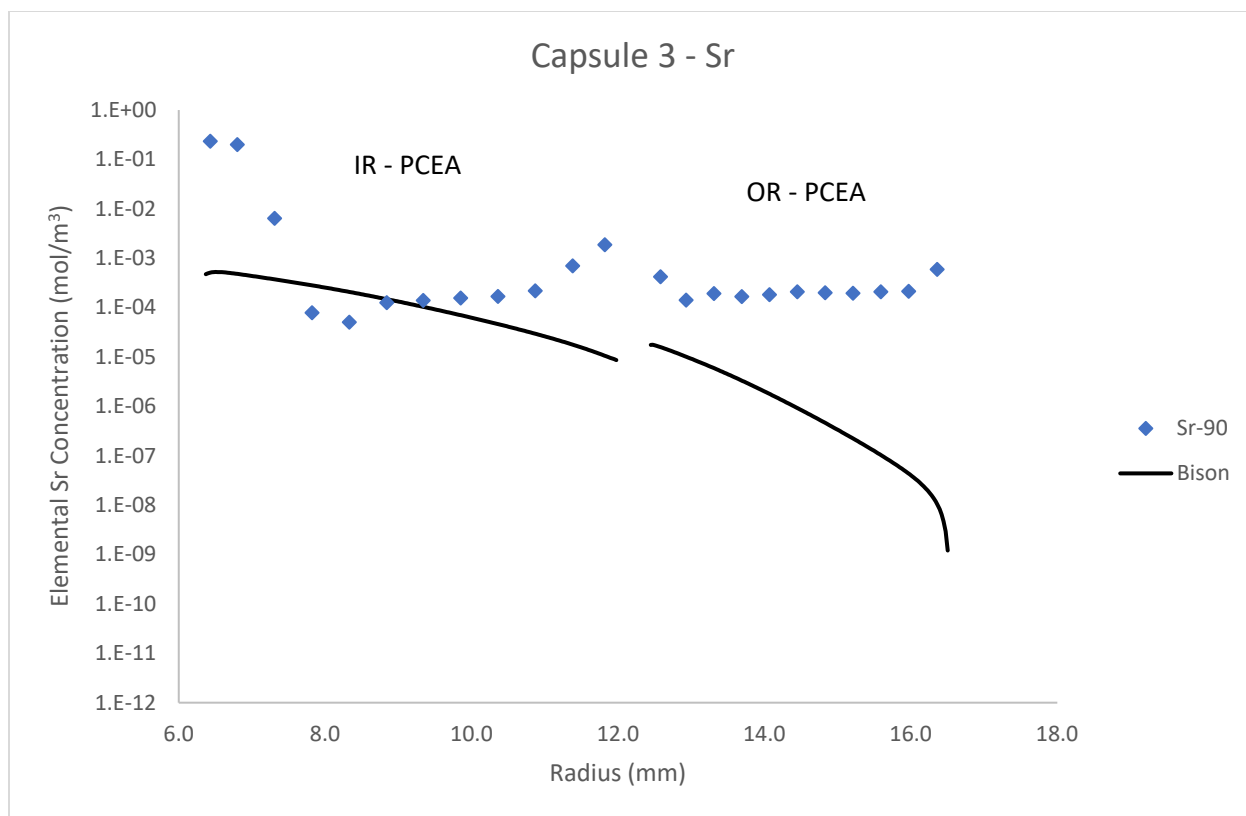Figure E6. Capsule 12 Ag measured versus calculated concentration profile.

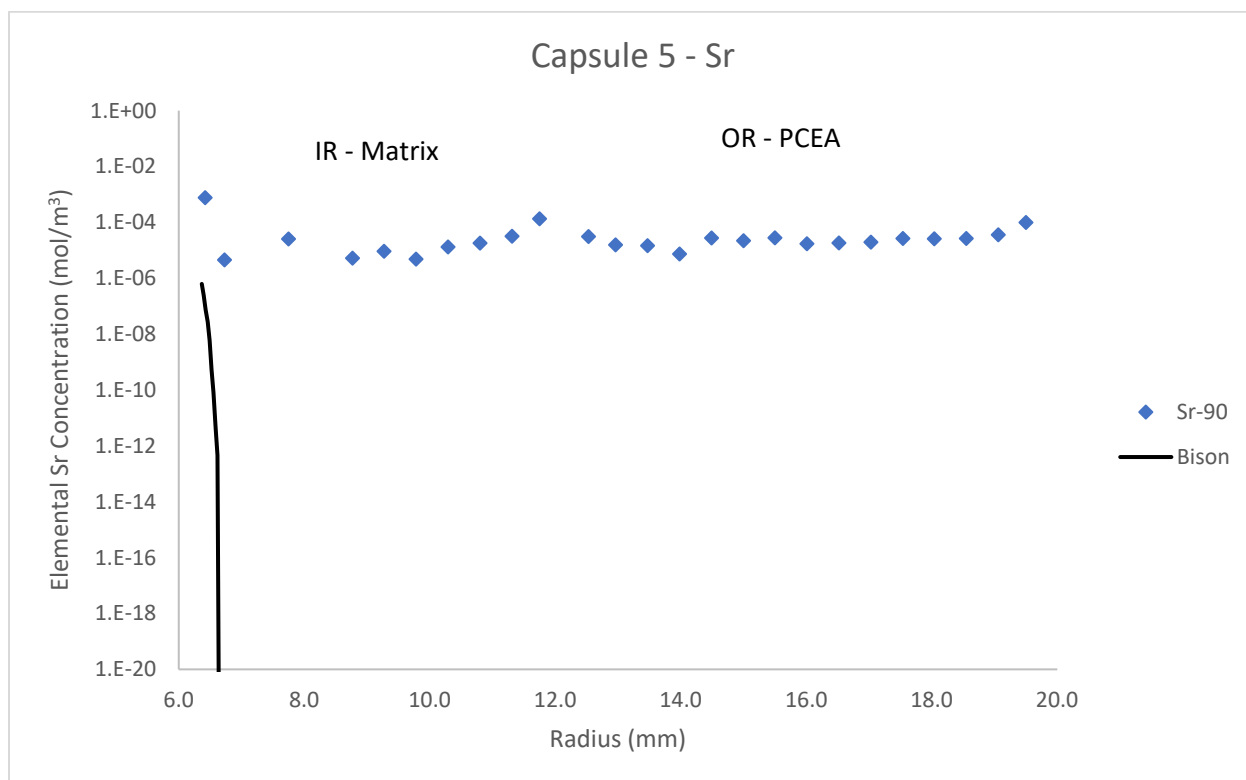Figure E7. Capsule 3 Cs measured versus calculated concentration profile.

Figure E8. Capsule 5 Cs measured versus calculated concentration profile.

Figure E9. Capsule 7 Cs measured versus calculated concentration profile.

Figure E10. Capsule 8 Cs measured versus calculated concentration profile.

Figure E11. Capsule 10 Cs measured versus calculated concentration profile.

Figure E12. Capsule 12 Cs measured versus calculated concentration profile.

Figure E13. Capsule 3 Sr measured versus calculated concentration profile.

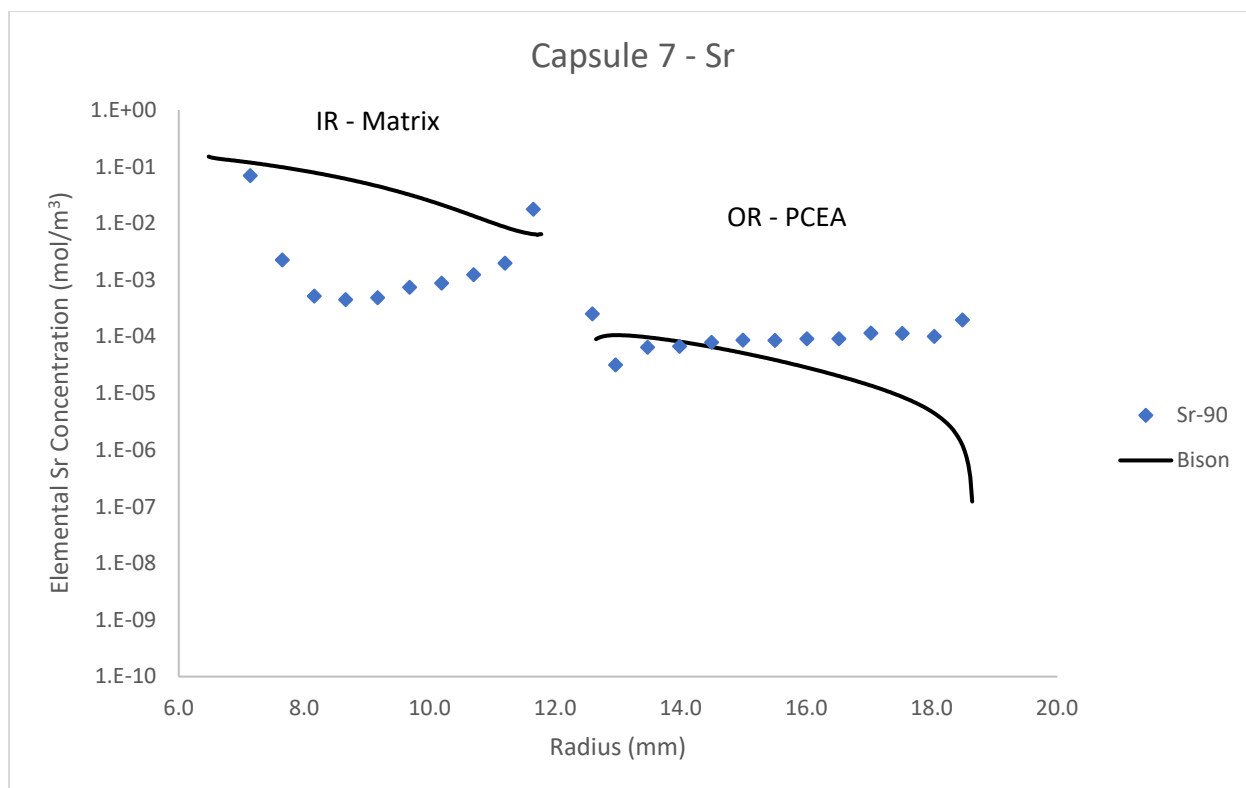Figure E14. Capsule 5 Sr measured versus calculated concentration profile.

80

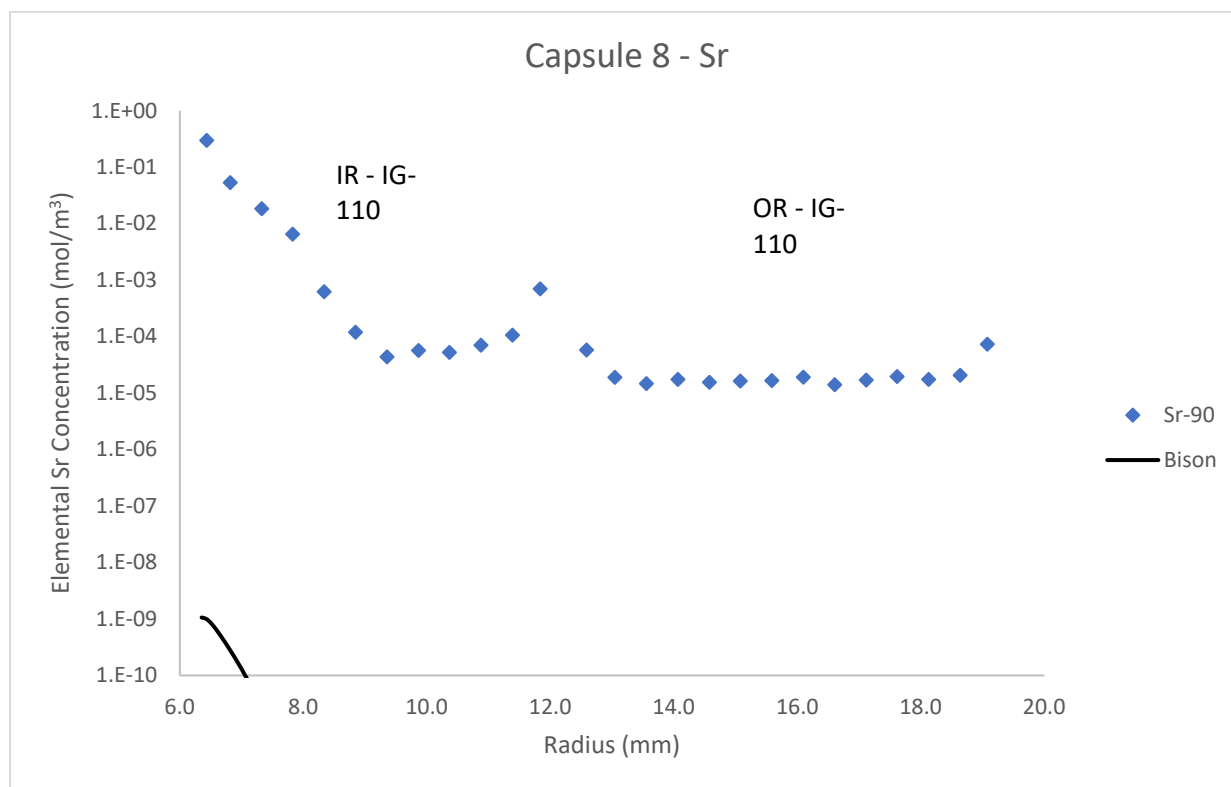Figure E15. Capsule 7 Sr measured versus calculated concentration profile.

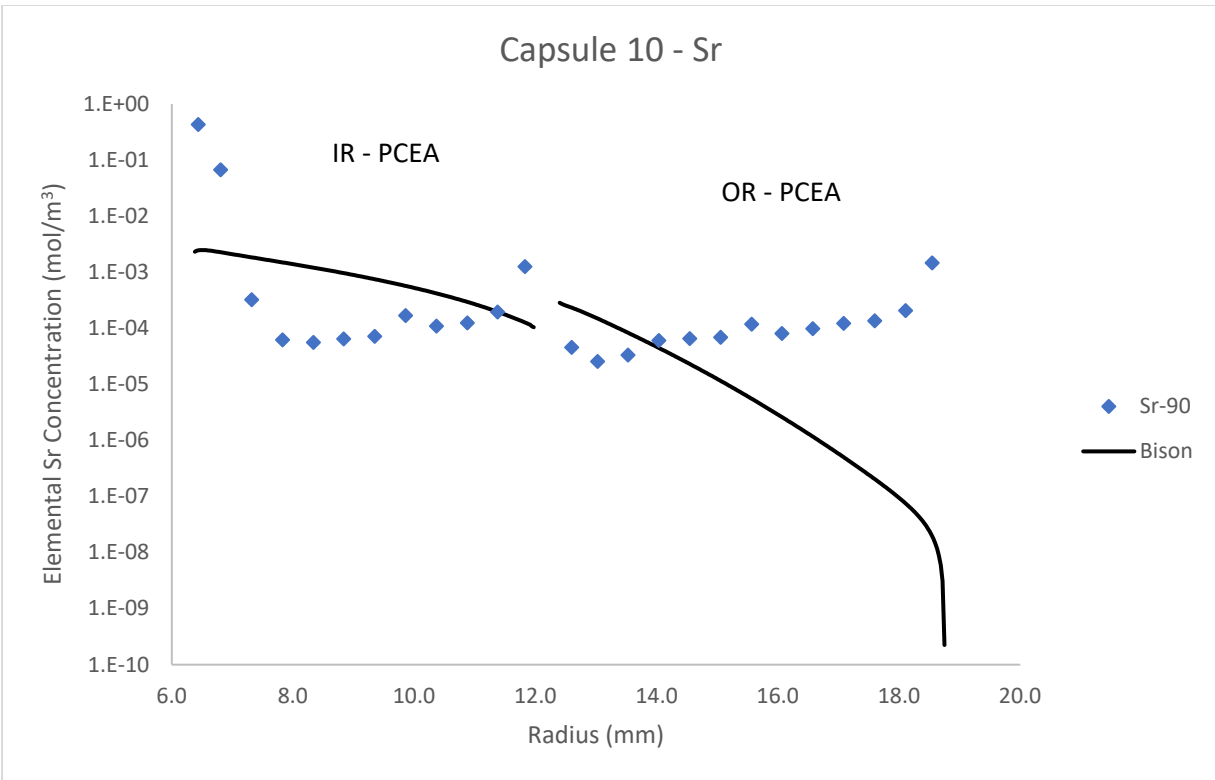Figure E16. Capsule 8 Sr measured versus calculated concentration profile.

Figure E17. Capsule 10 Sr measured versus calculated concentration profile.